Διδακτορική διατριβή του

Γεώργιου Δεληγεώργη
στο Τμήμα Φυσικής, Πανεπιστημίου Κρήτης

με θέμα:

"Κατασκευή και μελέτη διόδων laser με μεταβλητό εσωτερικό ηλεκτρικό πεδίο"

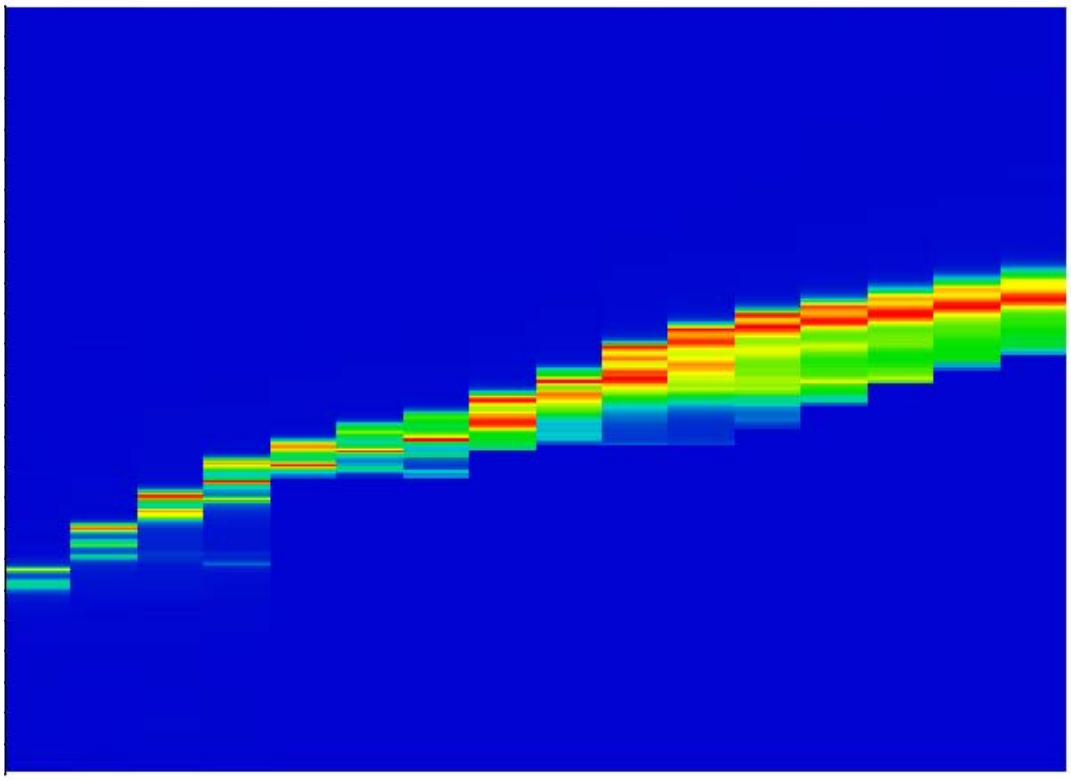

Επιβλέποντες καθηγητές:

Αλέξανδρος Γεωργακίλας (Τμήμα Φυσικής, Παν/μιο Κρητης)

Νικόλαος Πελεκάνος (Τμήμα επιστήμης Υλικών, Παν/μιο Κρήτης)

Ηράκλειο Κρήτης Ιούνιος 2008

Title: Study of semiconductor laser diodes with variable internal electric field

Physics Department, University of Crete, Greece
June 2008

Thesis author: George Deligeorgis

Thesis supervisor: Nikolaos T. Pelekanos
Alexandros Georgakilas

Thesis committee: N.T. Pelekanos
A. Georgakilas
Z. Chatzopoulos
P. Tzanetakis
C. Fotakis
S. Anastasiadis
X. Zotos

Acknowledgments

There are numerous people that have helped directly or indirectly toward the completion of this thesis. This small tribute to all of them is the least i could do to acknowledge their contribution both scientific and otherwise.

To cut a long story short, i would like to express my gratitude to G.Konstantinides and K.Michelakis for the vast knowledge on semiconductor processing, which they passed to me, to Z.Chatzopoulos for more than 40 semiconductor samples grown on Molecular Beam epitaxy, as well as numerous hours of explaining and discussion on semiconductor growth, to M.Androulidaki and K.Tsagkaraki for sharing and teaching me several characterization techniques such as photoluminescence, secondary electron microscopy e.t.c. And to two excellent technicians that were always eager to work on problems N.Papadakis and M.Sfendourakis. Last but not least I would like to thank my supervisors N.Pelekanos and A.Georgakilas for their supervision and guidance.

On a more generic, yet equally important level, I would like to thank E.Iliopoulos and P.Tzanetakis for fruitful observations and discussions. Both turned out to be key players in the route of this thesis to completion. Finally, i would like to thank F.Haimala for following through as a true friend would do.

Preface

This thesis is the result of the research work performed from January 2003 to January 2008 in the Microelectronics Research Group of the Foundation of Research and Technology Hellas. The main focus is tunable edge emitting laser diodes based on GaAs. This work would not be possible without the funding from the Greek research council for research under project "ΠΕΝΕΔ 01ΕΔ481".

The main focus of this work is experimental. Thus the goal of this thesis is twofold. Initially it is to understand the implications arising from electric fields present in a quantum well that operates under heavy carrier injection. Such quantum wells are used in semiconductor laser diodes. Secondly, it is to realize a tunable laser diode based on the quantum confined Stark effect of the quantum well responsible for gain.

The thesis is organized in parts. Starting with an introduction to semiconductor laser diodes and tunability strategies already used in todays tunable semiconductor LD's, the first part (chapters 3 – 5) discuss the work on structure growth, characterization and optimization that was necessary to obtain high quality material and a LD structure that is expected to perform comparably to the state of the art in todays semiconductor laser diodes.

The second part (chapters 6-8) presents the fabrication, the measurement methods and the characterization of reference laser diodes. Optimization of processing in order to fabricate high quality, edge emitting, ridge waveguide semiconductor lasers is discussed, as well as the techniques used to measure laser diodes. The last chapter presents the performance of the fabricated "normal" laser diodes. Normal in the sense that these are non-tunable, single quantum well, separate confinement heterostructure, edge emitting laser diodes that do not contain any tuning mechanism. These devices offer a validation of the optimization presented so far as well as a reference bench for the final part of this thesis that presents the performance of laser diodes including electric fields.

The third and final part of this thesis (chapters 9-12) discuss the performance of laser diodes that contain electric fields. The first two chapters are devoted to establishing the framework of the presented work. Initially the concept used to obtain tunable laser diodes is presented in detail (chapter 9) and subsequently (chapter 10), the details of semiconductor theory and simulation that were used to interpret the experimental results is presented. The final two chapters present the experimental results along with the theoretical simulation performed, to understand and interpret the obtained results in LD's with static and dynamic electric fields.

Table of Contents

Chapter 1.Semiconductor laser diodes

This chapter provides a quick overview of contemporary semiconductor laser diodes (LD). Its main purpose is to clarify the extend to which LD's are in fact a part of everyday life. In this sense, the research interest in the field is accordingly important. Presenting the applications of laser diodes however, also serves another purpose, to identify the needs and open issues in laser diode performance. The roadmap for further development emerges effortlessly through this discussion. The first section presents generic LD applications whereas the second section delves into the applications that benefit from device tunability.

Section:1.1. Semiconductor Laser diode applications

Semiconductor laser diodes today are a large part of everyday life. A CD or DVD player is probably within reach of the reader. All those devices would not have been realized without the use of laser diodes. But semiconductor laser applications are not limited in optical storage or recreational devices.

1.1.1 Applications of Non-tunable LD's

Besides optical storage (CD and DVD), a semiconductor laser device exists in every laser printer, in machining lines were parts are cut and/or welded using high power laser radiation and the list goes on.

In contemporary world, information is considered the new universal currency. Storing information has become extremely demanding, both in terms of size as well as speed. Optical storage has provided a fast and inexpensive way to store information with huge capacity. A compact disk is able to store 700MB whereas a Digital Video Disk (DVD) as much as 4.7GB. The first Blue ray disks have also emerged in the market with storage capacity in the order of 40-80GB. These devices utilize a semiconductor laser device to read and write an optically sensitive surface. If one considers the number of devices sold in technologically advanced countries, it is obvious that there are billion of laser devices fabricated yearly.

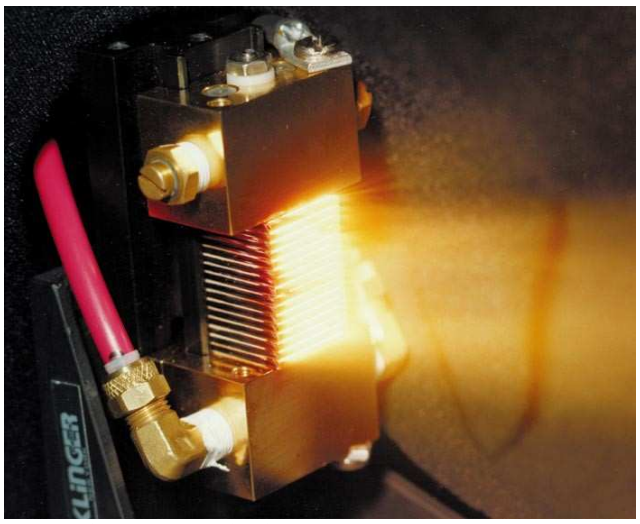

Figure 1.1.: A high power semiconductor laser diode array emitting 40KWatt. The array is water cooled. Reprinted from [1]

Printing is another example of extended LD use. Laser printers use a laser beam and a photoelectrically active surface to transfer an electronic image on paper.

High power lasers are used to ablate materials. Carbon monoxide lasers for example have been extensively used to perform laser machining. However gas lasers require maintenance and are expensive to buy. Since LD's capable of KW of optical output have emerged, they have partially replaced CO_2 lasers in such applications. LD's offer high lifetime and zero maintenance requirements. Today laser diode stacks, emitting 30-40KWatt of optical power, are routinely used to drill through metals, cut surfaces and weld materials together.

However, there are less known, yet equally important applications that have benefited from laser diodes. Contemporary solid state lasers (Nd:Yag for example) are pumped by laser diodes. Optical radar systems (LIDAR) use a laser beam, modulated at high speed to measure distance and speed of selected targets.

Optical fibers are used to transfer information using laser radiation. What was formerly achieved using microwave data links, now is routinely done using optical fibers. The rate of information transfer has sky-rocketed from Mbps (Megabits per second) to Gbps (Giga bits per second) and even Tbps (Tera bits per second) through a single optical fiber. In fact, optical fiber links have displaced satellite links as well.

The need for optical information transfer has lead to wavelength division multiplexing (WDM). In this scenario, several information channels (64) are simultaneously carried through the same medium (an optical fiber) using different wavelength of laser radiation. This enabled a drastic increase of information transfer rate. With the spread of the world wide web, and the society of information, the rate at which information is carried around the world, new applications (such as the Dense WDM) emerge. DWDM uses even more channels (128) placed closer together thus increasing the total data throughput even more.

1.1.2 Tunable LD applications

There are applications however, that require special spectral characteristics. Laser sources are used in gas analysis (measurement of absorption cross section). Such applications require not only a single wavelength source, but also the ability to tune the emission. This enables scanning through a region of interest and extracting information regarding different gas molecules. During the last twenty years, semiconductor tunable laser diodes have emerged to meet such needs.

Laser radars (LIDAR) are also good candidates for tunable devices. A tunable laser is necessary to enable a LIDAR to discriminate speed information as well as distance at the same time.

Last but not least, telecommunications. As already mentioned, many wavelengths are used in modern optical fiber systems. The cost of having a backup source for each one of them is a major issue in telecommunication technology. A tunable device is used instead. As soon one of the primary devices fails, the tunable device sets its wavelength accordingly and fills in.

Important characteristics

Diode lasers exhibit a series of unique characteristics that make them prevail in all these application. It is not only their exceptional power efficiency (~50%), neither the fact that they may be readily modulated at high speeds (>10GHz). As will be thoroughly described, LDs are compact, yet provide high optical power. Last but not least the cost to manufacture a LD is only a fraction of any other technology so far. The following table provides a comparison of laser sources and their characteristics.

Laser type	*Pump source*	*Efficiency*	*Size*	*Applications*
Gas	Discharge	Low	Large	Research, Machining
Chemical	chemical	Large	Large	Defense (MegaWatt output)
Dye	Other lasers		Large	Research (Broadly tunable)
Metal Vapor	Discharge	Low	Large	Research/ Medicine
Solid-state	Laser diodes	High	Large	Research, Machining, Medicine
Semiconductor	Current	Very high	Small	Telecommunications, optical storage, research, machining, medicine, range finding

Table 1.1: Comparison of characteristics of laser sources

It is obvious that Laser diodes offer the most appealing, cost effective solution compared to most laser sources. These applications were the motivating force that lead to such a fast development of semiconductor laser technology. In fact, tunable devices in particular are still an active research field. The field is still full of novel concepts and new publications and the motivating force for devices with improved tunability characteristics is strong.

Section:1.2.Semiconductor Laser diode – historical review

To gain a clear overview of the research field of semiconductor laser diodes, it is important to briefly look into the history of LD's. Starting from the invention of semiconductor lasers in 1962. [2] all the way to state of the art tunable laser diodes that are nowadays used in DWDM[i]

i Dense Wavelength Division Multiplexing is the upcoming generation of optical networks

telecommunication applications.

1.2.1 The roots of semiconductor laser diodes

Semiconductor lasing action was initially demonstrated in 1962 from R.N.Hall et al. [2] and M.I.Nathan et al. [3]. Continuous, low temperature, laser operation was demonstrated one year later by F.H.Dill et al [4]. The same year (1963) H.Kroemer [5] and Zh.Alferov [6] proposed the use of heterostructures in order to improve semiconductor laser diode performance. In 1968 the Zh.Alferov demonstrated the first heterostructure laser diode in pulsed mode, and in 1969 I.Hayashi [7] demonstrated the first room temperature laser diode operation.

With the rapid advance of semiconductor growth techniques, namely MBE (1971) and MOVPE (1970's), quantum well laser diodes were realized, in 1975, by J.P. van der Ziel et al [8]. Quantum wires and quantum dots were also utilized to successfully fabricate semiconductor laser diodes. Besides edge emitting laser diodes, vertical cavity surface emitting LD's were proposed and demonstrated in 1978 by H.Soda [9].

Emission wavelength of semiconductor laser diodes was initially in the near IR (840nm) but soon extended into the red part of the visible spectrum and the IR (1.3μm and 1.55μm) where fibers exhibit the minimum in dispersion and losses, respectively. Recently (1996) S.Nakamura [10] demonstrated the first long life blue LD. Today, efficient and reliable semiconductor laser diodes exist for wavelengths ranging from the UV to the far infrared, with the exception of green-yellow spectral range which is still an area of active research. The issue with Green – Yellow laser diodes is that no semiconductor material exists, that efficiently emits photons in this range.

Besides the need for fixed-wavelength laser sources, the need to obtain tunable laser sources for applications such as telecommunication's wavelength division multiplexing (WDM) and recently Dense WDM (DWDM) motivated research in this area. Remarkable results have been obtained [11], [12], [13], [14], [15] for tunable, edge emitting devices as well as for surface emitting ones. In fact, tunable semiconductor lasers is still a field of active research.

Active research in semiconductor lasers

Historically, research in the field focused initially in minimizing the losses due to scattering and absorption phenomena in the laser device. This enabled reduction of the threshold current needed to obtain gain thus improved laser performance.

As other materials became available, the emission wavelengths covered by semiconductor laser devices extended from the infrared to the low end of the visible spectrum (III-Phosphides) and recently to the UV and blue (III-Nitrides).

As far as cavity design is concerned, the advance of technology and the need for integrated laser diodes, several alternatives to cleaved mirrors where proposed. Most important of them are the layer stacks (Bragg reflectors) which provide large reflectivity (as much as 99.9%) and wavelength selectivity at the same time.

Recently, there has been increased interest in laser devices that exhibit very low threshold of operation. These devices take into account the attempts to inhibit spontaneous emission through **photonic band gap** materials [16]. This field is now emerging and is based on new, high end

semiconductor fabrication methods.

Chapter 2.Tunable semiconductor laser fundamentals

In this chapter an introduction to the internals of a laser diode are presented. This chapter sets the basis for the detailed theoretical and experimental discussion following in the rest of this thesis. After a generic discussion of the laser diode, the existing concepts leading to tunable devices is presented.

Section:2.1. Semiconductor lasers – the basics

A laser is, in a sense, three devices in one. First there has to be a **gain medium** that provides new photons inside the laser. A **waveguide** that will keep light on the right track is necessary as well. Finally there has to be an **optical cavity** that gives the necessary optical feedback to the device so that light is amplified by the gain material.

In a semiconductor, optical gain is achieved by introducing both kinds of carriers (electrons and holes) in the same region. Carriers recombine emitting photons that have energy matching the energy released by the recombination. In this way, light emitting diodes (LEDs) are realized. Normally, a fraction of the light that is emitted will be reabsorbed by the material. If however the carrier concentration is high enough, the probability of absorption becomes equal to the probability of emission. This is the point where the material behaves as if it is "transparent". If the carrier concentration is increased even more, a photon is more likely to cause stimulated emission rather than being absorbed. Thus, light is amplified. In this case, a semiconductor operates as an optical amplifier [17]. This is the operation regime of a semiconductor laser, the only difference being the **optical cavity** that makes sure that some part of the radiation is re-entering the structure. This ping-pong track of the photons results in amplification of a mode by a few orders of magnitude. That is, in a nutshell, how lasing occurs.

Gain

As will be thoroughly described later, photons may be created in a semiconductor when electrons and holes recombine. Gain is achieved in semiconductor lasers by injecting both kinds of carriers into a restricted portion of the material, this is the **active** area of the device.

The easiest way to inject both types of carriers in a semiconductor layer is by using a PN diode. One side (P-type) provides holes and the opposite side (N-type) provides electrons. In Fig.2.1 a

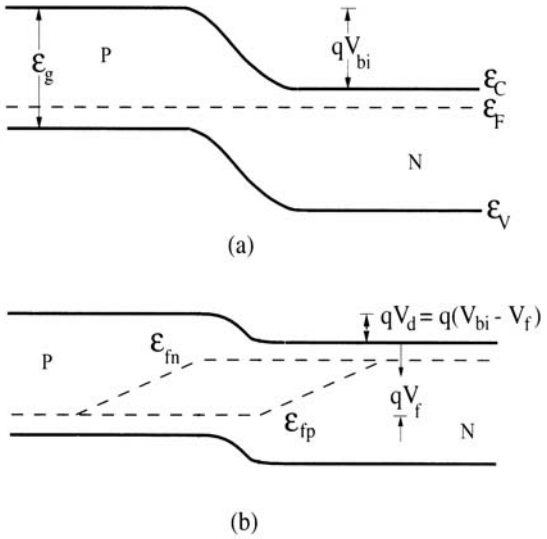

Figure 2.1.: Band diagram of a PN diode. a) Under equilibrium, b) Under forward bias.

band diagram of a simple PN diode is presented. Under forward bias, current flows through the device. Excess electrons and holes interact producing photons (we are assuming a direct bandgap semiconductor). Depending on the current flowing through the device, electronic states that were free under equilibrium conditions will now be occupied by carriers. Obviously the more the current the more the occupation probability.

In a PN structure designed for light emission, special care has to be taken so that injected carriers have no escape route. This ensures that all carriers will eventually recombine producing as many photons as possible. After a certain injection level, (i.e. current) the occupation probability becomes large enough so that a photon already present inside the active layer has a significant probability to cause stimulated emission. This occurs only if the density of states corresponding to the photon's energy are occupied to a large extend by free carriers. Given the fact that the density of states is comparable to the density of atoms in the material ($\sim 10^{23} cm^{-3}$), photon interaction with the material is strong. Fig.2.2 depicts typical gain spectra for different current density values, flowing through a semiconductor. It is worth noting the gain scale which is in the order of $10^4 cm^{-1}$. Gain values of this magnitude are readily obtainable in a semiconductor.

For low injection, gain is negative, corresponding to absorption of photons in the semiconductor. The breakthrough in semiconductor lasers was the adoption of heterostructures. Such structures ensure that carriers are contained in the active region of the device, inhibiting carrier leakage. Another advantage of using heterostructures is that the rest of the layers, having a larger bandgap, do not re-absorb any part of the laser radiation. A further improvement to the basic laser diode concept came by using quantum wells, wires or even dots as the active material. The advantage of ustilizing reduced dimensionality layers which have a modified density of states, is that the carrier density needed to obtain a given gain is less than the bulk material. Fig.2.2 provides a comparison between bulk and quantum well GaAs. Comparing two curves for the same carrier injection the gain difference is obvious.

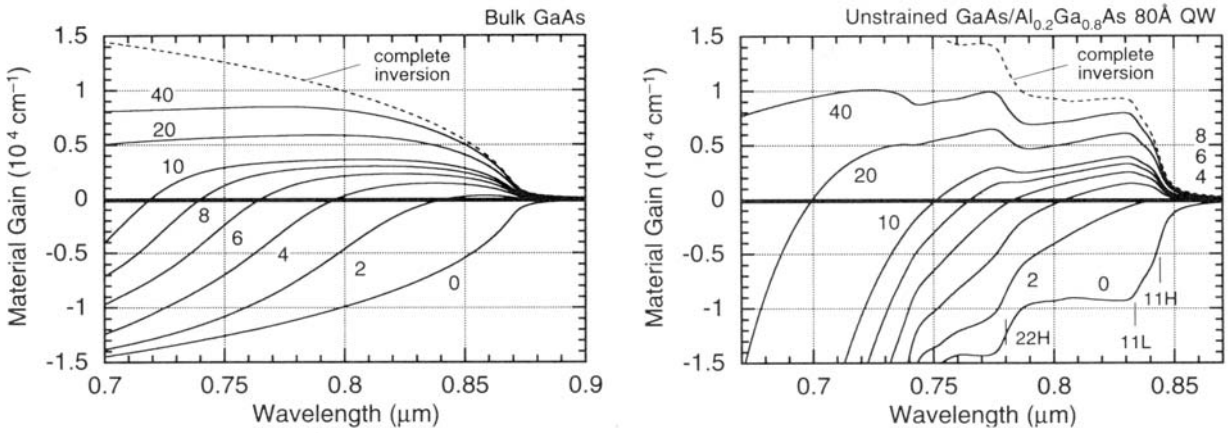

Figure 2.2.: Gain curves for a bulk GaAs (left) layer and a GaAs quantum well (right). Notice the gain scale which is in the order of $10^4 cm^{-1}$. Each curve corresponds to a different pump current density.

The gain necessary to reach lasing conditions (g_{th}) may be calculated if photon losses are known. Photons depart from the system either through the mirrors of a laser device (useful loss) or through inherent material losses (scattering, absorption e.t.c.). Eq. 2.1 is the most fundamental equation describing semiconductor laser diode operation.

$$g_{th} = a_i + \frac{1}{2 \cdot l} \ln \frac{1}{R_1 R_2} \tag{2.1}$$

a_i is the material inherent loss (cm^{-1}), l is the interaction length per round trip (cm^{-1}) and R_i corresponds to the reflectivity of the mirrors forming the cavity (here the simplest case of two mirrors is assumed). Carrier density and consequently gain, increases until lasing occurs. Above threshold, a self regulating effect appears. Carrier lifetime is sensitive to radiation density (through the stimulated emission rate which scales with photon density). More photons result in lower carrier lifetime. Based on the rate equations of a semiconductor we obtain that, to first order approximation, carriers (i.e. gain) are constant above threshold. This phenomenon, called **carrier pinning**, or **gain clamping** describes the fact that further increase in injected current (i.e. output power) will NOT change the carrier density, neither the gain curve inside a semiconductor laser.

Another comparison is quite enlightening here. Gas lasers have a density of active atoms which is orders of magnitude less than that of semiconductors. Furthermore atom excitation is sometimes more tricky in a gas laser. This is the main reason why lasers of comparable power, made from gases are macroscopic in size whereas semiconductor lasers are mm long and usually more efficient.

2.1.1 Edge emitting laser diodes

Laser diodes may be categorized in two groups based on the laser radiation direction of propagation. Edge emitting laser diodes are designed in such a way that light travels parallel to the growth axis. All devices fabricated in this work, are edge emitting devices. The alternative, namely laser diodes that emit perpendicular to the surface (VCSEL) will be shortly described in paragraph 2.1.2.

Waveguiding

In order to contain the light inside the active area of the semiconductor laser, there is a need to create some wave-guiding effect. Looking at the two dimensions perpendicular to the light propagation axis, we may identify two different mechanisms. On the growth axis, the one

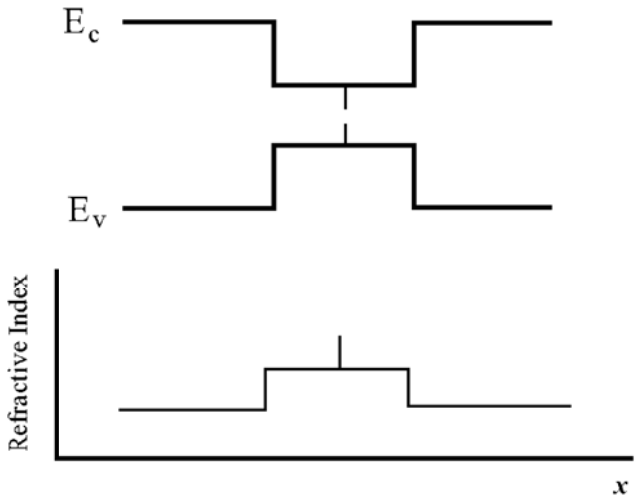

Figure 2.3 *um well separate heterostructure laser diode.*

perpendicular to the substrate, the layers of the heterostructure, have a different refractive index. Luckily, higher band gap semiconductors have a lower refractive index. Thus, the carrier containment discussed in the previous paragraph simultaneously serves as wave-guiding medium. A higher refractive index material is placed in the center of the laser diode (waveguide core) whereas a lower refractive index material (i.e. higher bandgap, cladding layer) is used to confine photons within the active region. Fig.2.3 depicts the bandgap as well as the refractive index profile along this axis.

On the axis parallel to the substrate, waveguiding is achieved either by replacing the semiconductor material with a higher bandgap semiconductor (regrowth) or – at the extreme case – by air (etching). A similar refractive index profile to the one depicted in Fig.2.3 is thus achieved, creating a waveguide effect. The advantages of simultaneously achieving carrier confinement apply to this axis as well.

Fabry – Perot cavity

The simplest way to create an optical cavity, is to place two flat mirrors parallel to each other. Reflected photons will bounce back into their original track after two reflections.

Semiconductor have high refractive indices. If a photon impinges on a flat, semiconductor-air interface, the reflection probability, is associated with the refractive index contrast between the materials forming the interface. In case of an air-GaAs interface, reflection is approximately 32%. Forming two parallel semiconductor-air interfaces at the sides of a semiconductor, is enough to obtain a Fabry-Perot cavity.

GaAs material, as well as most compound crystalline semiconductors, have a non-isotropic

crystal structure. There are some crystal orientations, where the atomic bond surface density is minimum. Upon crystal breakage, the fracture energy required scales with the bond energy and the number of bonds per unit surface. Crystal fracture will therefore occur easier in the planes discussed. This is called cleaving and is heavily used in semiconductor laser industry. The resulting surface is an atomically flat surface, always oriented along such a plane. Cleaving the crystal twice, will provide two, atomically flat, parallel semiconductor-air interfaces (facets). In other words an optical cavity. Further coating the exposed facet with highly reflective material may increase the native reflectivity.

In a Fabry – Perot cavity of length *l,* where light is traveling with an effective refractive index n_{eff}, the modes that may be sustained are given by the simple relation (round trip phase matching):

$$l = \frac{m\lambda}{2n_{eff}} \tag{2.2}$$

m is the **mode index** (an integer) that is a large number in edge emitting cavities. Using Eq.2.2 the spectral distance between adjacent cavity modes may be obtained. Obviously the shorter the cavity, the sparser the modes sustained. A Fabry – Perot cavity laser may only lase in one of these modes. Edge emitting devices have typical cavity length in the order of a several 100's of μm's. This corresponds to a mode spacing in the order of a nm or less. Given the fact that gain is broad, covering several 10's of nm, and the top of the gain spectral curve is rather flat, these devices are expected to lase in several longitudinal modes (i.e. several wavelengths).

In certain applications multi-mode emission is not tolerable. Due to this, plain facets are often replaced by more elaborate solutions. Both Distributed bragg reflectors (DBR) and Distributed Feedback Lasers (DFB) all take advantage of the notion of a periodic modulation of the refractive index. The periodicity results in wavelength selective reflectivity that ensures (see Eq.2.1) that only one longitudinal mode – the one with wavelength matching the maximum of the reflectivity – will obtain enough feedback to lase. These devices operate in **single mode**.

Summary of edge emitting laser diode characteristics

Edge emitting laser diodes are easy to build and are cost-effective. Since they have a high active material volume, they may emit high power output. Single mode operation may be obtained using DFB or DBR wavelength selection.

There are however some disadvantages inherent to the EELD. To begin with, emission is parallel to the semiconductor surface, making integration of these devices complicated. Furthermore, special design is necessary to obtain TEM_{00} operation (lateral mode control). Because the EELD's waveguide is usually strongly asymmetric (the growth axis thickness is much less than the lateral confinement) the beam is astigmatic. Astigmatic beams are difficult to couple into fibers and/or focus down to diffraction limited spots. Finally, since device size may not be reduced arbitrarily – typically in the order of 100's of μm – significant operation current is necessary, even for low power devices.

2.1.2 Vertical Cavity Surface Emitting Laser diodes (VCSEL's)

Attempts to address the disadvantages of edge emitting lasers, resulted in the design of the

vertical cavity surface emitting laser diodes (VCSEL's). The key technology was the accurate growth of heterostructure Bragg reflector stacks. These devices feature two highly reflective mirrors made from alternating material. Radiation propagates perpendicular to the substrate surface thus no cleaving is necessary. Since the cavity length is comparable to the operating wavelength, these devices are by nature operating in single longitudinal mode.

The light interaction with the active material is significantly decreased thus modal gain is drastically reduced. However, this is compensated by high mirror reflectivity (>90%). The resulting devices have small output power but exhibit a series of unique characteristics. The beam is free of astigmatic effects making it easy to couple into fiber optics, devices are functional without separating them from the wafer thus allowing arrays to be manufactured. Furthermore, the current needed to achieve lasing is smaller compared to EELD.

These devices are complicated to fabricate and involve sophisticated growth, and fabrication techniques (i.e. oxidation). A detailed description of the VCSEL's is out of scope for this document.

Section:2.2.Semiconductor laser tuning

As discussed in the previous section, semiconductor laser emission wavelength, depends on the gain of the material and the modes that the associated cavity may sustain. Each cavity mode is characterized by a gain and a loss value. If a mode satisfies Eq.2.1 it will emit laser radiation. In the contents of this discussion, multimode operation may be ignored. Two ways to make a laser change emission wavelength are evident, either dynamically change the gain curve, or shift the modes of the cavity. The first one will result into emission hoping between adjacent modes as the gain maximum shifts through the vicinity of each mode. On the other hand, the second one will shift the emission following the change in the dominant mode up to the point where either a different mode becomes dominant or the gain is no longer enough to sustain lasing.

An ideal tunable laser [18] would exhibit continuous tunability (no hoping) and no intensity changes during tuning. In other words, an ideal tunable laser diode would have two completely independent inputs. One to change the output power and one to change the wavelength. However, real device operation is still far away from this picture. [19]

2.2.1Cavity mode tuning

As already discussed, single mode emission requires Bragg reflectors (DFB or DBR). These devices work by spectrally filtering the cavity feedback. In such a cavity design the critical factor in wavelength emission shift is the DFB/DBR wavelength tuning.

Changing the spectral behavior of such a device, requires changing the periodicity (actual dimension change) or changing the refractive index of the layers. The latter is appealing given the fact that refractive index may dynamically change.

There are three basic phenomena that may modify the refractive index of a material.

Free carrier effects

Introducing free carriers in a semiconductor has a two fold effect on the refractive index. There is free carrier polarization effect and there is also absorption modification. Both changes result in

refractive index change [20] [21] [22]. To create the effect, carriers have to be injected into the semiconductor region. In order to obtain a significant refractive index change, the band gap of the tuning material has to be close to the photon energy. To date,the maximum relative refractive index change reported is 0.04 [23].

Electro-optic effect

The **quantum confined Stark effect** (QCSE) may be used to modify the refractive index through absorption changes. If a quantum well is biased, the electric field modifies its electronic states. In fact, the higher the electric field, the lower the ground electron-hole state separation. Corresponding devices usually utilize a multi-quantum well structure (two enhance the interaction) under reverse bias. The higher the reverse bias, the higher the QCSE and accordingly the higher the refractive index change [24], [25]. Contrary to the free carrier effect, this approach does not dissipate power since no carriers are injected. The effect is however weaker reaching a maximum relative refractive index change of 0.01.

Thermal cavity mode tuning

The refractive index is also sensitive to temperature changes. This has been extensively used to provide tunability [26] of the cavity modes of laser diodes. DFB and DBR gratings shift their wavelength characteristics at a rate of 0.1nm/K. A word of caution regarding thermal effects: Gain is also affected by temperature. Gain thermal tuning (which will be discussed later on) is a different mechanism and should not be mixed to the concept discussed here.

Device applications

Based on the previous concepts, numerous tunable devices were implemented. It is significant to have an overview of the performance and the drawbacks that these devices have. Knowledge of the existing solutions may clarify which is the novel or improved tuning characteristics that the concept proposed in this work may provide.

2.2.1.1Two-section DBR laser

The cavity in a two section DBR laser, consists of an active section providing the gain, and a DBR section that is controlled by a separate electrode. [23] Several ways to control the DBR refractive index have been devised (active DBR, passive DBR) so far. These diodes provide a quasi-continuous tuning behavior exhibiting up to 10nm tuning range. Although the DBR reflection is tuned, changing the emission wavelength, the device hops between adjacent cavity modes. The later are fixed by the main cavity. This discontinuous tuning mode is unacceptable in some applications.

Finally, even if the DBR is tuned, the gain curve remains unchanged. Thus the gain experienced by the lasing mode changes. Thus the output power may not be stable. The maximum tuning range is mainly limited by the DBR tuning range.

2.2.1.2Three-section DBR laser

Adding one more section to the previous design, so as to tune the main cavity modes, enabled

quasi-continuous wavelength tuning. [27] By quasi continuous tuning, the situation where all wavelengths may be addressed but the device may not scan through the tuning range in a continuous and predictable way. The extra section added, acts as a phase delay which permits cavity mode shifting. Practical quasi-continuous tuning ranges achieved are in the order of 10nm although up to 17nm discontinuous tuning has been reported [28]. The main drawback of such devices is the fact that both control electrodes have to be simultaneously controlled. This necessitates sophisticated control electronics.

2.2.1.3Multisection DFB laser

Much like multi-section DBR tunable lasers, DFB lasers may also be tuned [29]. The main advantage of multi-section DFB laser devices is the ease of fabrication. No additional regrowth is necessary. The only difference between a non-tunable and a tunable DFB laser is the fact that the top electrode is divided in two or more sections. In order to enhance the significance of the DFB grating, the facets in DFB lasers are usually coated with anti-reflective coatings. The best results were obtained for three section symmetrical DFB tunable lasers that have exhibited a 7nm tuning range in the IR [30].

2.2.1.4Transverse twin guide DFB laser

Instead of integrating the tuning and gain regions longitudinally, transverse integration is also possible [31]. Instead of a PN diode, a PNP structure is grown and three electrodes are formed. A bottom and a top P contact and one N contact in the middle. One PN contact is responsible for the gain control and the other one is used to provide tuning. Although device design is much more demanding, these devices have successfully exhibited continuous tuning in the order of 7nm. The limiting factor in these devices is not tuning limitations, it is rather the gain curve which diminishes for large $\Delta\lambda$ [32].

2.2.1.5 Striped thermal DFB laser

Since thermal effects also tune DFB [33] and DBR [34] devices, a heater may be integrated on top of such laser devices. The heating element is a resistive metallic stripe placed directly on top of the laser diode. To insulate the stripe from the laser, a thin oxide is used. This method has been extensively used, not only to create tuning on simple, non-tunable devices but mainly to extend the tuning range of the previously mentioned devices. The main disadvantage of the technique lie sin the fact that thermal effects enable a time response in the order of a μs. Thus the speed of tuning is significantly less than that of the devices described in the previous paragraphs.

VCSEL external cavity tuning

Much like the DBR described above, a VCSEL may be tunable by shifting the cavity mode. However, since the cavity is now extremely small, refractive index changes are not enough. Tunable VCSEL's utilize an external cavity design [35]. The top mirror is suspended on an elastic structure. Two electrodes, one on the top mirror and one on the underlaying surface are placed and an electrostatic force is applied to the suspended mirror. This results in a change of the distance of the mirror from the rest of the structure, thus changing the cavity length. In this concept tuning

implies mechanical movement of the mirror. This makes tuning slower than the DBR's. Furthermore, the voltage needed to tune these devices is rather high because of the stiffness of the mechanical support that holds the mirror suspended.

2.2.2 Gain tuning

The previous section described cavity mode tuning, there are however other approaches to tunable laser diodes.

Temperature tuning

The simplest way to "tune" a semiconductor emission is to vary the temperature. The bandgap energy is sensitive to the temperature thus when cooling a device the emission is expected to blue shift. As an example, the bandgap energy of GaAs is 1.519eV at 0K whereas it is 1.424 at room temperature. This corresponds to emission from 816 to 870nm. Further increase of the temperature may provide more shift toward the red part of the spectrum.

There have been many applications of temperature tuning especially for optical pumping of solid state lasers e.t.c. Although the tuning range is large, this technique has a series of drawbacks. To begin with, no wavelength selection mechanism (i.e. DBR, DFB) may be present in the device. This is due to the fact that such a system sets the emission wavelength, thus not allowing the device to lase at the gain maximum which is the one that exhibits the large shift. In fact, in order for this technique to work properly, the cavity modes have to be closely spaced so that the device may hop from one cavity mode to the next.

Finally, changing the temperature of the device involves a temperature control stage with the associated feedback electronics. This results in tuning time in the order of a sec which is prohibitively large for some applications. Integrating the heating element as described in cavity thermal tuning, will provide a faster response but still nowhere close to the Ghz scale which is required.

Quantum Confined Stark Effect (QCSE) tuning revisited

It has already been discussed that contemporary laser diodes utilize a quantum well system to induce refractive index changes through the QCSE. This effect, although weak, has provided significant tuning in the concepts mentioned so far. Implementing an active QCSE based device has not been proposed. Such a device would use this effect to tune the gain spectra of the device, as well as the refractive index. It has been assumed, that large carrier density existing in an operating laser device will screen electric fields, not allowing any significant stark effect to be sustained. So far, the only gain tuning mechanism proposed is thermal shift. This is however too slow for a large number of applications that require fast tunability. QCSE, on the other hand, is only limited by electric field change rate which is certainly orders of magnitude faster. In fact similar speed to the free-carrier effects are expected.

Part I: Growth and optimization of laser diode structures

Chapter 3. Semiconductor crystal growth

In order to implement any of the discussed ideas in practice, one needs to obtain a carefully tailored semiconductor structure. This chapter will briefly introduce the main points concerning semiconductor material growth.

Section:3.1.Crystalline semiconductors

The word semiconductor defines an extremely broad group of materials, both amorphous as well as crystalline. Our interest, is in crystalline semiconductors and specifically compound semiconductors of the III-V group with As as the V group material. It should be noted however, that the concept presented in this work may be applied to any semiconductor capable of light amplification.

III-As crystallizes in the zinc-blend structure. Depending on the group three element, it is possible to tailor the bandgap from 0.7eV (InAs) to 2.2eV (AlAs) including all intermediate values.

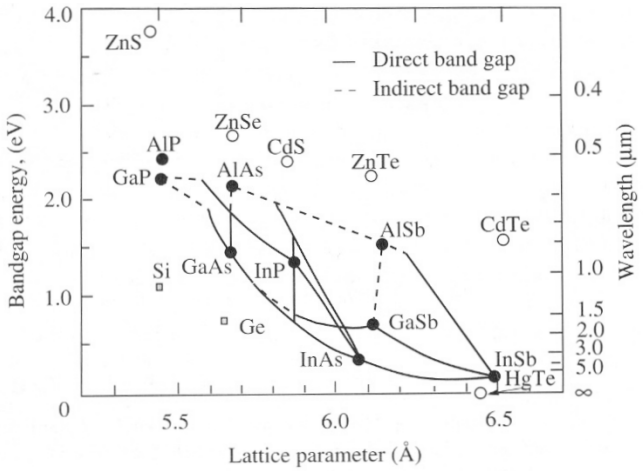

Figure 3.1.: Plot of the bandgap energy with lattice constant of various known semiconductors. Solid lines represent direct bandgap alloys whereas dashed lines correspond to indirect bandgap materials.

The lattice constant of the materials that may be grown on a substrate is determined by the lattice of the substrate. In the plot shown in Fig.3.1 this translates into a vertical line that corresponds to the lattice constant of the substrate material. The main advantage of compound

semiconductors is the fact that layers with different bandgap have the same lattice constant and thus may be combined in a single crystal. For GaAs substrates, alloys containing Al with arbitrary Al mole fraction may be incorporated into the grown crystal. As will be discussed later in this chapter, a situation where the lattice constant rule may be relaxed up to a certain point is possible. This allows for InGaAs to be grown as well on GaAs as long as the In mole fraction is small and/or the layer thin enough.

Section:3.2.Crystal growth, Molecular Beam Epitaxy

The process of extending a single crystal is called epitaxy after the greek word "επίταξη" which stands for put on top with order. If one could pick and place atoms of the constituent materials on the surface of the semiconductor crystal, it would be possible to gradually extend the crystal. Varying the kind of atoms that are placed would result in heterostructures. That is a layer by layer combination of different materials in the same crystal.

There are several techniques to grow semiconductor crystals. Some of them are "Liquid phase epitaxy (LPE)", "Metal-organic chemical vapor deposition (MOCVD)" and "Molecular Beam Epitaxy (MBE)" [36].

3.2.1 Crystal heating – surface mobility

It is easy to direct atoms of a specific element towards a crystalline surface. However this is not enough to extend a single crystal. If one were to try this at room temperature, atoms would adhere at random places thus an amorphous material would be formed. Raising the temperature of the crystal high enough, a series of interesting phenomena would appear. Initially, the atoms reaching the surface would have enough energy to move along the surface thus reaching a crystal site. These places are energetically favorable since they are the places were atoms may form the most bonds. On the other hand, some of the atoms may re-evaporate because of the increased temperature. Finally if the temperature is high enough the crystal itself may decompose allowing atoms to escape.

It turns out that for the III-As crystal there is a temperature range were the best of both worlds may be obtained, enough surface mobility to place the atoms in their proper lattice sites but not enough thermal energy to cause significant decomposition of the formed material. At this temperature range, As atoms that reach the surface, re-evaporate unless they become part of the crystal. The incoming flux of III atoms decides the growth rate of the crystal and it is only necessary to provide enough As atoms. A slight abundance of As atoms will cause no trouble as the excess As will re-evaporate. These conditions provide a set of parameters at which III-As semiconductors are grown [37].

3.2.2 Material sources

In order to grow a crystal made from Ga and As, we obviously need Gallium and Arsenic atoms. Given the fact that these elements exist in nature in the form of pure material, it is possible to use an effusion cell to provide the needed species.

If a material is heated up, it's vapor pressure increases. If we assume a closed container partially

filled with an element i.e. Gallium, we may obtain the Ga partial pressure in the container using the Clapeyron equation [38]. Making an orifice in the container will allow Ga atoms to exit the container at a rate which depends on the orifice size and the partial pressure inside the container. In simple words this is a "Ga atom beam". Changing the temperature of the container will change the pressure of Gallium and thus change the flux exiting the contraption. This is called a Knudsen cell or in short a K-cell.

Similar logic may be applied for any element that may be in solid or liquid form, at room temperature. In a molecular beam epitaxy system, a series of K-cells exist, one for each element. Temperature control of the cell enables a beam flux with an accuracy of better than 1%. Long term stability of the K-cell flux–temperature relation is changing because material inside is depleted and/ or the evaporation surface changes. Thus it is necessary to periodically calibrate the flux for each cell.

K-cell	*Typical operating Temp.*	*Use*
Ga	1040-1100 ºC	III group
Al	1070-1140 ºC	III group
In	850 ºC	III group
As		V group
Si	1230 ºC	Donor
Be	850 ºC	Acceptor

Table 3.1: Available elemental K-cell sources in III-As MBE reactor.

3.2.3 Vacuum chamber

In order for the elements evaporated from the K-cell to reach the surface of a crystal, it is expected to travel a macroscopic distance (i.e. a few cm). Direct travel in the form of a molecular beam, is only possible at very low ambient pressure. This is the first reason why an MBE process requires an ultra high vacuum (UHV 10^{-11} – 10^{-9} Torr) chamber. The mean free path in this pressure regime is very large allowing for the atomic flux exiting the K-cells to reach the crystal to be grown.

However, the main reason that UHV conditions are required, is the fact that an ultra pure crystal needs to be grown. Typical intentional doping concentration is seldom more than 10^{18} cm^{-3}. If a contamination of only 1ppm (10^{-6}) existed in the grown crystal, the non-intentional doping would be $10^{17}cm^{-3}$ which is extremely high. To minimize stray atoms that may contaminate the grown crystal, the MBE chamber has to operate at UHV conditions.

Furthermore, a cryo-panel is placed between the walls of the chamber and the crystal to be grown. This is cooled at cryogenic temperature, thus any atoms leaving the wall of the chamber are trapped on the panel instead of reaching the sample. Even though these seemingly extreme precautions are taken, non intentional doping is typically in the range of $10^{14}cm^{-3}$ for the material system described.

3.2.4 Summary

In short, the molecular beam epitaxy system is an ultra high vacuum chamber equipped with a set of temperature controlled elemental sources that provide the constituent atoms to form a semiconductor crystal. An initial crystal is required as the base where the new crystal is to be

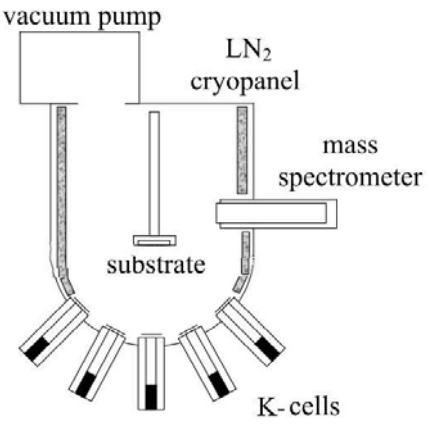

Figure 3.2.: Schematic of an MBE system.

grown. These are substrates – wafers of the same material (homoepitaxy) grown by bulk crystal growth methods. The crystal is heated up to a temperature range were thermal energy allows atoms to reach their proper atomic places and thus extend the crystal. A set of shutters control the fluxes thus facilitating control at the atomic layer level of the crystal's composition [39] [40].

Section:3.3. MBE Apparatus

The MBE equipment used to produce the III-As samples for this study, is a VG 80H Molecular beam reactor. The chamber is maintained in ultra high vacuum (UHV) by a system of ion and sublimation pumps. During growth, a set of cryo-panels ensures that minimum residual gases remain in the chamber.

III-V elements available to grow the semiconductor crystal are supplied by a set of K-cells with In, Ga and Al corresponding to the group III element and As corresponding to the V group. Furthermore, a set of doping sources, namely Si and Be exist, so that both N and P type doping may be achieved respectively.

Both the temperature for each source cell, as well as the substrate temperature are controlled. Finally, an ion gauge is used to measure the equivalent pressure of element fluxes in order to accurately control the growth process.

Section:3.4. Pseudomorphic growth

As pointed out at the beginning of this chapter, crystal growth is restricted by the lattice constant of the host material. A different lattice constant epilayer would mean that atoms have to be placed at different interatomic distances than the native crystal sites. This rule however may be slightly bent. If two materials have the same crystal structure, yet slightly different lattice constants, then it would be enough to deform one or the other thus accommodating the atoms and making both crystals follow a single lattice constant.

The energy of the deformed crystal is larger than the native one. Up to a point, it is possible to grow such a pseudomorphic layer. Eventually the deformation energy becomes large. After a certain point, the energetically favorable state of the crystal is no more a layered smooth growth but

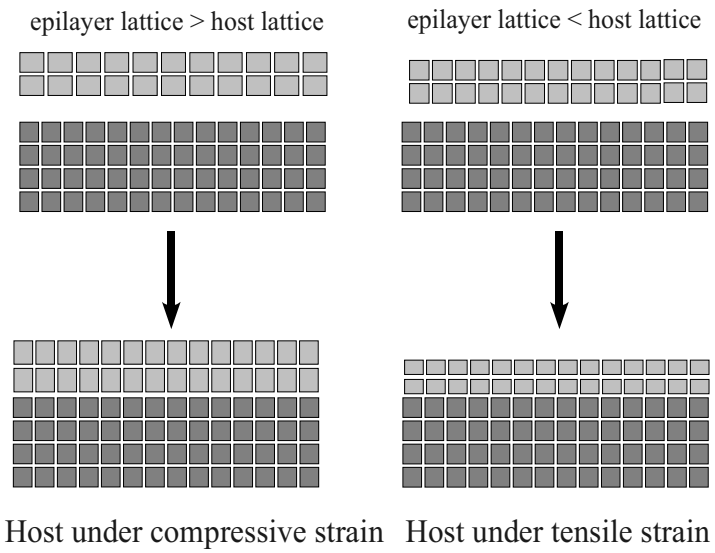

Figure 3.3.:Schematic representation of pseudomorphic growth for two cases: a) when the grown layer has larger lattice and b) has a smaller lattice constant

rather crystal defects or rough surface. The small, but significant, window of layered (two dimensional) pseudomorphic growth allows for example InGaAs thin layers to be grown on GaAs, even though the two materials have a different lattice constant.

Pseudomorphic growth is technologically important for many reasons. To begin with, the pool of materials that may be grown on a single wafer broadens. Additionally, strained layers exhibit a series of interesting electrical and optical behavior that semiconductor industry has taken advantage of. In what follows some of these effects – that are of special interest for this work – will be thoroughly described.

Chapter 4. Structure characterization methods

This chapter briefly describes established techniques both in terms of scientific knowledge as well as in our group. These tools are generic and frequently used in semiconductor characterization for a variety of fields. The insight gained using these techniques are mainly specific to crystalline quality and morphology.

Section:4.1. X-ray diffraction measurements (XRD)

X-ray diffraction measurements were performed on some samples to obtain information regarding the quality of the grown crystal structure. Thus it is useful to briefly introduce the method and describe which information one may obtain using this tool.

4.1.1 Principle of operation

Any crystal is made from a highly periodic lattice [41][42]. III-As based materials crystallize in the zinc-blend structure which is a cubic lattice. When an electromagnetic radiation impinges on such a sample, each crystal site i.e. an atom, acts as a scattering center. The scattered radiation interferes producing a diffraction pattern which is characteristic of the crystal and the wavelength of the impinging radiation. In order for this effect to be observed, the wavelength of the radiation has to be comparable to the inter-atomic distance, thus in the order of an Angstrom. This radiation is in the x-ray range.

X-ray diffraction has long been used in solid state as a powerful scientific tool. Several methods have been invented each focusing on a specific field of interest. In this work the field of interest is mono-crystalline materials which need to be characterized in terms of quality, layer composition and thickness [43] .

Depending on the structure of the sample, the incidence and scattering angle, the scattered radiation may interfere either constructively or destructively producing a strong diffraction at specific angles and almost no intensity elsewhere. The governing equations will be shortly described.

The periodicity of a crystal is described by the reciprocal space vectors. Each plane may be

characterized by three indices (miller indices). Thus for a family of parallel planes we have:

$$\vec{H}_{hkl} = h\cdot\vec{b}_1 + k\cdot\vec{b}_2 + l\cdot\vec{b}_3 \tag{4.1}$$

Where b_i are the reciprocal vectors and *h,k* and *l* are the **Miller indices**.

The distance between two adjacent parallel planes is easily found and is given by:

$$d_{hkl} = \frac{1}{|H_{hkl}|} \tag{4.2}$$

In order to obtain constructive interference, the path difference of the beams diffracted at the interfaces (i.e. the two crystal planes) has to be a multiple of the wavelength λ, thus we obtain:

$$\frac{\vec{S}-\vec{S}_0}{\lambda} = \vec{H}_{hkl} \tag{4.3}$$

Where S is the vector describing the diffracted beam path and S_o is the unitary vector describing the impinging beam path as shown in Fig.4.1. Eq.4.3 is the well known **Bragg law** and is the main governing equation in crystallography. An immediate result of this equation is that in order to have diffraction, the wavelength λ must be $\lambda<2d_{hkl}$ and given the fact that atoms are a few Angstroms apart λ has to be in the x-ray range. When Eq.4.3 is satisfied, a strong intensity will be recorded in the x-ray sensor, conversely, when the angle is different, the intensity will drastically drop.

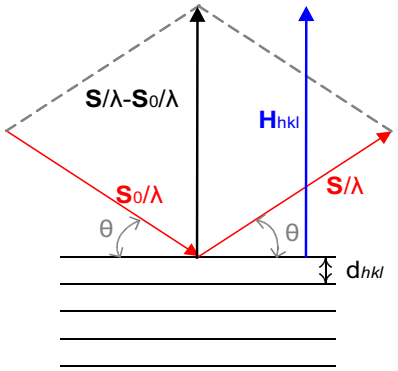

Figure 4.1:Mathematics of crystallography: S_o is the impinging radiation vector, S the diffracted beam and λ the wavelength. d_{hkl} is the interplane distance

Depending on the crystal structure and the feature of interest, a diffraction peak is selected (corresponding to a set of miller indices) and an angle scan of the diffracted intensity is recorded. This is symmetric ω-2θ scan and is the most common way to measure a sample in semiconductor crystallography.

Since scattering depends on atom size and inter atomic distance, the recorded data contain information that reflect both crystal quality as well as structure information such as layer thickness and composition.

4.1.2 Experimental setup

The group is equipped with a high resolution diffractometer BEDE D1. The following figure

depicts a simplified schematic.

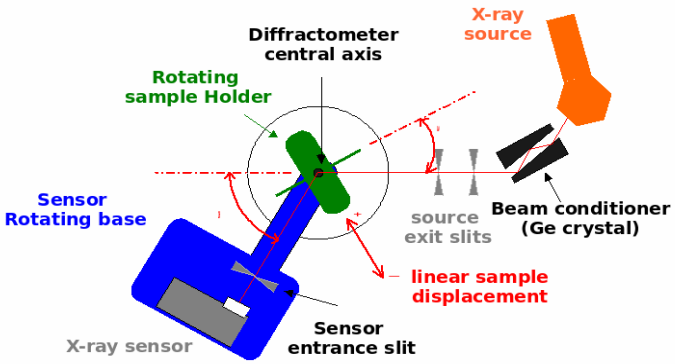

Figure 4.2:Schematic of Bede D1 diffractometer top view

The X-ray source is a 2KWatt water cooled copper cathode Roentgen tube. The emitted x-ray line is at λ=1.54051Å (Cu K_a1 line). A Ge beam conditioner is used to filter out any other x-ray radiation. The source is completed with a double/triple slit setup to ensure beam collimation. The sample holder is a high precision 4-angle motor stage. As shown in Fig.4.3 there are 4 degrees of freedom thus the "4 angle" name. Additionally it is possible to move the sample holder perpendicular to the sample so that the center of rotation coincides with the reflection point on the sample. It is important to align the sample to the diffractometer before a measurement is performed [44].

Parameter	*Range*	*Resolution*
Θ	280˚	0.18 arcsec
2Θ	235˚	0.18 arcsec
Tilt goniometer	40˚	0.01 degrees

Table 4.1: Range and specifications of bede D1 system

The sensor consists of a photon counting device and an entrance slit. The slit ensures that a narrow angular content of the beam is sensed. Depending on the intensity of the diffracted beam, a long averaging may be necessary to obtain a noise free plot. Thus a scan may be hours long.

The system is computer controlled facilitating automated measurements for a range of each controlled parameter.

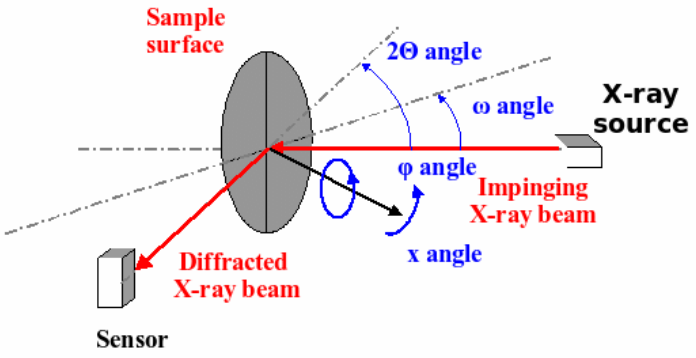

Figure 4.3:4 angle x-ray measurement setup

As already described, an ω-2θ scan is taken for a specific plane family (described by a set of hkl indices). This means that an x-ray intensity with angle plot is recorded. The data are then analyzed as described in the next section to extract the useful parameters.

4.1.3 Data analysis

Analyzing XRD data is by itself a complex field [45]. Theoretical prediction of the XRD intensity data can be calculated solving Eq.4.3 for each angle of interest. Of course the interesting part is to extract thickness, composition and lattice constant data from the acquired spectra.

There is a software tool, accompanying the instrument, that completes this task as far as thickness, composition and lattice constant are concerned. The program accepts as input the collected data, and a layer by layer description of the structure. Finally, a range is set for each parameter. The program uses a trial and error genetic algorithm to obtain the best fit and calculates confidence levels.

The output is a corrected structure description which corresponds to the measured XRD data along with an error estimate for each fitted parameter. Depending on the Miller indices that the experiment is performed, there is a different sensitivity to each parameter of the structure. It is thus important to select the reflection that will provide increased sensitivity to the parameter if interest. Much like an optical etalon, multiple reflections are possible from interfaces. This creates shuttle

peaks which provide an indication of the roughness in the interfaces. This technique is used to characterize thin layers such as quantum wells.

In summary XRD measurement is a sensitive tool to check the grown material quality. That is the reason it was used to characterize samples in this work.

Section:4.2. Scanning Electron Microscopy (SEM)

It is well established since Rayleigh that optical microscopy is limited by the wavelength of the light used to visualize a sample. When higher resolution is required, electron microscopy is used. In principle, electron microscopy is limited by the De Broglie wavelength of the electrons which is orders of magnitude smaller than that of visible light. Using electrons in imaging although simple in principle, requires technologically advanced equipment. In what follows, a brief description of electron microscopy is attempted in order to reveal the capabilities and weaknesses of such equipment.

4.2.1 Principle of operation

Scanning electron microscopy or alternatively secondary electron microscopy, uses a focused electron beam to scan the surface of a sample. This way, a high resolution image of the sample is acquired and displayed on screen [46].

Producing electrons is straightforward. There are two methods to achieve this. Each material has a work function. In other words, there is a certain amount of energy that an electron inside a bulk material needs to escape into vacuum. This energy can be either provided thermally (hot filament) or through an electric field.

Hot filament electron emission is common knowledge. Electronic tubes, cathodic ray tubes (television) are common examples of hot filament electron emission. Each electron obtains energy from the hot lattice and a significant number of electrons, having energy above the work function can escape. It is evident that metals with low work function are preferred.

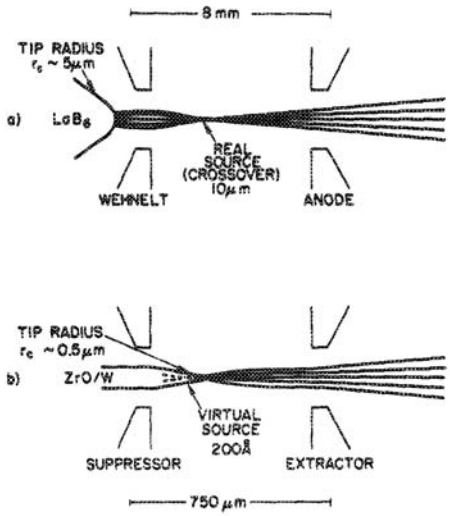

Figure 4.4:Electron guns used in modern SEM instruments. The difference in source size is evident. Reprinted from [47]

Hot filaments can produce large number of electrons (high emission current) and have low cost. The only disadvantage of this method is the fact that electrons are emitted from a large area typically in the order of a few μm in diameter.

Field emission is based on the fact that electric field changes with the radius of curvature of an equipotential surface. Thus, if we have an acute tip and an electric field is applied, the edge of the tip will experience an electric field much more intense than the rest of the body. Choosing a low work function material and heating the tip allows electrons to escape just like the hot filament emission only this time they escape only from the edge of the tip [47].

Recently, cold field emission sources have been manufactured. Such electron sources do not use thermal energy to emit electrons and thus produce electrons with less energy dispersion and from a very small area, of the order of a nm^2.

The emitting area, the energy dispersion of the electrons and the emission current are the main characteristics of an electron source. The smaller the emission area and the energy dispersion, and the larger the emission current the better resolution an electron microscope may achieve.

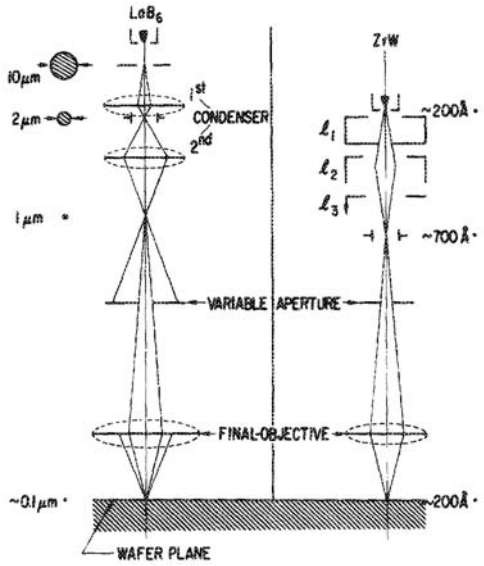

Figure 4.5:SEM column, the electrostatic lenses that demagnify the initial electron beam may be seen. Reprinted from [47]

Emitted electrons are accelerated by a high voltage typically in the KVolts range. This translates to smaller De Broglie equivalent wavelength, thus a better resolution. A set of electromagnetic lenses focuses the beam down to a minute spot. As in any projection system, either optical – focusing photons – or electronic – focusing electrons, the smaller the source the smaller the final spot.

The spot is focused on the surface of the sample. There, electrons impact on the sample, they transfer energy and secondary electrons are produced. In a mechanistic analog, imagine a ball falling at high speed in a container with balls, many of them will bounce around. Of course, depending on the surface material and morphology more or less secondary electrons will be produced.

A small voltage (few hundred Volts) is enough to direct those electrons into a measuring device. Moving the spot around, each site on the surface may be probed. In fact, each SEM is equipped with a pair of deflection plates that steer the electron beam in X and Y direction. This way, a scan of the area of interest, much like an old TV screen, is obtained. The intensity map of secondary electron emission thus forms an image of the sample's surface. The resolution of this method is only limited by the size of the focused electron beam on the surface. Routinely the resolution of an SEM is in the nm range.

An important drawback exists on electron microscopy. In case of non-conductive samples, the excess electrons impinging on the sample are trapped on the surface. This creates a repulsive potential which builds up with time. The beam is thus deflected away from its initial position. Furthermore the excess electrons cause a large emission of secondary electrons, in the area, cluttering the image. In order to obtain a high quality image, it is important that electrons have an escape route towards ground. In simple words, only conductive speciments may be viewed in an electron microscope. In order for an insulating sample to be examined, a thin conductive coating is

necessary so that electrons can escape through the conductive coating. Au or C sputtering is used in such cases.

The charging effect exhibited by dielectrics may hinder optical imaging. Nevertheless it may prove to be useful as well. Examination of a dielectric surface in a SEM imaging system may readily reveal the quality of electrical isolation that layer may provide. A good layer will exhibit strong charging effects whereas a leaky or conductive layer will show no charging effects.

Semiconductor samples are no problem as far as conductivity is concerned although careful grounding of the sample is important. Caution is necessary when dielectrics exist on the surface of the sample. In such a case, coating may be necessary to obtain a high resolution image.

4.2.2 Electron microscope instruments

Two SEM machines were used during this work. The first one was a hot filament emission SEM with a resolution of 100nm. This was the only available instrument for the majority of the lifespan of the project. Mirror quality, metal morphology, roughness are several key features that were evaluated using the electronic microscopy systems.

Near the end of this work, a new, hot field emission microscope (JEOL SM7000) was installed in our group. The resolution of this instrument is as high as 2nm. Most of the images shown in this text are taken using this high end imaging equipment.

For the sake of completeness, the following table summarizes the capabilities of the two electron imaging systems used in this work.

Parameter	*JEOL 940*	*JEOL 7000SM*
Gun type	Filament	Th. Field Em.
Acc. Voltage	1-20 KV	1-30 KV
Resolution	~ 200 nm	~ 1.5 nm

Table 4.2: Specifications of the SEM equipment used for this thesis

4.2.3 Summary

In summary electron microscopy is a powerful, high resolution imaging technique. In our work, SEM was used to check morphology of the etched areas, metal deposition and laser mirror smoothness. Finally as discussed, the charging effect was utilized to check dielectric quality.

Section:4.3.Photoluminescence measurements

In this chapter, photoluminescence measurements will be shortly described. Photoluminescence is a powerful technique routinely used to probe semiconductor samples. Keeping in mind that the purpose of this work is to create light emitting devices, photoluminescence acquires an even more serious role. It gives information about the samples ability to convert carriers into light.

The first section will describe the standard (time integrated) photoluminescence setup. With the advance of technology, time resolved photoluminescence is know possible. In this technique which is briefly described in the second section, not only spectral information is obtained but the sample's emission is followed in the time domain providing information regarding the carrier dynamics in the

structure under investigation.

4.3.1 Photoluminescence

Photoluminescence (PL) has been used for a long time and a vast collection of literature exists in the field. See reference [48] and references therein for a detailed description of PL related phenomena. PL is nondestructive and provides information about the band edges which is where 99% of the action takes place in a semiconductor. These two features make it an attractive characterization tool.

Principle of operation

When a semiconductor is under equilibrium, the carrier density is constant throughout the structure. No new carriers are created and no carriers are annihilated. Of course in such a case no photons are created in the structure. In case an external excitation creates some excess carriers, these will relax into their respective band and occupy some state near the band-edge. Finally, given enough time these carriers will recombine. In a direct bandgap semiconductor such as GaAs, carriers that recombine will most probably emit photons. This process is called luminescence. If the excitation of excess carriers is achieved using light which is absorbed in the semiconductor (obviously photons with higher energy than the bandgap) then the process is called photoluminescence.

Before recombining, carriers have enough time to relax inside the band they are created in. Relaxation is a fast process with characteristic time, in the order of 1-10psec. On the contrary, recombination is much slower. Thus carriers that recombine will almost always be at the bottom of their respective bands. This is why PL probes the band edges. Any shallow state at the band edge that can trap carriers is likely to exhibit a signature in PL. Furthermore, electron hole pairs form excitons which are shallow states and provide a unique signature in emission as well. In essence, PL is a tool that allows us to probe the band edge states of a semiconductor. Finally, as will be shortly described, PL intensity may provide an indication of light emitting efficiency in the structure.

Experimental setup

A standard PL setup was used to record luminescence spectra [49]. The experimental setup is depicted in Fig. 4.6. A short description of the main components will be presented in order to obtain an overview of the capabilities of the setup.

speciments are placed in a closed-loop He cryostat, able to cool down to ~10Kelvin. The front side of the vacuum chamber is a 2” quartz window that allows optical access to the sample. The cryostat is equipped with a heating element and a thermocouple controller. This enables setting the sample temperature anywhere from 10 to 350 Kelvin with an accuracy better than 1Kelvin.

A laser beam is used to optically excite carriers inside the sample. Depending on the bandgap of the sample, the pump laser wavelength is selected so that light will be absorbed preferably at the layers of interest. Thus, some degree of control as to where the excess carriers are created is achieved. A wavelength deep inside the absorption band (i.e. photon energy far above the bandgap of the material of interest) will provide high absorption, thus low penetration depth. Following is a

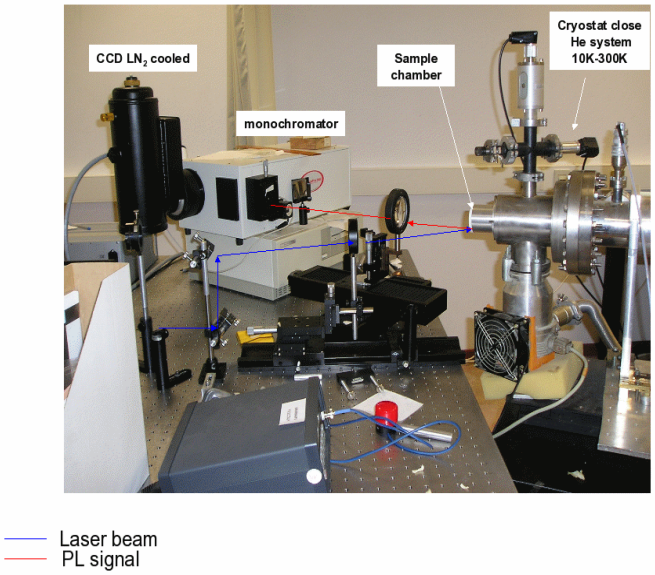

Figure 4.6: Photoluminescence setup. The main parts of the setup as well as the beam paths are marked on the picture. Reprinted from: "MRG internal report by M. Androulidaki"

table with the available pump laser characteristics.

Pump Laser λ(nm)	*Pump Power (mW)*	*Material to pump*
905 (Diode)	10	InAs
850 (Diode)	30	InGaAs
780 (Diode)	10	GaAs
650 (Diode)	7/35	$Al_xGa_{1-x}As$, x<0.25
532 (Yag doubled), pulsed	30	$Al_xGa_{1-x}As$, x<0.40
405 (Diode)	30	$Al_xGa_{1-x}As$, x<0.80/ InGaN
325 (He:Cd)	30	GaN
266 (Yag quadrupled),pulsed	6	$Al_xGa_{1-x}N$, x<0.50

Table 4.3: Pump lasers available for photoluminescence excitation. The last column shows some typical application material for each laser TODO

A small portion of the light emitted from the sample is collected using a large diameter lens. It is then coupled into a spectrometer. A Princeton Instruments ACTON 500mm monochromator was used. This spectrograph is equipped with 3 interchangeable gratings (150gr/mm, 600gr/mm and 1200gr/mm) and a liquid nitrogen cooled CCD array to acquire the spectrally resolved output. Following is a list of the basic characteristics of the setup. When a large wavelength region needs to be recorded with high resolution, several frames are recorded and are combined into a single plot extending beyond the range of a single image. Excitation of 650nm and 780nm was frequently used in our experiments. These wavelengths were selected in order to create carriers at or near the active part of the structure i.e. the InGaAs quantum well.

Grating	*Dispersion*	*Wavelength coverage*
150 g/mm	13 nm/mm	346 nm
600 g/mm	3.1 nm/mm	83 nm
1200 g/mm	1.4nm/mm	39 nm

Table 4.4: Dispersion and wavelength range covered in single shot using the 500mm spectrograph for each of the available gratings.

It should be pointed out that for indirect bandgap materials, it is difficult to obtain useful information from PL experiments, since these materials give very weak PL spectra. Furthermore there are structures where luminescence from one layer may be re-absorbed from another layer or worse a layer of similar bandgap may emit an overlapping spectrum. These cases are often encountered and turn the PL analysis into a complicated and tedious procedure.

Data analysis

The data obtained from a PL experiment is in the form of intensity vs wavelength. It is quite informative to obtain a set of measurements at different temperature values. Temperature dependent PL data are especially useful in the analysis of non-radiative effects.

Although Gaussian functions are routinely used to fit PL peaks, they provide little information concerning the physical mechanisms involved. Furthermore, asymmetric peaks as the ones recorded in the experiments described thereafter, are poorly fitted using gauss functions. Therefore a more fundamental approach was selected to analyze our PL data.

As known, the thermalized carrier population in a semiconductor is described by the product of the density of states (DOS) function times the Fermi Dirac probability distribution. When dealing with optical transitions, one may use the reduced density of states instead, thus taking into account both types of carriers necessary to provide a photon. Given the fact that the carrier lifetime in a given state is short and finite, according to the uncertainty principle, the product mentioned above is "smeared" in the energy domain, which in mathematical language translates to a convolution using a Lorentzian function. The following equations are thus enough to describe the problem. It should be noted that Eq.4.2 corresponds to the three dimensional density of states. Although in reality the DOS function corresponding to the dimensionality of each emitting layer should be used, this simplified approach has been found to adequately describe the PL data.

$$P_f = \frac{1}{1+e^{\frac{E-E_f}{kT}}} \tag{4.1}$$

$$D.O.S. \propto \sqrt{E-E_b} \tag{4.2}$$

$$f(x; x_o, \Gamma) = \frac{1}{\pi}\left[\frac{\Gamma}{(x-x_o)^2+\Gamma^2}\right] \tag{4.3}$$

where P_f is the Fermi probability and Eq.4.3 is the Lorentz distribution.

Using the approach described so far, one may fit the measured spectra using as adjustable parameters amplitude (I), center wavelength (λ_o), chemical potential (E_f) (what would be the Fermi

energy in a single type of carriers problem), thermal energy (kT) and the lorentzian factor (Γ). The resulting function which may not be given in closed form, describes the experimental data with very good accuracy and provides direct link to physical constants.

In order to implement this approach, a C++ algorithm was developed. (shown in Appendix TODO) The first step in the algorithm is to guess some initial values for the parameters. Then the parameters are fitted using a Levenberg-Marquardt algorithm. The algorithm finally outputs the best fit parameters along with a fit quality parameter.

In case the emitting layers are alloys, their composition is evaluated using the center emission wavelength λ_o. Composition information can be cross checked using the XRD measurements described in the previous chapter in some cases. This way the composition of the layers is ascertained.

The low energy side broadening of the PL peak is associated with band edge density of states (DOS). A high quality sample will have abrupt DOS band edge i.e. no tails or non-uniformity thus an accordingly abrupt PL. This is easily observed at low temperature where thermal effects are negligible. It is thus obvious that PL can provide information – to some extent – regarding layer uniformity. Especially when Quantum structures are probed, low energy side broadening is usually attributed to thickness non-uniformity of the quantum confinement structure [50].

Furthermore, exciton recombination which emits photons with energy below the band gap, provides a distinct signature in the PL. In high quality samples, the exciton recombination is dominant as long as the thermal energy is significantly below the binding energy of the exciton (5-10meV).

By increasing the temperature, there are a number of effects that enter into play. Besides bandgap change with temperature, the distribution of the carriers changes inside the bands. This leads to emitted photons with energies greater than the band edge. Thus, the high energy tail of the emission is more pronounced at high temperature. Overall, the emission peaks are broader and assuming that no carriers are lost, the spectrally integrated PL intensity (which is directly analogous to emitted photon number) should be constant.

Of course this is not the case in real samples as non-radiative recombination paths are enhanced with increasing temperature as well. With the increase of temperature, a significant number of carriers recombine without emitting a photon thus the spectrally integrated PL intensity diminishes. The extent to which this happens is a good figure of merit regarding non-radiative defect density. The more the defects and the more active they are, the less the luminescence persists with temperature.

It may be assumed for high quality material, that radiative efficiency (i.e. the portion of radiative recombination to the total number of carrier pairs annihilated in the structure) is very close to unity at low temperature. This assumption combined with the PL emission integral may provide some data regarding the quantum efficiency of the structure with temperature.

Improving PL analysis

The analysis described in the previous section has several pitfalls. To begin with, the true

density of states of the structure is not taken into account, but rather a simplified three dimensional parabolic band approximation is used. Furthermore, an arbitrary number of carriers is assumed to exist in the structure. In reality, the band structure as well as the excess carrier density i.e. the intesnity of excitation are significant parameters. A good example of such a case is piezoelectric structures were carriers partly screen the built-in field thus shifting the luminescence with excitation power. The full analysis of PL measurement begins with a detailed simulation of the structure under excitation. More detailed information regarding this will be provided in the following chapters when discussing bandstructure simulation.

The full schema to analyze PL and extract all useful information is much more tedious. More information will be presented when tackling the theoretical approach in the following chapters. The main points however are the following:

- Full bandstructure calculation (electron and hole density of states)
- Quantum effects (Schroedinger equation)
- Carrier relaxation and diffusion (to predict carrier density in each point of the structure)
- Exciton and doping states: carrier capture - release
- Non-radiative phenomena

The above requires tedious calculations and only recently have there been some attempts to fully develop simulation tools that predict and analyze photoluminescence data [51] .

4.3.2Time Resolved Photoluminescence

Besides traditional photoluminescence which gives valuable information for the band structure and the sample quality, modern technology allows us to follow the time evolution of the emission from a semiconductor structure. An ultrafast laser beam (Ti:Sapphire) (P_{width} < psec) impinges on the sample exciting carriers. The emission from the sample is collected using an optical lens system and then is spectrally resolved using a spectrometer. Finally the intensity of the emission is recorded using a streak camera. A streak camera is equipped with a two dimensional optical sensitive array (CCD or CMOS). One dimension corresponds to the wavelength and the second one is scanned with time thus giving a temporally and spectrally resolved emission of the sample.

Principle of operation

In time resolved PL, the idea is to follow the intensity of the emitted radiation from the sample in time. Given the fact that intensity is proportional to the excess carriers present in the system, Intensity vs time data may be readily converted into carrier population vs time. This provides carrier lifetime information for the system investigated.

In order to achieve this, a very short pulse of optical excitation is necessary. Then the system is monitored until it returns to equilibrium. In essence carriers are created in a time scale much shorter than the dynamic effects that are investigated and then the optical response of the system is recorded.

With the advance in ultrafast laser pulses and measuring electronics, it is easy to record intensity with a time accuracy better than a few psec. Typical carrier lifetime inside a semiconductor is in the

order of a nsec thus it is possible to follow the time evolution of this system.

Experimental setup

Two set of experiments were performed using this method. Initial experiments were performed in Technische Universitat Munchen at Munich, Germany. An ultra fast Ti:Sapphire laser was used to produce pulses with nominal width of 150fsec (pump pulses) at a repetition rate of 75MHz.

Samples were mounted inside a continuous flow liquid Helium cryostat in order to perform Temperature dependent studies. The pump laser was focused on the sample using a lens (F=150mm, D_{active}=10mm). The estimated spot size was in the order of 150μm diameter. Power impinging on the sample was selected in the range of 1-20mW which corresponds to a luminous intensity from 5.35W/cm^2 to 107W/cm^2. This translates to sheet carrier density in the $5\cdot10^{10}$cm^{-2} to 10^{11}cm^{-2} range that is quite high.

Photoluminescence from the sample was collected using a lens (F=50mm, D=12.5mm) and directed towards a monochromator. The grating used throughout the experiments was 150g/mm. The exit of the monochromator was coupled to a Multi Channel Plate (MCP) amplifier and finally to a streak camera. The entire setup was able to record time and spectrally resolved photoluminescence data.

Time range	*Time Resolution psec/pixel*	*Time window*
1	0.31	158 psec
2	1.52	800 psec
3	2.93	1.5 nsec
4	4.30	2.2 nsec

Table 4.5: TUM Streak Camera time resolution characteristics

The final experiments were performed at Dipartimento di Fisica and European Laboratory for Non-linear Spectroscopy (LENS), Universitá di Firenze, Florence Italy. The system used there is similar to the one used in Germany. A Ti:Sapphire laser was used with pulses <2psec and repetition rate of 76MHz. The pump focusing lens was F=7.5cm and D=0.5cm resulting in a similar spot diameter. Power varied from 100μW to 20mW resulting in a sheet carrier density in the $5\cdot10^{8}$cm^{-2} to 10^{11}/cm^{-2} range. The sample emission was recorded either using a photomultiplier tube and a car box analyzer setup (time integrated spectra and/or time resolved spectra at a specified wavelength) or alternatively the spectrometer emission could be directed to a Hamamatsu streak camera equipped with a CMOS sensor so that a two dimensional image spectrum/time could be recorded.

Time range	*Time Resolution psec/pixel*	*Time window*
1	0.26	150 psec
2	1.42	812 psec
3	2.44	1.4 nsec
4	3.6	2 nsec

Table 4.6: LENS Streak Camera time resolution characteristics

A typical image obtained using this setup is shown in Fig.4.7. The horizontal axis corresponds

to wavelength and the vertical axis to time.

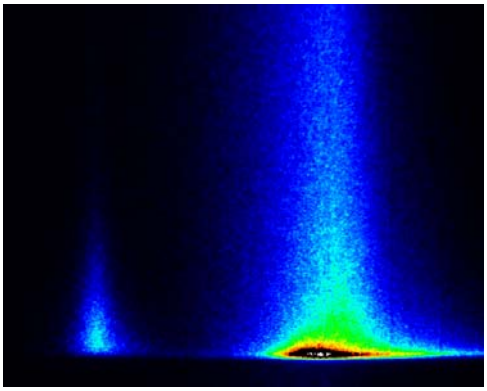

Figure 4.7.: Experimental data acquired using the time resolved streak camera setup. The horizontal axis corresponds to wavelength and the vertical one to time. The peak on the left is the emission of a $In_{0.2}Ga_{0.8}As$ quantum well and the peak on the right is from bulk GaAs. Intensity is displayed in color code.

Data analysis, which will be described in the following sections, provides information about the time evolution of the photoluminescence.

Data analysis

Assuming a gedanken three level system shown in Fig.4.8, we may model the time evolution of the intensity solving the differential set of equations:

$$\frac{dN_{pumped}}{dt} = A\cdot\delta(t-t_o) - \frac{N_{pumped}}{t_{th}} \tag{4.4}$$

$$\frac{dN_{thermalized}}{dt} = \frac{N_{pumped}}{t_{th}} - \frac{N_{thermalized}}{t_D} \tag{4.5}$$

Where the first equation describes the population evolution in the upper state and the second describes the middle state that is responsible for the luminescence. The δ function in Eq.4.4 is a Dirac – delta function describing the pump pulse impinging at time t_o on the sample. It is assumed that the excitation may only drive a small amount of carriers to the excited state. Thus, the ground state occupation probability is taken to be close to unity (weak excitation regime). Solving the system we finally obtain the following equation to describe the intensity with time:

$$Intensity(t) = I_o\cdot\frac{e^{\frac{t_o-t}{t_D}} - e^{\frac{t_o-t}{t_{th}}}\,UnitStep(t-t_o)}{-\left(\frac{t_{th}}{t_D}\right)^{\frac{t_D}{t_D-t_{th}}} + \frac{(t_{th})^{\frac{t_{th}}{t_D-t_{th}}}}{t_D}} \tag{4.6}$$

where t_o is the time at which the excitation pulse hits the sample, t_{th} is the thermalization time of the carriers inside the band which is usually very short and t_D is the carrier decay time.

Combining the time decay model described with the wavelength model described in PL data analysis, we obtain a model describing the PL both in wavelength as well as in time. This tool enables us to extract all the corresponding parameters from the time resolved photoluminescence experiments.

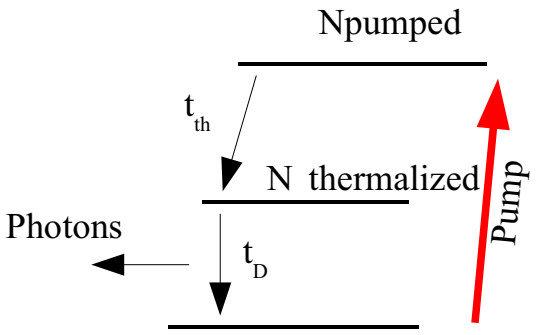

Figure 4.8: Three level system to model time evolution of the intensity in time resolved PL experiments

Time resolved emission from structures with built in electric field.

In case there is an electric field present inside the structure under investigation, emission becomes more complicated. The built-in electric field is partially screened by the carriers created from the excitation during photoluminescence. This translates to a dependence of the emission wavelength from carrier density and hence time, due to the Stark effect. The corresponding theory will be thoroughly described later but it is clear that a Stark shift term should be accounted for in the emission model described.

In our model we have incorporated an additional wavelength shift term of the form shifting λ_o with intensity i.e. carrier density.

$$\delta\lambda_o \equiv a \cdot \sqrt{I} \tag{4.7}$$

The factor α is merely a proportionality factor and depends on a number of structural parameters. Using this model we successfully modeled the time resolved data acquired throughout this project, extracting τ_D and α where applicable.

Temperature dependence of time resolved experiments

As described earlier, the intensity of the photoluminescence emission diminishes with increasing temperature because of non-radiative effects that play an important role at high temperatures. We may provide the intensity with temperature using the following equation:

$$I(T) = I_o \cdot n(T) \tag{4.8}$$

where I_o is the emission intensity should all carriers recombine radiatively and n is the efficiency of the emission which may be given by

$$n(T) = \frac{1/\tau_r}{1/\tau_D} = \frac{\tau_D}{\tau_r} \tag{4.9}$$

where τ_D is the decay time measured by the time resolved experiments and τ_r is the radiative lifetime of the system. Combining Eq.4.5 and 4.6 we have:

$$I(T) = I_o \cdot \frac{\tau_D(T)}{\tau_r(T)} \tag{4.10}$$

It is also known that τ_D is a combination of all decay paths in the system under study. Separating radiative and non-radiative decay paths, we may write:

$$\frac{1}{\tau_D}=\frac{1}{\tau_r}+\frac{1}{\tau_{nr}} \tag{4.11}$$

where τ_D is the decay time, τ_r the radiative lifetime and τ_{nr} the non-radiative lifetime. Combining the last two equations we may obtain:

$$\tau_{nr}=\frac{I_{max}/n_o\cdot\tau_D}{I_{max}/n_o-I_{PL}} \tag{4.12}$$

Thus assigning a low temperature efficiency n_o is enough to obtain both τ_r and τ_{nr} throughout the temperature range under study.

It is expected that τ_{nr} will decrease monotonically with temperature since non-radiative centers are more active at high temperature.

This analysis was initially published in [52] and is a powerful technique to obtain radiative lifetime measurements as well as an estimate of the non-radiative paths on a structure.

It is important to notice that in order for this analysis to hold, it is assumed that a steady number of carriers is pumped into the system throughout the temperature range studied. Of course, changing the temperature, also changes the bandgap due to thermal effects. Keeping the pump wavelength constant would result in different absorption at each temperature thus different pumping conditions across temperature. To cancel this effect, we followed the bandgap temperature shift with the pump beam wavelength.

Power dependence of time resolved experiments

Another significant issue when studying decay time in a semiconductor structure is to obtain power dependent measurements. Both PL intensity and decay time may provide useful information.

PL intensity should – to first approximation – be linear with power. Non-linearity in the low power regime indicates defects that trap carriers. Increasing the power quenches the defects and restores the linear behavior.

Although to first order approximation, decay time should be independent of power density it has been shown in [53] and [54] that higher power results to longer decay times since higher k states are occupied. These rates differ in the recombination dynamics among other things and carriers residing there have longer decay times.

Furthermore, in case of built-in electric fields, the electron hole overlap functions change with carrier screening leading to a change of dipole matrix element. This is directly connected to carrier lifetime. A piezoelectric quantum well for example would have a longer decay time when low carrier density is pumped into the system because of low electron hole wavefunction overlap. Increasing the pump power would result in screening of the electric field thus increasing the overlap. This manifests by a decrease in decay time at high excitation conditions contrary to a non piezoelectric system.

Finally, there are indications [55] that some non-radiative mechanisms may also be affected by

strain and piezoelectric effects.

An analytic description of the radiative and non radiative decay time with temperature, power or structure details, is complicated [56][57] to provide, since many mechanisms are important. However a qualitative description of the power dependence is indicative of the mechanisms involved in some systems.

Chapter 5.Laser Diode structures

This chapter presents a detailed overview of the structure design and fabrication. The laser diodes fabricated in this work are based on III-As. The first section presents the structure design whereas the second briefly presents the MBE fabrication.

Section:5.1.Laser diode design

As discussed previously, there are two main goals a laser structure has to achieve. The first is to efficiently produce gain and the second is to waveguide light in a cavity. Gain is realized using a semiconductor thin film (usually one or more quantum wells) whereas the waveguiding action is achieved by tailoring the refractive index of the structure along the growth axis. Although multiple quantum wells are used in most semiconductor lasers, the simplest case is when a single quantum well is employed to produce the necessary gain. In order to keep the parameters of the problem to a minimum, the single quantum well approach was adopted for this study.

5.1.1Single quantum well active medium

The material used to fabricate the active quantum well is directly related to the emission wavelength of the final device. $In_xGa_{1-x}As$ with x in the range of 0.15-0.20 emits near 980nm at room temperature which is a wavelength interesting for short range telecommunications. Furthermore this material may be pseudomophically grown on GaAs substrates. The later allows us to grow samples of this kind with the equipment available within the group. Given the above, this material was chosen to be used as the active quantum well throughout this study.

5.1.2 Waveguide design

Two waveguide designs were used in this project. Structure A, shown in Table 5.1, was inherited from a previous study of gain tunable laser diodes. [LeThomas].

Material	*Thickness*	*Doping*	*Description*
GaAs	150nm	P+ 10^{18} cm^{-3}	Ohmic contact
$Al_{0.3}Ga_{0.7}As$	1.6μm	P 10^{17} cm^{-3}	Cladding
$Al_{0.15}Ga_{0.85}As$	124nm	I	Top core
GaAs	20 nm		Top collection
$In_{0.1}Ga_{0.9}As$	12nm	I	Active
GaAs	4 nm		Bottom collection
$Al_{0.15}Ga_{0.85}As$	124nm	I	Bottom core
$Al_{0.3}Ga_{0.7}As$	2μm	N $3 \cdot 10^{17}$ cm^{-3}	Bottom Cladding
GaAs		N+ 10^{18} cm^{-3}	Substrate

Table 5.1: Laser diode structure A

Waveguide simulation based on numerical solution of the maxwell equations for a 1D waveguide (described in detail later) was used to obtain the waveguiding characteristics of the structure. The resulting waveguide mode is depicted in Fig.5.1 left.

The second waveguide structure is shown in Table 5.2. This structure was designed to reduce the lasing threshold of the final laser diode devices. There are a number of modifications compared to structure A. To begin with, the cladding layers were designed using $Al_{0.5}Ga_{0.5}As$ instead of $Al_{0.3}Ga_{0.7}As$. This results in a lower refractive index in the cladding leading to better confinement of the radiation within the core of the device. Furthermore, graded index layers were introduced around the core of the waveguide. This improves the radiation intensity at the vicinity of the active quantum well.

Material	*Thickness*	*Doping*	*Description*
GaAs	150 nm	P+ 10^{18} cm^{-3}	Ohmic contact
GaAs - $Al_{0.5}Ga_{0.5}As$	70 nm		-
$Al_{0.5}Ga_{0.5}As$	1.6 μm	P 10^{17} cm^{-3}	Cladding
$Al_{0.5}Ga_{0.5}As$ - $Al_{0.15}Ga_{0.85}As$	120nm	I	GRIN[ii]
$Al_{0.15}Ga_{0.85}As$	90 nm	I	Top core
GaAs	20 nm		Top collection
$In_{0.17}Ga_{0.83}As$	12 nm	I	Active
GaAs	8nm		Bottom collection
$Al_{0.15}Ga_{0.85}As$	110 nm	I	Bottom core
$Al_{0.15}Ga_{0.85}As$ - $Al_{0.5}Ga_{0.5}As$	120nm		GRIN
$Al_{0.5}Ga_{0.5}As$	2.5μm	N $3 \cdot 10^{17}$ cm^{-3}	Bottom Cladding
$Al_{0.5}Ga_{0.5}As$ - GaAs	70 nm		-
GaAs	-	N+ 10^{18} cm^{-3}	Substrate

Table 5.2: Laser diode structure B

The right-hand side of fig.5.1 shows the respective mode profile of structure B. It is clear that the mode is now better confined compared to structure A. Also an important difference arises in the maximum of the normalized mode. Structure B has a larger maximum at the center, which is expected due to the better electromagnetic confinement.

ii **Gr**aded **In**dex layer

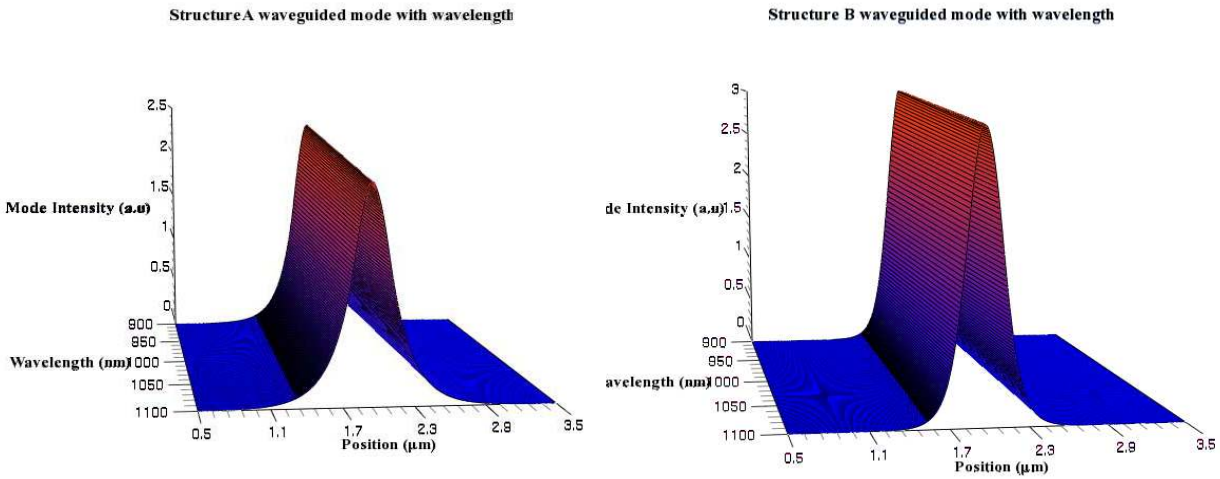

Figure 5.1: Waveguided mode at wavelengths between 900-1100nm for structure A (left) and structure B (right). Note that the latter structure provides a better confined mode with higher intensity near the center where the active quantum well resides. This translates to reduced threshold of operation for the laser devices based on the second structure.

Fig.5.2 provides a direct comparison of the performance of the two structures for the same wavelength. The cavity mode in structure B (depicted with green) is confined to the central part of the structure and the maximum (which coincides with the active quantum well) is much larger.

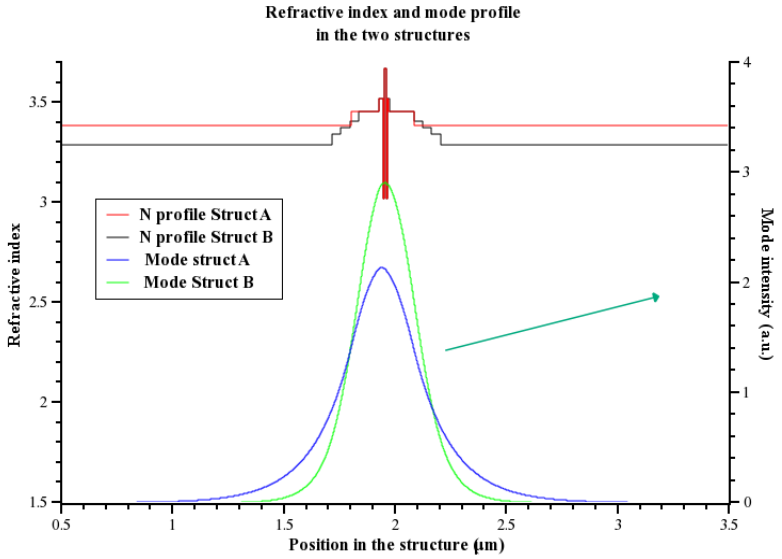

Figure 5.2: Comparison of the refractive index profile and the waveguided mode between the two structures for a wavelength of 980nm.

To clarify this further, the active quantum well confinement factor is shown in Fig.5.3. The higher the confinement factor, the lower the threshold of the laser device is expected to be. It is clear that structure B has improved the interaction of the cavity mode with the active quantum well

by as much 60%. Another important result is the wavelength sensitivity of the confinement factor.

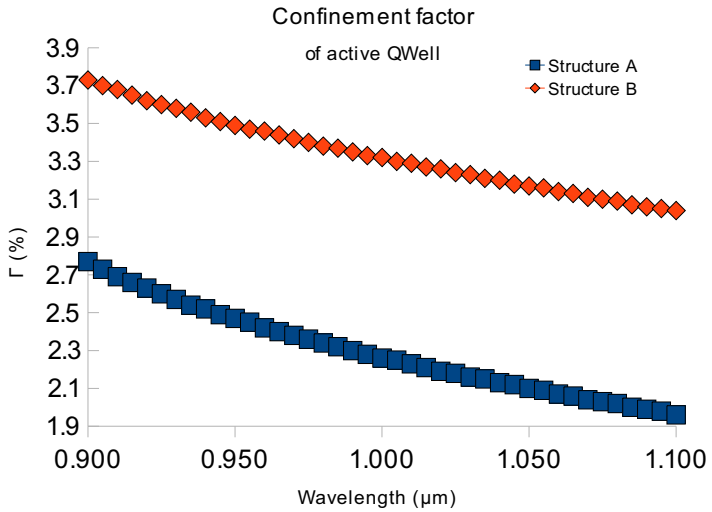

Figure 5.3: Confinement factor of the active quantum well versus wavelength for the two structures. Higher numbers are better since Γ is a direct measure of the percentage of the radiation in the waveguided mode that interacts with the active medium.

Since our laser devices are designed to be tunable, the same structure will be expected to operate in a range of wavelength. The less the dependence of the confinement factor on the wavelength, the better the waveguide will operate under tuning conditions. As may be seen from Fig.5.3 The confinement factor for Structure B has reduced wavelength dependence.

Finally it is necessary to compare the part of the radiation traveling in the doped region of the structure. This is because, doping and carriers provide enhanced light scattering mechanisms. The more the radiation interacting with this part of the structure, the larger the losses will be of the resulting device. The latter is inversely proportional to the threshold of the laser device as already described. In Fig.5.4 it is clear that for structure A a significant part of the cavity mode resides in the doped cladding layer. Whereas for structure B only a very small part of the cavity mode interacts with this part of the structure.

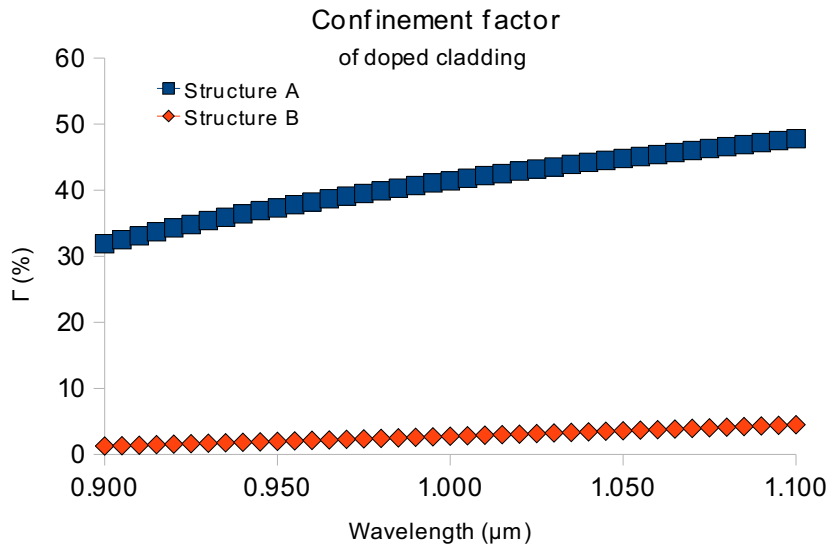

Figure 5.4: Cladding layers confinement factor for the two structures. Lower numbers are better since doped layers produce enhanced scattering effects.

Section:5.2.Molecular Beam Epitaxy (MBE) growth

One may be tempted to think that MBE is a black box, where you order whatever structure and it simply gets fabricated. The reality is far from this. Molecular beam epitaxy is a science in itself. It is often necessary to adapt to the inherent limitations of crystal growth in order to obtain the optimum result, than the other way around. It is therefore instructive to present a brief and by no means complete description of the typical problems associated with MBE growth.

Laser structures are complicated. It is not trivial to grow such a structure successfully. Each layer has to be grown at optimum conditions in order to obtain high quality, low dislocation density material. As an example, AlAs is grown at high temperature to increase the Al atyom diffusion on the surface during growth. This ensures a smooth growth surface. On the contrary, InAs is grown at low temperature since no In atoms are incorporated in the crystal otherwise. Furthermore, once an InAs or InGaAs surface is exposed to elevated temperature, it decomposes and In desorbs from the surface of the crystal. Following this reasoning, a change at the InGaAs substrate growth temperature will result in a change of the In mole fraction incorporated in the material.

Furthermore, each material is optimally grown at a different elemental-source flux. All these differences require continuous changes in the K-cell elemental source temperatures as well as the substrate temperature during growth. However, the abruptness of these changes is not obvious. Even if one requests an abrupt change in a K-cell temperature in the order of 100°C, the heat capacity of the material will limit the rate of temperature change. It is typical for a K-cell to require up to 2 min to stabilize at the requested temperature in a controlled manner. At a growth rate of 0.5μm/hr this translates to a growth thickness of 20nm which is comparable to the thickness of some of the layers in the structure.

Therefore, there are two technical issues related to the previous discussion. The first is how to

abruptly change the temperature (i.e. the fluxes) of the K-cells. The second one is how to abruptly change the substrate temperature.

As far as the sources are concerned, the optimum solution would be to utilize more than one K-cell for each kind of element. If for example two Ga sources were available, then it would be easy to use the first source to grow the initial layer and as soon as a change in flux is needed, switch to the second source which is in advance adjusted to the right temperature (flux). Of course, this requires redundant K-cell sources. In our MBE system no redundant sources are available.

Anyhow, the extra K-cells would not resolve the substrate temperature issue. A different approach employed in our system, is to interrupt the crystal growth. If all group III material fluxes towards the substrate are blocked, no growth is obtained. The necessary time is spent in this state to reset all temperatures at the desired values. Then the fluxes are restored in order to continue growth with a different layer. As expected there is a price to pay for this interruption.

Even under optimum conditions, there are still some contaminants in a MBE chamber. These result in a low, yet measurable, defect density in the grown crystal. Should the growth be interrupted, these contaminants are accumulated on the surface of the wafer. In a sense, a delta layer of contaminants is formed precisely at the position that the interruption occurred. Depending on the position inside the structure that a growth interruption occured, this may or may not have a serious effect. If for example this layer of increased defects is placed inside a quantum well that is designed to emit photons (the active well in a laser diode structure) the non-radiative centers created by these defects race against radiative recombination, “killing” electron hole pairs, thus reducing the efficiency of the device.

5.2.1 Optimum growth temperature

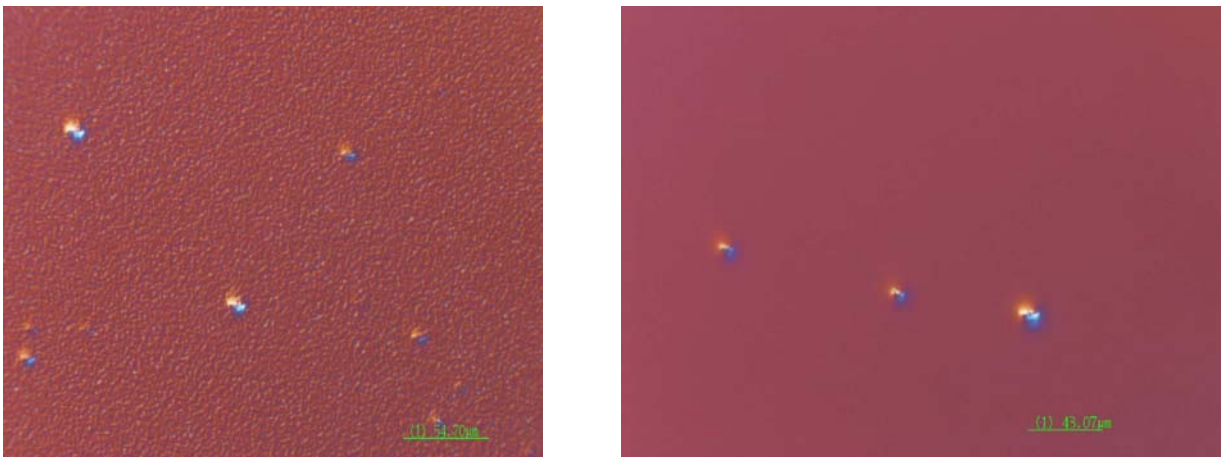

Figure 5.5: Surface roughness observed with optical phase shift microscope. Sample on the right was grown at sub-optimal $Al_{0.5}Ga_{0.5}As$ temperature. As a result surface roughness occurred. The same structure grown at optimum substrate temperature is shown on the right. Roughness is efficiently supressed. The elongated spots are oval defects typical in GaAs growth.

Optimum growth temperature was investigated for each material separately. Surface investigation (roughness and defect density) and photoluminescence (PL) were used to determine

the quality of the grown layer. The figure of merit was the intensity of the PL and the FWHM of the quantum well emission at low temperature. In Fig.5.5 (left) a characteristic example of sub-optimum substrate temperature during the $Al_{0.5}Ga_{0.5}As$ layer is depicted.

The surface roughness resulting from reduced surface mobility of the Ga and Al atoms during

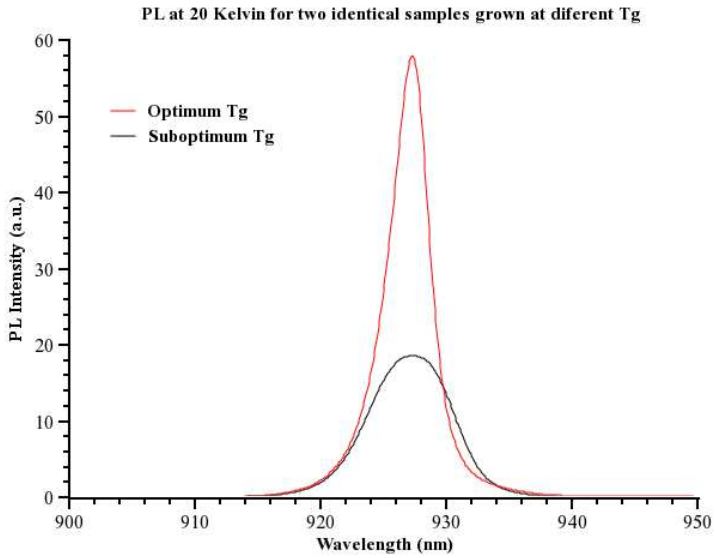

Figure 5.6: Comparison of the $In_{0.17}Ga_{0.83}As$ QW photoluminescence from the two samples shown in Fig.5.5. The FWHM for the optimum sample is 3.3nm whereas the FWHM for the rough sample is 6.5nm. Furthermore, the emission intensity is adversely affected.

growth has a direct effect on the emission of the quantum well. Fig.5.6 depicts the corresponding PL emission data. Not only the FWHM of the emission from the quantum well (QW) is increased by a factor of approximately 2 but the PL intensity also reduces. Both have a direct impact on the performance of laser devices.

5.2.2 Transient suppression

Another issue that was addressed was transient effects in K-cell temperature. As discussed, even if an abrupt temperature change is performed in a source, it will take a certain amount of time for the K-cell to reach thermodynamic equilibrium in the new temperature setting. Attempt to grow a semiconductor layer prior to this equilibrium being established, will result to growth with the elemental flux changing over time. In case of alloy growth, this may lead to non-uniform material mole fraction in the given layer. In Fig.5.7 an abrupt temperature drop was performed in the Ga K-cell and an $In_{0.17}Ga_{0.83}As$ QW was grown before the Ga K-cell temperature (T_{ga}) was stabilized. As a result, a non uniform In mole fraction quantum well was grown. This is clear by the multi-peak features existing in the low temperature PL signature of the QW.

In order to avoid this issue, special care was taken to allow enough time for the cell temperature to stabilize prior to growing ternary compound layers.

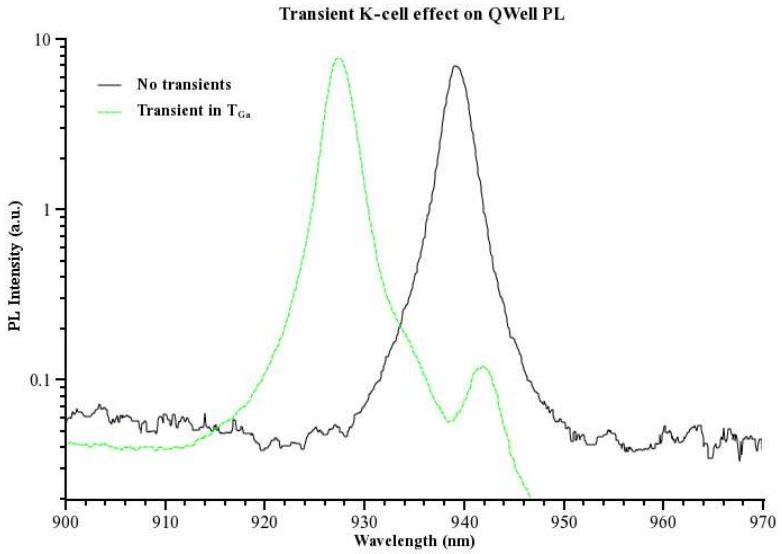

Figure 5.7: Effect of stabilizing the Ga K-cell temperature on the growth of $In_{0.17}Ga_{0.83}As$ QW's In the case of transient flux growth, a non-uniform QW is obtained as manifested by the multiple PL peaks. In the other case, the emission is a single peak.

5.2.3 Tunable structure growth

In the tunable structure which will be discussed in the final chapter of this thesis, the $In_{0.17}Ga_{0.83}As$ quantum well, is sandwiched by a high bandgap $Al_xGa_{1-x}As$ tunneling barrier. Here the growth optimization of these structures is presented. Nominally, the AlGaAs material is grown at much higher temperature compared to InGaAs. In fact the larger the Al mole fraction the higher the optimum substrate temperature, reaching more than 200°C difference for the case where AlAs barriers are used. The implication in the structures designed for this work is that at least two growth stops have to be implemented at the edges of the InGaAs QW.

Material	*Thickness*	*Doping*	*Description*
GaAs	150 nm	P+ 10^{18} cm^{-3}	Ohmic contact
GaAs - $Al_{0.5}Ga_{0.5}As$	70 nm	P+ 10^{18} cm^{-3}	-
$Al_{0.5}Ga_{0.5}As$	1.6 μm	P 10^{17} cm^{-3}	Cladding
$Al_{0.5}Ga_{0.5}As$ - $Al_{0.15}Ga_{0.85}As$	120nm	I	GRIN
$Al_{0.15}Ga_{0.85}As$	90 nm	I	Top core
GaAs	20 nm	I	Top collection
$Al_{0.6}Ga_{0.4}As$	5 nm	I	h-tunneling barrier
$In_{0.17}Ga_{0.83}As$	12 nm	I	Active
$Al_{0.6}Ga_{0.4}As$	6 nm	I	e-tunneling barrier
GaAs	8nm	I	Bottom collection
$Al_{0.15}Ga_{0.85}As$	110 nm	I	Bottom core
$Al_{0.15}Ga_{0.85}As$ - $Al_{0.5}Ga_{0.5}As$	120nm	I	GRIN
$Al_{0.5}Ga_{0.5}As$	2.5μm	N $3 \cdot 10^{17}$ cm^{-3}	Bottom Cladding
$Al_{0.5}Ga_{0.5}As$ - GaAs	70 nm	N+ 10^{18} cm^{-3}	-
GaAs	-	N+ 10^{18} cm^{-3}	Substrate

Table 5.3: Tunable laser diode structure. The two layers marked with red are the tunneling barriers.

As already discussed, growth stop is a risky choice when active layers are involved (such as a QW emitting photons). The alternative is to grow the AlGaAs barriers at a sub-optimum temperature. Given the fact that the layers are only a few nm thick, roughness is not expected to be an issue. As will be discussed when presenting the performance of tunable diode lasers, both alternatives were investigated.

Part II: Laser device fabrication and characterization

Chapter 6.Laser diode processing

This chapter presents a detailed overview of the fabrication methods used to create edge emitting laser diodes from III-As based material. In the first section, a brief presentation of the processing methods is presented. In the second section, the fabrication sequence flow is discussed. The third and final section presents the fabrication optimization.

Section:6.1.III-As semiconductor processing

By the description "processing", we refer to the procedure that transforms a crystalline material, like GaAs, into functional devices. By definition, processing is sequential. Every process is performed on the entire wafer, layer by layer. Each layer is a building block of the final topography. Each time a processing step is performed, some means to define the device geometry is needed. Thus each step involves some means of patterning the substrate surface. Given this, the fundamental process involved in even the simplest fabrication process is patterning.

6.1.1 Lithography

In order to etch material, deposit metal or perform any manipulation onto a wafer, a way to define shapes – act on desired parts of the wafer's surface – is needed. Technology provided us with chemicals that react to light or electrons, much like a photographic emulsion. Depending on the radiation used to define a pattern (UV, Deep-UV or e^-) a proper thin film of material, sensitive to the corresponding radiation, is deposited on the sample. Usually spin coating is used i.e. the radiation sensitive resin is dispensed on the wafer and subsequently the sample is spinned at 2-5krpm to produce a thin homogeneous film. Solvents are evaporated using baking to produce a thin, hard film of radiation sensitive resin.

In our group a Karl-Suss MA6 UV lithography system is used. It is equipped with two sources both in the UV region (350nm or 240nm). The first one is used routinely and can produce patterns with minimum feature size down to 0.4μm. Minimum feature size is directly related to radiation wavelength through the Rayleigh law. When features as small as 0.2μm are necessary, the 240nm light source may be used. Smaller patterns require focused electron beam or other advanced techniques[iii]. The effective De Broglie wavelength of an electron accelerated to a few KeV is so

iii Currently "Double exposure lithography" is being used to produce patterns down to 90nm using DUV (240nm) or XUV(190nm).

small that it is easy to focus the e-beam to spots as small as a few nanometers. Thus very small geometries may be defined.

Back to optical lithography, the prototype of the pattern is engraved on a thin metallic film (mask) supported by some transparent material (Quartz or Borosilicate) defining transparent and opaque areas. This "mask" is placed facing the sample to be processed. A well defined light dose (intensity·time) is passed through the mask. Areas that are transparent on the mask allow light to impinge on the sample. This causes chemical reaction on the photosensitive emulsion. A proper chemical solution (i.e. developer) is used to selectively remove the exposed (positive resist) or unexposed (negative resist) areas. Thus the pattern is transferred onto the sample. The first row in Fig.6.1 depicts the described process.

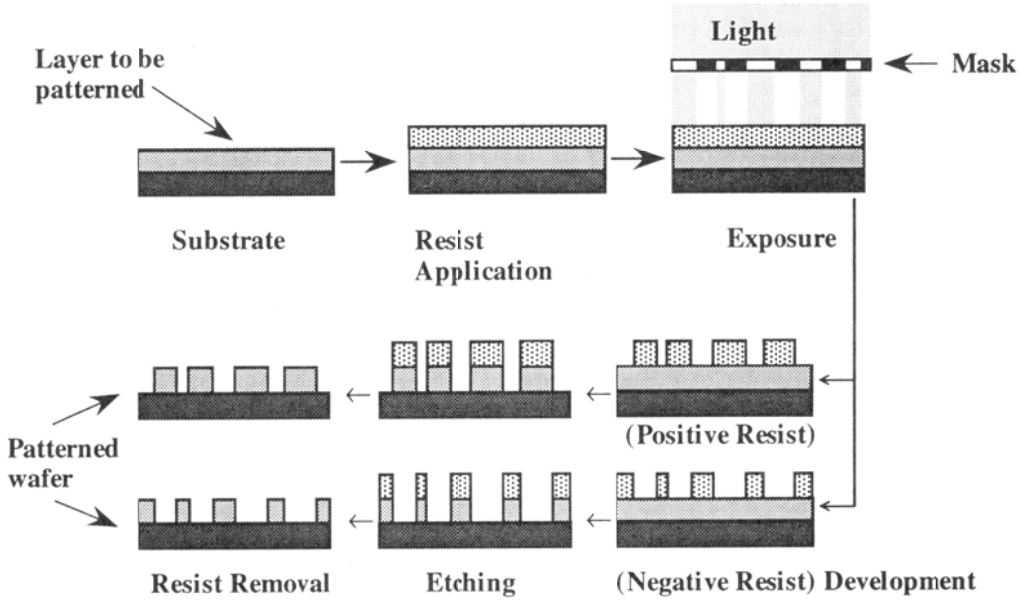

Figure 6.1: Lithography concept, applied in an etching step.

Optical-lithography is faster (the entire sample is patterned in one exposure) and cheaper than any other patterning solutions. This is why photo-lithography is the preferred method. E-beam is only used when no alternative exists. Techniques to extend the resolution of optical lithography beyond the diffraction limit are actively explored. Double optical exposure and immerse photo-lithography are some of the most promising techniques explored by major fabrication companies.

6.1.2 Contact formation

Ohmic contacts on GaAs is a mature technology. Electron-gun (e-gun) evaporation (Temescal SIMBA e-gun evaporator) was used to deposit metals. Metal patterning was achieved employing the lift-off technique [58].

P-type ohmic contact on GaAs

P-type ohmic contacts consist of a Pt/Ti alloy. The following metalic multilayer is deposited on p+ GaAs: 4x (50Å Pt followed by 100Å Ti) then 400Å Pt and finally a conduction layer of 1000Å

Au.

The Pt/Ti multilayer is the core of the contact. Pt/Ti diffuses into the p+ material making a shallow degenerate layer. The top Au layer ensures an adequate current carrying capacity of the metal film. Since Au is highly diffusive, a thick Pt layer is used to inhibit Au migration towards the contact.

Contact activation is achieved by sample **rapid thermal annealing** (RTA) at 410°C for 60sec.

N-type ohmic contact on GaAs

N type ohmic contacts follow the same reasoning. A Au/Ge multilayer is used. Specifically 3x (100Å Au followed by 200Å Ge) then 400Å of Ni and finally 1000Å of Au. The Au/Ge multilayer forms a eutectic melting at 350°C that diffuses into the GaAs, forming a degenerate n++ layer. Ni much like Pt in the p-type contact is a rigid metal inhibiting Au diffusion. Finally Au is deposited to reduce the total contact resistance.

Contact activation is achieved by RTA at 410°C for 20sec. A comparison of RTA for p and n type ohmic contacts is interesting. Annealing temperature is the same. This is explained by the fact that GaAs decomposes at higher temperatures than 410°C. Decomposition would lead to Arsenic loss on the surface. Arsenic vacancies act as mid-gap states [59], causing the ohmic behavior to deteriorate. Comparing RTA duration, a large difference is observed. This may be explained by taking into account the fact that Ti and Pt exhibit a small diffusion coefficient whereas Au and Ge are quite diffusive. The conclusion drawn from this discussion is that p-type ohmic contact RTA has to be performed before any n-type contact is deposited on the sample.

6.1.3 Material Etching

Compound semiconductor device isolation is obtained by removing excess material. This is mainly due to the fact that implantation – which is extensively used in Si fabrication – has poor results in compound semiconductors. Material etching is achieved by chemically attacking the crystal either with proper chemical solutions (**wet etching**), or by **plasma** (**dry etching**).

Wet etching

Several aqueous solutions of acid/hydrogen peroxide etch III-As compounds. Each solution has a distinct advantage. Important parameters are etch rate, etched surface quality and material selectivity. Table 6.1 presents some of the most common etchants used in III-As wet etching.

Composition	*Etch rate*	*Selectivity*	*Roughness*
$1:H_3PO_4/1:H_2O_2/40:\ H_2O$	1000Å/min	Crystallographic	small
$1:H_3PO_4/1:H_2SO_4/1:H_2O_2/10:\ H_2O$	2.5μm/min	Crystallographic	small
$1:H_2SO_4/1:H_2O_2/100:\ H_2O$	0.5μm/min	Isotropic	None
Citric Acid	0.1μm/min	Stops at AlGaAs	no info

Table 6.1: Typical wet etching solutions used in GaAs based device processing.

All wet etching reactions remove material by oxidizing the surface atoms and subsequently removing the resulting oxide. That is why an oxidizing agent (hydrogen peroxide) and an oxide etching agent (acid) is used. Wet etching attacks only the surface of the material. Thus no damage

to the remaining crystal is induced. This is especially true for etchants that produce a smooth surface.

On the other hand, wet etching has certain limitations. In general, etching attacks all exposed surfaces, thus etching does not progress only downwards but also sidewards. This is described as **isotropic etching**. Some chemicals provide a crystal structure sensitivity, etching faster along a certain crystallographic orientation (**preferential etching**). This prevents realization of trenches with large **aspect ratio** (depth/width) or vertical sidewalls. A different approach to material etching is necessary to realize such topologies where size does matter.

Dry etching

In principle, removing an atom from any material requires enough energy to break the chemical bonds that keep it in place. In an etching solution this energy comes from the bond energy of the reactive agent. However, other alternatives exist.

A free atom that is accelerated has kinetic energy which may be readily calculated. If such an atom, impinges on a crystal, the kinetic energy is transfered upon collision to the bonds holding the crystal together. If enough kinetic energy is supplied, a portion of the crystal (an atom or a cluster of atoms) may be extracted. Using inert accelerated atoms, such as Argon, and bombarding the surface of a semiconductor crystal will gradually etch away a portion of the material. The process described is called **ion milling** and is purely physical.

Using an atom that may chemically react with the crystal, forming a new molecule, will add the formation energy of the new molecule to the energy balance. Chlorine atoms, which readily react with Ga to form $GaCl_x$ molecules are a good example. In fact a Cl atom may need no kinetic energy at all to extract a Ga atom from a GaAs lattice, given the fact that GaCl formation is energetically favorable. Furthermore, contrary to ion milling, the product of this reaction is volatile and will thus fly away from the reaction site.

Given the above, if the semiconductor surface is exposed to a plasma environment, etching is possible provided the correct parameters (atom kinetic energy, atom spieces) are selected.

In a **Reactive Ion etching** (RIE) apparatus, plasma is created using an RF field. Selecting the gas used in the RIE chamber, will provide the corresponding atoms, gas pressure affects the density and the mean free path of the atoms and finally RF power affects the kinetic energy and the relative density of the various spieces produced. Successful dry etching is all about choosing the correct gas, one that provides active species that will etch the material, as well as parameters like kinetic energy (i.e. plasma power), pressure e.t.c. In this work, all dry etching was performed in a Vacutec Reactive Ion Etching apparatus equipped with several etching gases, detailed in table 6.2.

Gas	*Typical application*	*Selectivity*
Cl_2	III-As, III-N	None
BCl_3	III-As, III-N	None
CF_4	GaAs / Oxides	Strong to Al containing layers
SF_6	GaAs / Si-C	Strong to Al containing layers
CH_4	III-N etching	-
H_2	III-N etching	-
O_2	polymer etching	-
Ar	Ion Milling	None

Table 6.2: Available gas species for dry etching along with their typical application.

The main drawback of dry etching techniques is material damage. Unless special care is taken, impinging atoms destroy the crystal below the surface. A layer of damaged material may remain below the etched surface after dry etching. This is unacceptable for laser diodes since defects are non-radiative recombination paths that reduce the laser efficiency.

Another issue is etched surface roughness. At the sidewall of a laser device, roughness acts as a scattering center for electromagnetic radiation, removing photons from the cavity mode. This has a direct impact on laser performance in terms of threshold.

To fabricate an efficient laser device, it is necessary to obtain etching with damage free, smooth sidewalls. The way to achieve this will be discussed when presenting optimization of the etching process used in fabrication of the devices for this work.

6.1.4 Dielectric deposition

In several cases it is necessary to cover parts of the device with a non-conducting and/or transparent material. There are several dielectrics available such as Oxides, Nitrides and polymeric substances (plastics). Specifically in edge emitting laser diodes, the need for a dielectric coating is three-fold.

Each device will finally be interconnected to macroscopic size electrodes so that the device may be operated. Thus there is a need to create large metallic contacts on the device. These are typically created on the side of the device away from the active layers. The need to provide isolation between the interconnect metal and the rest of the semiconductor is obvious.

Furthermore, surface states of the semiconductor have to be minimized. A free semiconductor surface is full of defects, originating from the lack of periodicity. Covering the surface with a dielectric improves the situation and reduces surface defect density [60].

Finally, as already discussed, some degree of roughness is inevitable on the etched surface of a semiconductor. The resulting optical scattering is related to the refractive index contrast of the materials forming the rough interface. Si_3N_4 has a refractive index of 2.3 which is much closer to the refractive index that GaAs has (3.5). Thus, covering the sidewalls of a laser diode with Si_3N_4 is expected to reduce light scattering as well. Si_3N_4 is grown using **Plasma Enhanced Chemical Vapor Deposition** (PECVD).

Overall Si_3N_4 is known for its excellent dielectric characteristics, high refractive index, low absorption in the visible and IR and very good passivation effect on GaAs.

PECVD Si_3N_4 deposition technique

In order to create Si_3N_4 several techniques are used. In III-V fabrication the most common one is **plasma enhanced chemical vapor deposition** (PE-CVD).

In a PE-CVD, gas precursors are used to provide Silicon and Nitrogen atoms. SiH_4 is used to provide Si and N_2 or NH_3 to provide Nitrogen. These molecules are dissociated in a plasma environment (plasma enhanced) and the sample is heated to promote growth of the material. PECVD is in fact the exact opposite of RIE, free atoms are created and the minimum kinetic energy possible is provided. Since bonded atoms have less energy, it is energetically favorable for these atoms to form a Si_3N_4 film rather than remain in the gas phase.

Hydrogen is the main issue associated with PECVD growth of Si_3N_4. PECVD grown Si_3N_4 films suffer from high hydrogen content originating from SiH_4 and NH_3 [61].

6.1.5 Interconnect metalization

Semiconductor devices need electrical interconnection to the macroscopic world. To obtain a firm, manageable area of electrode there is a need to create interconnect pads on the semiconductor surface. Each pad is then connected to the proper terminal of the device through a metalization. Interconnect metalization is one of the final steps in the fabrication of nearly any semiconductor circuit. It should successfully carry current in and out of the device, and manage to connect parts of the device which may be on different height (remember that compound semiconductor circuits are seldom planar). Thus a thick metal, with low resistance is necessary. Furthermore this metalization should adhere firmly on the underlaying layers. This ensures that probing the device from the outside (either with probe-tips or with bonding wires) will not result to metal damage.

6.1.6 Chemical – mechanical Polishing (CMP) - Lapping

As discussed in laser diode theory, current density in the order of KA/cm^2 is routinely applied on a semiconductor laser diode. Even though a significant part of the input power is turned into light, heating is a major issue in laser diodes. Cooling the device through a 200-300μm thick GaAs substrate is inefficient. Furthermore, cleaving a thick substrate is more error prone. It is thus preferable to thin down the substrate, making both cleaving as well as cooling easier. chemical mechanical polishing (CMP) is used to grind the substrate down to 100μm.

An abrasive material (Al_2O_3 grains), dissolved in H_2O is used. The surface of the material is scrubbed against a rotating disk covered with the abrasion solution. The thickness changes are monitored with a micrometer. This process is called **lapping**.

Chemo–mechanical polishing (CMP) is subsequently used to restore surface roughness. CMP is a combination of etching chemicals (Cl containing) and fine Al_2O_3 grains that is applied on a rubber abrasive disk. Much like lapping, only more gentle, the process removes material turning the

semiconductor into a flat, mirror like surface.

In total the process followed is described below in bullets:

- Measure initial thickness – calculate thickness to be etched.
- Mount sample on carrier (round glass 4") using wax.
- Install metal abrasive disk and Al_2O_3 20μm grains etching solution.
- Etch until final thickness is reached (35rpm on the disk).
- Thoroughly clean the carrier with the sample to remove large abrasive grains.
- Install rubber foam CMP disk and soak with CHEMLOX© and water.
- Polish sample for 5 min at full rotation speed.
- Rinse thoroughly using Di-H_2O.
- Heat to 60-70ºC to melt wax and remove from carrier.
- Rinse in Trichloroethane to dissolve wax and then degrease[iv].

As soon as this is completed the sample should have a smooth back surface and a thickness of approximately 100μm.

6.1.7 Cleaving – facet formation

As discussed earlier, cleaving is used to form laser diode mirrors. The process involves controlled fracture of the crystal along a crystallographic orientation with low bond density. The process is schematically outlined in Fig.6.2. Mirrors were not coated resulting in an effective mirror reflectivity of ~32%.

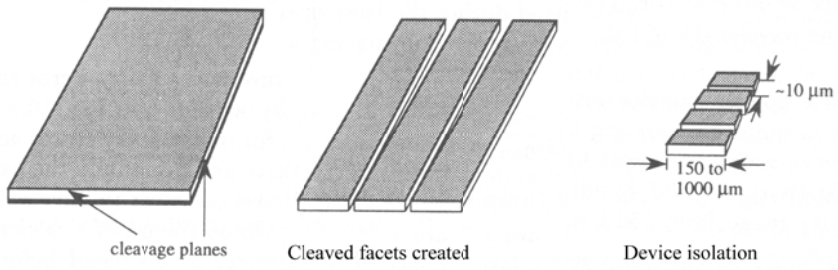

Figure 6.2: Cleaving process schematically illustrated

6.1.8 Device mounting – heat dissipation

As pointed out already, heat dissipation is a significant issue in laser diode operation. In fact heat sinking in laser devices is considered an area of active research [62]. If continuous operation is not necessary and short operation pulses are used, the device does not heat extensively. This regime of operation is called pulsed operation and is routinely used to characterize laser devices.

Devices throughout this project were mounted on gold coated ceramic tiles. Mounting was achieved using In. The resulting thin In layer also ensured proper electrical contact to the bottom n-

iv Degreasing a sample is achieved by submerging it to strong solvents (Usually acetone, propanol and water). This removes organic residues (grease) from the surface.

type contact.

Subsequently tiles were mounted on packages. Wire bonding was used to connect each laser device to a package connection. This way, several devices can be simultaneously mounted. A common ground is used for all devices (n-type contact) whereas each p-electrode is connected to a single port forming an independently addressable array of laser diodes.

Section:6.2.Edge emitting laser diode process

The main processing techniques in semiconductor fabrication, have been described in the previous section. Here the step combination required to transform a laser diode structure into an edge emitting laser diode is described. When processing semiconductors, it is important to have an overview of the process flow. Each step may need further optimizations taking into account preceding and subsequent processes.

6.2.1Process flow

The process flow that was initially implemented to fabricate cleaved laser diodes is outlined in the following bullets.

- **P-type ohmic contacts:** P-type ohmic contacts are evaporated on the material as described in the previous section. Lift-off is used to obtain continuous metal stripes of varying width (see mask design). P-contacts are annealed to obtain a low specific contact resistivity. P-type metalization is used to align all subsequent steps.
- **MESA formation:** Reactive Ion Etching (RIE) and a mix of Cl_2 and BCl_3 is used to etch the material and form ridges with 10-50μm width 1mm apart from each other. On top of the ridge, lies the p-type contact. The etch depth is 1.7-1.8μm so as to achieve electrical isolation of the devices.
- **Si_3N_4 deposition:** Plasma Enhanced Chemical Vapor Deposition (PECVD) is used to cover the entire surface with 0.3μm thick Si_3N_4. The side walls of the ridge are also covered using this method. It is reported in the literature [63] that Si_3N_4 deposited using this method has a high molecular H_2 content.
- **Si_3N_4 patterning:** RIE is used (CF_4/O_2) to etch away the Si_3N_4 directly over the p-type contacts. This is necessary to interconnect the p-contact to the interconnect metalization.
- **Interconnect metalization:** Subsequently the interconnect metal is evaporated on top of the dielectric, forming a dielectric bridge. The interconnect metal also forms a continuous pad 200μm wide on one side of the ridge allowing for easy electrical contact to the device.
- **Lapping**: The sample is thinned down to 100μm thickness to improve cooling and cleaving as discussed in the previous section. During this step the front side of the sample is coated with thick resist to protect the devices from scratching.
- **N-type contact**: The n-type contact is deposited on the backside of the sample. This makes fabrication easier plus improves the series resistance of the total device providing a large area contact. Annealing of the contact completes the fabrication of the sample.
- **Cleaving**: Finally cleaving forms the devices of the desired length. Typical cavity length ranges from 500μm to 2mm. Shorter cavities are difficult to cleave whereas longer cavities

require excessive current to operate.

6.2.2 Lithography mask design – cleaved laser diodes

In order to complete the steps described previously, it is necessary to design a set of masks. This mask set, enables us to fabricate edge emitting, heterostructure cleaved laser diodes of arbitrary length, with contacts either on top or top/bottom configuration. Ridge width should be varying in order to be able to study the effect of width on laser performance.

Mask design rules

In order to be able to design a mask that can be successfully used, several design rules have to be applied. The most important sources of design rule needs are described thereafter.

a) Optical lithography misalignment

Consecutive steps involve alignment of subsequent steps on pre-existing patterns. Using the available equipment (MA-6 UV optical lithography) the expected misalignment is <0.4μm. This number is provided by the manufacturer of the equipment and regularly checked in our process to ensure that no malfunction is present.

b) Resist fidelity

The dimension of the transferred pattern on the resist may differ from the mask pattern, depending on the optical lithography quality. For example a strong overexposure would result in reduced size in the shape of the remaining resist (Positive resist). The same effect goes for over-development. Even if the optimum parameters are selected, the resist itself has a resolution which may not be surpassed. For AZ-5214 which is the resist used in our group, this is designated to be 0.1μm.

c) Ohmic contact

Contact metalization expands during annealing. This is inevitable due to diffusion of the metal edge. When designing a device this has to be taken into account. Depending on the annealing and the metalization, the degree of expansion may differ. A safe upper margin is 1μm.

d) Ridge formation

Depending on the etching technique used (wet or dry) there is always some undercut of the ridge dimension. Side wall etching is inevitable to some extend. It is obvious that wet etching, produces the most undercut, in fact similar to the etch depth (d_{etch}). Therefore in that case the design should be larger by d_{etch}. In case of isotropic dry etching the situation is similar. However in non-isotropic dry etching, the effect may be insignificant. Especially for dry etching processes that produce smooth and vertical walls like the one used in this work, the undercut is minimal and may be neglected.

Taking into account the described parameters, and using experience to determine their importance during the process the following design rules have been applied:

1. **P-contact to ridge** clearance has to be at least 1μm. Notice that if p-contacts were evaporated and annealed after the ridge, this should be increased to take into account misalignment and edge effects on spin coated photoresist.

2. **Ridge** is designed at the nominal width since dry etching is to be used.
3. **Dielectric opening to contact size** edge has to differ by at least 1μm. In order to make sure that the interconnect metal comes in contact only with dielectric and contact metal.
4. **Top n-contact to ridge** clearance has to be at least 5μm. N-contact lithography is performed after the ridge is formed. The 2μm thick step on the side of the ridge causes significant variation of the resist thickness close to the ridge. Placing the n-contact closer would create non-unifomity in lithography definition of the n-contact.
5. **Contact pad** size has to be at least 150μm wide in order to facilitate bonding. 200μm was chosen to allow easy bonding.

Finally, a set of 4 mask plates were designed using the described guidelines. These mask plates enable fabrication of arbitrary length edge emitting laser diodes. Several ridge width are included in the design. Namely, 10,20,30,40 and 50μm wide laser bars are designed. The diodes were designed to be 0.5mm apart and individually addressable.

Section:6.3.Process optimizations

Laser diode fabrication requires tedious optimization. LD's are complex devices and both electronic as well as optical aspects have to be carefully reviewed. Optimizing fabrication is expected to improve lasing operation threshold current and temperature sensitivity.

6.3.1 Ohmic contact optimization

Ohmic contact for GaAs devices are long used in our lab. Initial experiments revealed two main areas of possible improvement.

Roughness

Initial experiments revealed that roughness existed both on the metal surface as well as the edge of the metalization. The main reason for surface roughness was identified to be carbon contamination in the Au crucible (container) of the evaporator.

Crucible made from carbon were used to evaporate Au. Given time, carbon build up on the surface of the Au target, resulted in small clusters of Au being evaporated from the source onto the samples. Two ways to remedy the situation were found:

1. Use Mo crucible. Molybdenum is a high temperature melting material and does not produce the same effect. In fact Au evaporations done using this crucible produced a very smooth surface. There was a severe problem however concerning longevity of the crucible itself from thermal cycling. Cracks would appear after some time and Au leak occurred through the cracks.
2. Regular cleaning of Au target. It was found that carbon build up occurred in the form of dust on the surface of the Au target only. This was readily removed with a clean-room compatible cotton-cloth. Regular cleaning of the target reduced the cluster formation to an acceptable level.

Edge roughness issues were attributed to bad photoresist side wall quality. In lift-off, a negative

photoresist side wall is significant. A negative resist sidewall creates shadowing of the deposited metal allowing easy removal of the unwanted material. Chlorobenzene was used to improve the side wall properties of the lithography [64]. Metal edge definition was successfully improved using this technique.

Thickness

Normally both type of contacts require a thick Au overlay (2000Å). However in the specific application, both contact are not required to laterally convey current. This function is performed by the interconnect metal which covers the p-type contact, and the large area In bonding at the bottom which dissipates current into the entire bottom surface of the sample. This is why the initial Au layer thickness was reduced to 1000Å. The advantage of this decision was that better lift-off quality was achieved for the p-contact (thin layers are easier to lift-off properly) as well the ridge sidewall lithography.

6.3.2 Ridge etching

Initially, ridge formation was done using wet etching $H_2SO_4/H_2O_2/H_2O$ solution. Fig.6.3, depicts the etch profile of an early device. Strong waveguiding was achieved by removing the semiconductor waveguide core material. The etching depth was 2.8μm.

As discussed earlier, strong waveguiding exposes a large part of the laser radiation. This increases the scattering losses of the device. Instead, adequate waveguiding effect may be accomplished by etching only part of the top cladding layer (effective index guiding). This minimizes scattering of the cavity mode thus reducing losses.

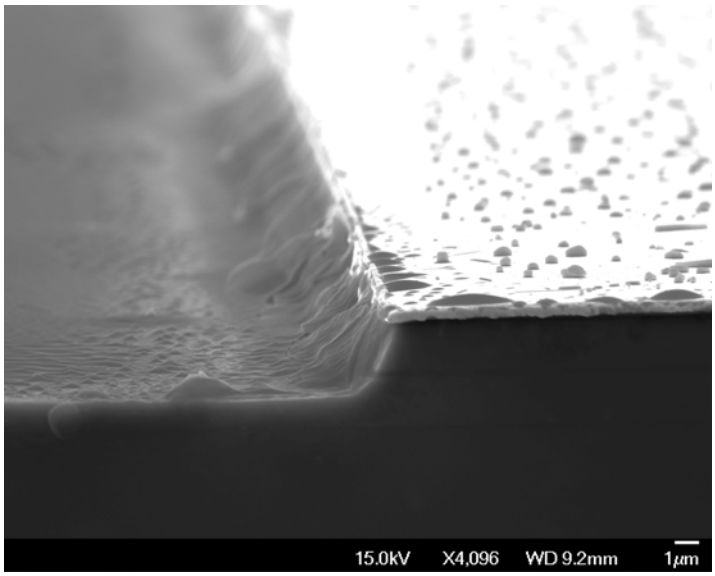

Figure 6.3.: SEM image of the side wall roughness of initial wet etching Ridge formation. The active region may be barely seen at the middle of the ridge as a dark line.

Ridge etching is also used to ensure electrical isolation. A very shallow ridge, one that does not remove the top conductive layers, will result in significant current spreading. This is undesirable since it will reduce the effective current density on the device.

For the reasons described so far, etch depth was decreased to 1.8μm, barely enough to etch the top cladding layer and reach the non-conducting layers.

Fig.6.4 Depicts the sidewall profile of a wet etched laser device. Etching depth is reduced, following the reasoning described previously. However, sidewall quality still suffers from roughness. Dry etching was employed to improve roughness and sidewall profile.

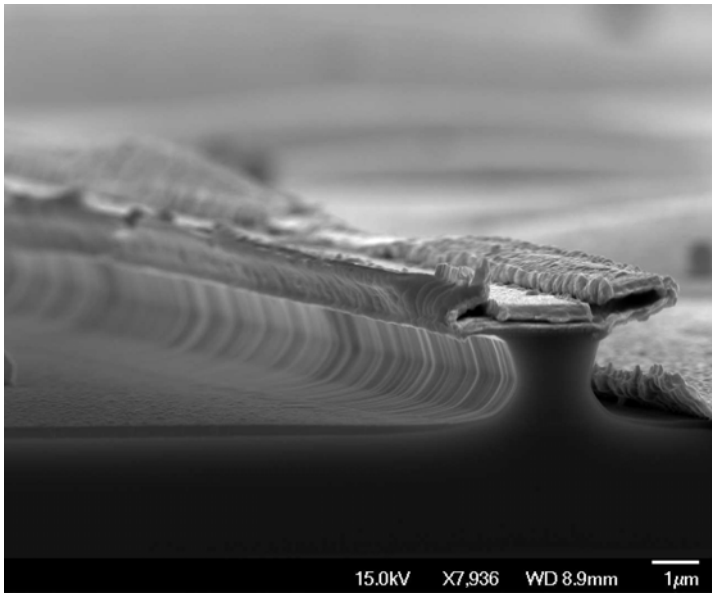

Figure 6.4.: Image of ridge sidewall roughness and profile using H_2SO_4 and H_3PO_4 etching solution

It is well established in literature that plasma containing BCl_3/Cl_2, etch GaAs and AlGaAs non-selectively. Furthermore, under proper plasma parameters, vertical and smooth sidewalls may be produced. If BCl_3 alone is used, the desired morphology (i.e. Vertical and smooth sidewalls) are obtained. However, BCl_3 etches resist almost as fast as GaAs.On the other hand Cl_2 plasma is too reactive resulting in isotropic etching and rough sidewalls. Slowly adding Cl_2 to BCl_3 increased etch rate of semiconductor material significantly. Resist etch rate which is mainly due to sputtering from B atoms, remained almost unchanged.

It was found that a ratio of 20/1 produces no surface roughness yet has an acceptable etching rate. To obtain vertical sidewalls the pressure of the plasma chamber was chosen to be 10mTorr. Higher pressure results in deviations from the vertical side wall morphology. Fig.6.5 shows the sidewall quality and the profile of a ridge etched using this process. Comparing Fig.6.3 and 6.5 provides a clear view of the improvement.

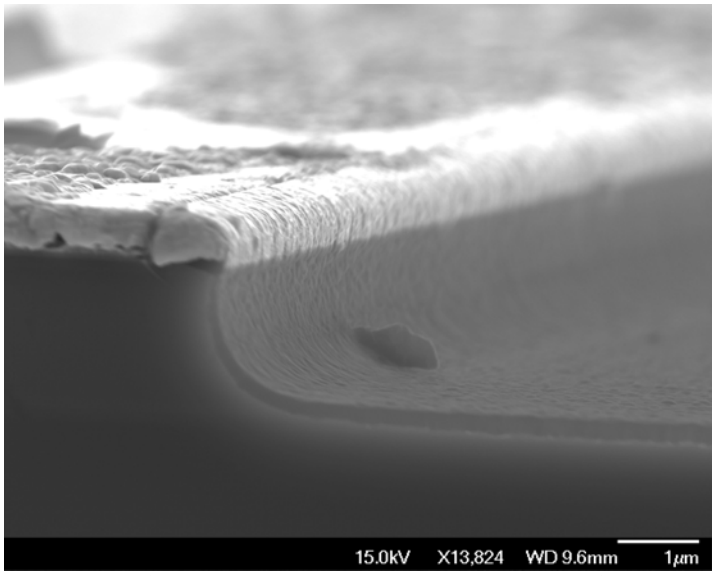

Figure 6.5.: Etch profile of BCl_3/Cl_2 dry etching process. Despite the increased magnification, roughness on the side wall is barely visible.

Finally, measuring reverse leakage current on the laser diodes and forward operation characteristics it was verified that this step produces no significant etching damage [65] (i.e. non-radiative recombination centers).

6.3.3 Dielectric deposition

Si_3N_4 dielectric layers are routinely used in compound semiconductor processing as dielectrics. PECVD grown Si_3N_4, produces layers of varying characteristics, depending on the growth parameters. Table 6.3 gives an overview of typical parameter values for stoichiometric (CVD) and PECVD deposited Si_3N_4. Si_3N_4 growth experience in our lab was mainly to create inter-capacitor dielectric for microwave integrated circuits (MMIC's). Such a Si_3N_4 is grown under conditions that provide high dielectric coefficient, much larger than stoichiometric Si_3N_4. For laser diodes, on the contrary, the desired characteristics are good dielectric strength (i.e. high breakdown voltage), good optical quality (no midgap absorption) and low outgasing (i.e. low hydrogen content).

Parameter	*Si_3N_4*	*PECVD Si_3N_4*
Refractive index	2 – 2.1	1.9 – 2.2
Dielectric strength (V/cm)	10^7	6 10^6
Thermal stability	Excellent	variable
Plasma etch rate (CF_4/O_2) [Å/min]	200	500
Si/N ratio	0.75	0.8-1.0

Table 6.3: Si_3N_4 typical parameters, reprinted from [58]

PECVD grown Si_3N_4 usually exhibits high hydrogen content. This may also affect material density. The Si_3N_4 initially grown using our equipment at 220ºC exhibited an exceptionally high dielectric coefficient (optimized for capacitor dielectric) but poor thermal stability and high H content. Si_3N_4 has to be able to withstand the n-ohmic contact annealing process. It is thus important to exhibit low H content and optimum thermal stability.

According to literature [58], an increase of deposition temperature, is expected to lead to higher quality films containing less Hydrogen. The initial deposition temperature (220ºC) was increased to 290ºC. Furthermore, higher pressure is expected to improve dielectric film density and improve refractive index characteristics. SiH_4 to N_2 ration was optimized by a series of experiments. Each film fabricated during this optimization process, was checked for breakdown voltage and leak current using metal-insulator-metal (MIM) configurations. Ellipsometry was performed to extract the optical characteristics (i.e. refractive index **n** and absorption **k**). Table 6.4 depicts the initial and final deposition parameters for Si_3N_4 grown on GaAs substrates.

Parameter	*MMIC optimized Si_3N_4*	*Laser optimized Si_3N_4*
RF Power (Watt)	50	60
Temperature (ºC)	220	290
Pressure (mTorr)	300	500
SiH_4 /N_2 flow ratio	4 10^{-3}	3 10^{-3}

Table 6.4: Deposition parameters for PECVD deposited Si_3N_4 before and after optimization for laser diode processing

Good thermal stability and significantly less outgasing were verified by outgasing rate measurements. In fact, optimized Si_3N_4 exhibited negligible gas release up to 400ºC. Annealing of the n-type ohmic contacts on final samples, did not result in interconnect metal blistering or adhesion loss as with the initial non-optimized Si_3N_4.

6.3.4 Si_3N_4 patterning

Si_3N_4 patterning is achieved by plasma etching, using CF_4 and O_2. Fluorocarbons such as CF_4 are known to create polymers in a plasma environment. O_2 is used to turn polymers into CO_x and/or other volatile molecules. Early experiments on interconnect metalization, revealed a poor contact with the underlaying metallic surfaces. This along with optical inspection of the samples surface after Si_3N_4 patterning suggested that polymeric residues may be sputtered on the surface of the sample.

To remove polymeric residues, a short (2min) O_2 plasma was used directly after the CF_4/O_2 etching. To avoid ohmic contact surface oxidation, low power was used.

6.3.5 Interconnect metalization

As described, the interconnect metalization is used to convey current into the device. A thick Au layer is deposited for that purpose. Given the fact that Au is diffusive, and interconnect metal is in contact with several layers, a diffusion barrier is placed below Au to improve reliability issues. An example of Au diffusivity is Si_3N_4. If Au diffuses in Si_3N_4, breakdown voltage of the dielectric deteriorates to the point where current leak becomes significant. Pt was initially used as a diffusion barrier. However, experiments with Ni indicated that it performs better. Wire bonding on the devices became easier and less damage occurred on the underlaying surface. This was evident from the high breakdown voltage of bonded laser diodes. Finally, a thin layer of adhesion metal is used. Metals that exhibit exemplary adhesion properties are Ti and Cr. Experiments with both options, showed that Cr adheres better on Si_3N_4 . Summarizing, the interconnect metal used initially (i.e Ti/Pt/Au) was changed to Cr/Ni/Au.

Another issue that was primarily addressed through optimization of the ridge sidewall profile, was the step coverage of the ridge. E-gun evaporation is known to exhibit shadow effect. Surfaces that are sloped or vertical receive a reduced amount of metal. The result is a thin layer of metalization or even metal discontinuity. Fig.6.6 (left) depicts the discontinuity of the interconnect metal observed on early devices. Tilting the substrate by 15-20 degrees so that the side wall is no longer parallel to the trajectory of the metal atoms, provides an easy way to deposit metal on these

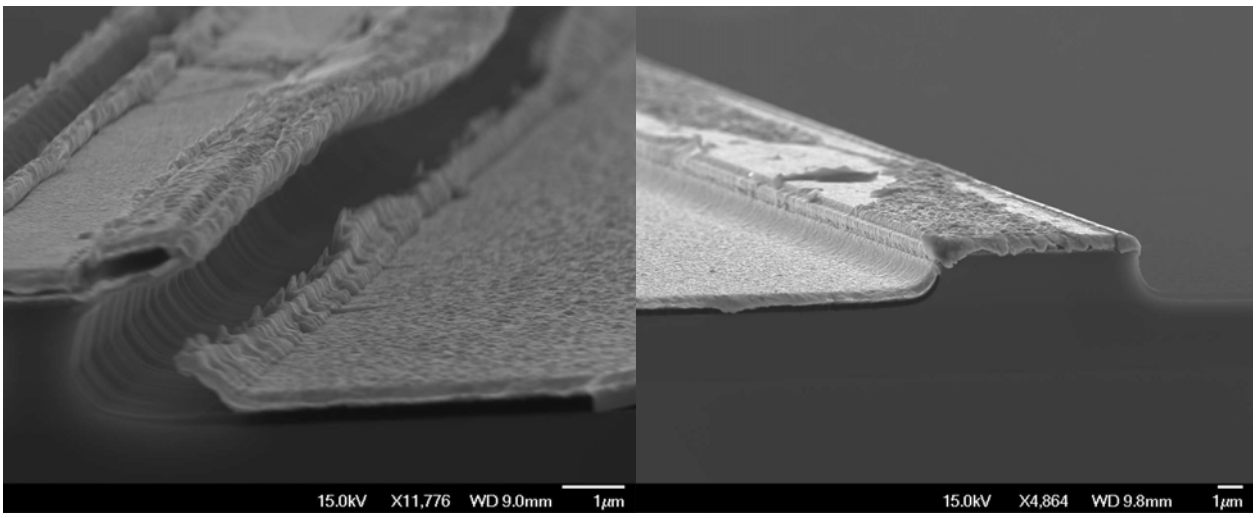

Figure 6.6.: ***Left****: Initial problems with the interconnect metal discontinuity because of the significant undercut.* ***Right****: Proper sidewall coverage because of vertical sidewall and angled evaporation.*

surfaces. SEM inspection of the step coverage shown in Fig.6.6 (right) reveals a continuous metal film attached on the Si_3N_4 as desired.

Finally, in order to further improve front interconnect metal behavior during annealing of the backside contacts, the Au thickness was reduced to 1000A. The final Interconnect metal deposited was: 20A Cr / 500 A Ni / 1000 A Au.

6.3.6 Backside n-contact

Backside n-contacts were used in this project. This necessitates contact annealing after the entire front side processing and lapping of the samples is completed. On the front side however, a number of layers with different thermal expansion coefficients exist. Heating the device to 410ºC is required to activate the n-contact. This imposes a significant thermal stress. Rapid temperature changes (as high as 100ºC/sec) occurring in an RTA chamber further stress the device. Experiments revealed that reducing the heating rate significantly improved front side layer behavior.

N-contact annealing was still performed at the same temperature and for the same duration. Good ohmic contact behavior was verified following this change and no significant differences were observed.

6.3.7 Electroplating

Following the backside contact annealing, a step to increase the front side, interconnect metal was introduced. Au was electroplated increasing the interconnect metal from 1500A to 1μm. This has a two fold impact on the devices. Firstly current conveyed to the p-contact is more homogeneously spread over the entire length of the device since resistance of the metal layer is now drastically reduced. Furthermore, since Au has a heat conductivity more than 0 times higher than GaAs, the thick interconnect metal acts as a heat spreader and thus improves heat behavior of the device when it is operating under high injection current.

Chapter 7.Electro-luminescence measurements

So far the techniques used to characterize the material itself have been introduced along with the analysis method to extract useful parameters. The ultimate goal of this project however is to create and characterize edge emitting laser diodes. Under normal working conditions a laser is operated using current input. Thus in order to measure a laser device's light output, electrical pumping should be applied.

The first section presents the setup developed to perform electro-luminescence measurements of laser diode devices. Subsequently the data analysis is split in two main sections. The first is generic laser diode characterization and may be applied to any laser diode device. The third and final section describes the additional analysis in order to measure the main characteristics of tunable laser diode devices.

Section:7.1.Developed experimental setup

7.1.1 Electrical pumping

Laser diodes consume power in the form of electrical current flowing through their contacts. As expected, a portion of this power is wasted on resistive parts (contact resistance, bulk resistance) and non-radiative processes. This power is transformed into heat on the device. Given the fact that current density typically applied in a working laser diode device is in the order of $10^3 A/cm^2$, and wall-plug (i.e. external power) efficiency is in the range of 50%, one expects a laser diode device to heat up significantly. In fact heat sinking is a major issue in laser diodes. In order to be able to measure the performance of a laser diode in a given temperature, without having to take into account heat dissipation and heating effects, laser diodes are typically characterized in pulsed operation.

This necessitates a source which is capable to provide current pulses, rectangular in shape (constant current) and short enough so that the device does not heat up. Furthermore, this pulse has to be abrupt (turn on/off time) so that the measured response corresponds to the main part of the pulse only. Subsequently, the current is turned off for a long time to allow the device to dissipate heat. The typical characteristics of such a pulse is depicted in the following table:

Parameter	*Typical value*
Current I_{ON} (mA)	0-2000
Pulse width [PW] (nsec)	200-1000
Rise Time [10-90%] (nsec)	20-50
Fall Time [90-10%] (nsec)	20-50
Duty Cycle (%)	0.1-1%
Current regulation (ΔI_{ON})	<1%
DC current I_{DC}	1μA - 100mA
DC current accuracy ΔI_{DC}	<1%

Table 7.1: Specifications for a current source to perform Electrical pumping measurements of Laser Diodes

Conversely, at low current levels, heating is not an issue. Furthermore, optical output is very low. Pulsed pumping would offer nothing in this regime on the contrary given the fact that average optical power is divided by the duty cycle factor, it would be necessary to measure a minute optical signal rendering measurements at very low current impossible. For this reason it is equally important to be able to supply a small but controlled DC current to tha device under test as well.

To meet the described specifications, a hybrid (analog+digital) electronic circuit was designed [66] and fabricated. To design the circuit, the program PSPICE was used to simulate each module separately and finally PROTEL© [67] was used to design the printed circuit boards. All boards were fabricated in the lab using standard 2 sided copper plated photo-resist coated commercially available boards and UV-lithography technique. As depicted in fig.7.1 the basic modules comprising a full-featured pulsed current source are the following:

- DC current source (Voltage controlled DC current output)
- AC current control module (DC current source + modulating network + current amplifier)
- Timing circuit (Voltage controlled rectangular pulse generator)
- Measuring module (measures voltage and current on the device)
- Digital control unit (provides auto-control voltages and mode of operation)
- Interface Unit (LCD, keyboard, RS-232 interface and analog input of control parameters)
- Power supply (provides all voltages necessary for operation)

In Appendix A the schematic of each module along with a brief description of the operational logic is described.

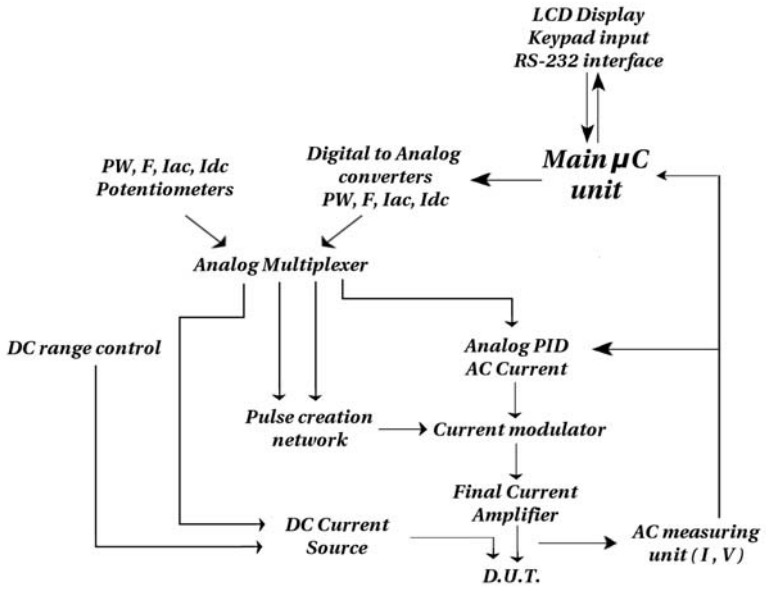

Figure 7.1.: The topology of the basic modules comprising the current source design implemented for the needs of laser diode measurements throughout this thesis.

7.1.2 Total emitted power output measurement

One important characteristic of a working laser device is the total emitted optical power. Not only does this measurement allow for characterization of efficiency of the laser device but as will be described shortly, several important characteristics may also be extracted.

Semiconductor laser devices emit optical power in a "peculiar" way. To begin with, the optical output diverges strongly when exiting the facet of the laser device. Common full width at half maximum (FWHM) angular power distribution is in the order of 100º or more in the direction parallel to the growth axis. This is expected if one bears in mind that the waveguide in this dimension is typically less than 1μm. To make things more complicated, in the direction parallel to the surface, the divergence is much smaller (~10º), making a strongly astigmatic beam. It should be noted here that these emitting characteristics hold true only for edge emitting devices. Vertical cavity laser diodes usually have no astigmatism and much less divergent beams, but these devices are out of scope for this document.

Finally, when no coating on the facets is applied – as in our case – the emitted power is equally distributed between the two mirrors. All these characteristics necessitate a careful approach to total power output measurement.

Total emitted power measurement setup

In order to collect and measure the emitted power from a laser diode device, the experimental setup shown in fig.7.2 was developed. Devices are placed at the edge of a gold coated Silicon plate that acts as the bottom electrode. A probe tip equipped with a micro-manipulator is used to contact the top side electrode of each laser device. Laser devices are electrically pumped using the current

source described in the previous section.

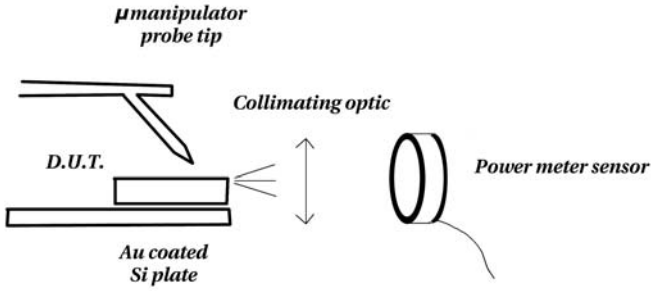

Figure 7.2.: Schematic of the total emitted optical power measurement setup.

A high numerical aperture lens (Melles Griot 06GLC001) was used in close proximity with the facet of the device that is placed at the edge of the plate. This multi element light collimating optic is designed for laser diodes. Its main characteristics are tabulated below.

Parameter	*Value*
Design Wavelength λ_o	830 nm
Anti-reflective Coating	Yes: MgF_2
Numerical Aperture	0.62
Working distance f_w	0.8mm
Transmitted wavefront error	$\lambda/4$
Transmission @ λ_o	99.75%
Transmission @ ±10% of λ_o	>99%

Table 7.2: Specifications of collimating lens 06GLC001 by Melles Griot.

It is important to note that this lens has been selected for its excellent transmission properties, the small working distance from the facet of the device and its high numerical aperture which ensures that even strongly divergent beams are successfully collimated with minimal power loss.

The collimating lens was mounted on an XYZ stage to allow for proper alignment with the laser device. The result of this setup is a collimated beam containing 99% of the emitted power from one facet of the device.

A calibrated optical power meter (Newport 1830c with sensor 883-UV) was used to record the optical power. It is important to note that the selected power meter, besides a calibrated measurement has a high maximum power density ($10W/cm^2$). The most common error done when measuring laser emission power, is focusing the laser beam on the surface of the power meter. In a well focused image of the laser facet, the entire output power impinges on a surface with area in the order of $1mm^2$. This, combined with a peak power of 100mW results in a power density of $100W/cm^2$. This optical density is far beyond the maximum power density of the measuring sensor leading to non-linearities and even possibly to sensor damage. To avoid this situation, the beam was

de-focused on purpose. A facet image size of 5x5mm is enough to reduce the power density by a factor of 25.

The main drawback of this setup was the fact that no temperature control of the device is possible. This restricts all total power measurement to room temperature. However the ease of use and the fact that no packaging of laser devices was necessary made this setup a useful tool for initial characterization.

7.1.3 Wavelength resolved optical emission setup

In order to measure the emitted intensity from a laser diode, the devices were placed in the setup for photoluminescence described in the previous chapter. Devices were mounted on a package and were interconnected using wire bonding. The vacuum chamber is equipped with an electrical feedthrough. This was used to interconnect package leads to the current source described in 7.1.1.

Light output was collected using the collection lens described in PL. Even though, only a fraction of the emitted light is collected this way, it is more than enough to record the intensity using the monochromator and CCD camera setup described previously. In fact, during lasing, the recorded intensity is too high. A set of **neutral density filters** were used when necessary to reduce the intensity so as to avoid overexposing and saturation of the CCD sensor.

To ensure that the measuring system recorded the light traveling inside the waveguide of the laser device, a small reflector was placed in front of the laser facet at 45º angle. The light exiting the facet is redirected perpendicular to the package and is thus collected by the collection lens.

This setup was used to measure wavelength resolved intensity at various pump current values and within a temperature range from 10 to 300K.

Section:7.2.Analyzing Laser Diode performance

This section aims to clarify the analysis of Laser diode performance. Starting from the measured data of optical power output and/or wavelength resolved emission, the way to extract the main characteristics of a laser device will be presented. Parameters specific to tunable laser diodes will be presented in the following section.

7.2.1 Threshold extraction

Both measuring setups are able to provide threshold information. Each following a different procedure. As will be shown when presenting experimental results later on, both methods produce the same threshold results, as expected.

Threshold extraction from total optical power measurements

The setup provides a single facet average optical power measurement. In order to convert this to *absolute total emitted optical power* we need to take into account that devices are under pulsed excitation and the fact that output power is equally distributed between the two mirrors (for non-coated mirrors)

It is easily shown that

$$P_{peak}^{opt} = \frac{P_{avg}^{opt}}{Duty\ cycle} \tag{7.1}$$

Thus, with a duty cycle in the order of 1% the measured value should be multiplied with a factor of 100 to obtain the peak power emitted from the device. Furthermore, an equal amount of power is emitted by the second facet, hence to obtain the total emitted peak power, the result from eq.7.1 should be increased by a factor of 2.

$$P_{total}^{opt} = \frac{2 \cdot P_{avg}^{opt}}{Duty\ cycle} \tag{7.2}$$

The duty cycle for square pulses, is calculated by taking into account the pulse width and the repetition rate of the driving current source. $Duty\,Cycle = P_{width}[sec] \cdot Rep.\,rate[Hz]$ (7.3)

Combining the last two equations we finally obtain: $P_{total}^{opt} = \frac{2 \cdot P_{avg}^{opt}}{P_{width}[sec] \cdot Rep.\,rate[Hz]}$ (7.4)

which is used to calculate the total emitted optical power of a device.

In our experiments 500nsec wide pulses were used. Repetition rate was set to 10KHz. This results in a duty cycle of 0.5% or in other words a correction factor of 200.

Optical output power measured data provide average emitted optical power (mW) vs current (mA). The latter can be translated to current density $J = \frac{I}{w \cdot l}$ (A/cm^2) as long as the width (w) and length (*l*) of the device are known. This way the emission from devices with different geometrical characteristics may be compared.

Fitting P_{out} vs J data obtained from the lasing part for each device, using the linear equation: $P_{out} = A+B \cdot J$, the threshold current density is calculated by:

$$J_{th} = \frac{-A}{B} \tag{7.5}$$

where B is an indication of the efficiency (W·cm^2/A) of the laser device, also known as external differential efficiency. Furthermore, the **differential quantum efficiency** n_d may be calculated using the recorded data and the following equation:

$$\eta_d \equiv \frac{1}{h\nu} \cdot \frac{dP_{out}}{dI} \tag{7.6}$$

where *h* is the Plank constant and *hv* is the photon energy. In the following section a more detailed discussion will be presented regarding the efficiency analysis of the laser devices.

Besides the fact that this setup is limited to room temperature measurements, the main drawback of this method lies in the fact that to obtain a decent fit of lasing power with current, a significant current range has to be recorded. On the other hand, this method provides not only threshold information but efficiency estimate as well. The analysis followed to extract efficiency from the measured data will be discussed below.

Threshold extraction from spectrally resolved intensity measurement

As discussed previously, there is also the possibility to spectrally resolve the emission from the laser device under investigation.

Below threshold, where a laser diode operates much like an LED, the emission spans several nm corresponding to the carrier distribution inside the bands. As soon as lasing threshold is reached, stimulated emission kicks-in. Since the gain inside the material has a maximum at a specific wavelength, it is only around this wavelength that lasing occurs. This manifests in the I(λ) plot as an intense narrow emission on top of the spontaneous emission background. Further increase of the pump current leads to several orders of magnitude increase in the stimulated peak intensity.

The pump current for which the signature of stimulated emission is initially observed, is the threshold current of the device. Although this may be a seemingly subjective measurement, it is so sensitive that an accurate estimation of the threshold is possible.

Although the respective setup is more complex since devices need to be packaged and carefully interconnected, there is no need to couple all the light output of the device into the spectrometer. In fact, alignment needs are relaxed. Furthermore, there is no need to further increase the pumping current if only the threshold is needed.

Finally, threshold measurement with temperature is possible using this setup.

7.2.2 Measuring internal losses

Utilizing the technique described in the previous section, namely, the total power output versus current, one may estimate the efficiency of the laser device.

It is worth pursuing the analysis further since we may extract more important characteristics of the laser diodes.

Absorption coefficient and internal quantum efficiency

As already described, the differential quantum efficiency may be extracted from total power output measurements. Differential efficiency n_d and internal quantum efficiency n_i are related through

$$\eta_d = \eta_i \cdot \frac{\frac{1}{l} \cdot ln\left(\frac{1}{R}\right)}{\alpha_i + \frac{1}{l} \cdot ln\left(\frac{1}{R}\right)} \tag{7.7}$$

Where R is the total reflectivity of the laser's facets and a_i is the internal loss in the cavity. Carefully looking at eq.7.7 one may recognize in the numerator the emitted photons whereas the denominator is nothing short of the total number of generated photons. This may be rewritten into:

$$\frac{1}{\eta_d} = \frac{1}{\eta_i} + \frac{1}{\eta_i} \cdot \frac{\alpha_i}{ln\left(\frac{1}{R}\right)} \cdot l \tag{7.8}$$

It is evident that measuring n_d (using eq.7.6), for devices with different cavity length, and

plotting 1/ n_d vs l, both n_i and a_i can be extracted from the intercept and slope of the plot respectively.

This method is able to calculate experimentally the internal losses inside a device using only a set of laser diodes fabricated the same way but with varying cavity length. Internal losses are directly linked to the laser structure as well as fabrication quality of the laser devices. A high quality laser diode will exhibit low internal losses. Using this analysis the internal quantum efficiency of a device may also be deduced.

7.2.3 Threshold vs cavity width

The internal losses discussed in the previous paragraph may be attributed to two different mechanisms.

One is photon scattering from the bulk of the device. This is difficult to overcome and depends from the structure design. A general rule of thumb is that the core of the laser device were most of the radiation resides, has to be doping-free since dopants act as scattering centers. Of course, there are several refinements one could implement to address this issue further. A typical structure may have α_i in the order of a few cm^{-1} due to this phenomenon.

The second and most important contribution to losses, is the scattering that occurs at the sidewalls of the laser diode. This strongly depends on the roughness of the surface that is created during processing of the device, the refractive index difference between ridge and surrounding material and the percentage of the cavity mode that reaches the interface. This mechanism usually contributes the most in internal losses and there have been many approaches to reduce sidewall scattering (regrowth, high index dielectric coatings e.t.c.).

In order to clarify the origin of the measured internal losses in a laser device fabrication, the dependence of α_i with cavity width may be measured. If we completely neglect sidewall scattering we expect that reducing the width of the device by half, will also halve the threshold current. This will hold true to the point where the width becomes comparable to the wavelength of the emitted radiation.

On the contrary a rough device that has an α_i mainly due to sidewall scattering will still have a high threshold of operation since losses remain unchanged or even increase as emitting modes are closer to the sidewalls. In practice there is an optimum width that produces the minimum threshold current density. Obviously the less the sidewall scattering the smaller the optimum width.

7.2.4 Threshold temperature dependence

With increasing temperature, the fundamental change that comes into play is the different Fermi distribution of carriers inside the bands. This in turn leads to a decrease of the maximum gain since carriers span a larger energy region. The fact that threshold current is directly associated to the gain maximum, leads to the logical assumption that increasing the temperature will increase the threshold as well. This has been well documented in the literature. In fact, an empirical formula describing the temperature dependence is eq.7.9.

$$J_{th} = J_{th}^{o} \exp[\frac{T}{T_o}] \tag{7.9}$$

where J^o_{th} is the threshold at zero temperature and T_o is the characteristic temperature of the laser device. In general, T_o depends on the material and the laser structure. For AlGaAs laser diodes is in the order of 100-200°Kelvin.

In general, the higher the bandgap of the material, the higher the characteristic temperature T_o. This is expected since higher bandgap translates to higher confining potential inside the laser structure.

It is understood that the higher the T_o is, the smaller the threshold variation over a given temperature span will be. An unusually low characteristic temperature is a signature of non-radiative recombination paths inside the active region of the laser. InGaAsP lasers for example although they have higher bandgap are known to suffer from Auger recombination and thus have a characteristic temperature only around 80°Kelvin TODO: “Reference”.

Section:7.3.Measuring emission tuning

Although semiconductor lasers usually have a fixed emission wavelength, there are exceptions to this rule. Tuning may be achieved in numerous ways, either cavity mode tuning or gain tuning. Spectrally resolved intensity measurements is the only way to get information regarding the lasing modes, spectrally resolved gain information and effective refractive index within the cavity. The discussion here will only be limited to edge emitting laser devices, that achieve tuning using gain. A general discussion would be out of scope in this text.

7.3.1 Laser diode emission wavelength

Laser emission in any laser device is a superset of cavity modes and the gain curve. In edge emitting laser diodes, cavity modes are closely spaced. The mode spacing is given by:

$$\Delta\lambda = \frac{\lambda^2}{2\bar{n}_g \cdot l} \tag{7.10}$$

where n_g is the group effective index given by:

$$n_g = n - \lambda(\frac{\partial n}{\partial \lambda}) \tag{7.11}$$

Edge emitting laser devices are typically long (l > 200μm) thus Δλ is small, in the range of 1nm. Contrary to gas lasers, semiconductors have a broad gain spectrum, several tens of nm wide. This allows for several cavity modes to experience gain and thus reach lasing. Broad edge emitting laser devices also exhibit multiple lateral modes further increasing the available modes for lasing.

In a laser diode, close to lasing threshold only a few modes may obtain enough gain to lase. As soon as pumping is increased, the gain curve is clamped for those modes (stimulated emission depletes carriers fast) and the top of the gain curve may experience a flat top merely including more modes. Such a situation will result in multimode operation.

Since the maximum gain position is fixed to first approximation, lasing will be also fixed. Such a laser diode is typically designed to have a fixed emission wavelength and only thermal effects

may cause the emission wavelength to shift due to bandgap thermal effects.

However, there are cases were the gain curve may shift significantly due to other phenomena. Stark effect inside the active medium would result in such a shift. In such cases, it is expected that the lasing modes will increase as in a typical device but their envelope, corresponding to the gain curve will also shift. In the following paragraph, we will present the two main methods to quantitatively measure the observed shift.

Dominant emission

The easiest way to measure shift is to record the dominant lasing wavelength. In cases where the cavity modes are closely spaced together, this is actually where the gain maximum occurs. This method is fairly accurate for narrow stripe lasers, where dense longitudinal cavity modes exist, yet not many lateral modes may survive the modal competition. In such a measuring scheme, one may expect to see the dominant wavelength hopping from one cavity mode to the next one as the gain maximum shifts through the proximity of each supported mode. This method suffers from the fact that mode hopping is often observed in semiconductor lasers. An insignificant change may result in mode hoping. However, this is recorded as an actual shift in emission wavelength. Furthermore, cavity interaction with the substrate or other weakly coupled components of the device may create a beating effect, increasing the uncertainty as to where the actual gain maximum resides.

Weighted emission

A more sophisticated way to approach gain maximum would be to average emission wavelength for each mode using as weight the corresponding intensity. A multimode emission with the dominant mode on one side, is thus properly treated. Keep in mind that differences in gain that lead to dominance of a lasing mode may be trivial. Sometimes a minute difference in mode losses may be the sole reason that a cavity mode has lost intensity.

Furthermore, the emission wavelength is to some degree decoupled from cavity spacing as long as there are a few cavity modes lasing simultaneously. This is the method of choice to preserve cavity mode immunity when measuring shift in a laser diode such as the ones fabricated in our work.

It should be noted that below threshold, where spontaneous emission is recorded, both methods should be able to record shift with reasonable accuracy.

7.3.2 Emission and pump Current

Following the rational developed in the previous section, emission spectra may be recorded at different pump current for a given device. Normal diodes should exhibit minimal emission shift provided no self heating is caused by the pump. On the other hand, Stark tunable devices like the ones fabricated in our work, should exhibit a concise shift with current.

Obviously, for laser devices, wavelength shift occurring below threshold is wasted. It is however important to check the ability of each structure to provide a Stark-induced shift. A single plot is produced spanning the emission wavelength from μA of current flowing through the device all the way to large current, several times the threshold current. The lasing threshold is then

depicted on the plot, to make it clear which part of the shift is actually lasing wavelength shift.

7.3.3 Emission shift with temperature

Plotting the emission shift for several temperature values, will provide a clear view whether the shift persists with temperature or not. It is worth noting that the lasing threshold will also change with temperature, moving to higher currents, as the temperature increases. This is the main reason why we chose to depict both below and above threshold shift vs current in a single viewgraph. The ultimate goal is to make a temperature insensitive – in terms of shift (i.e. tuning) – tunable laser diode that will exhibit most of the shift during lasing.

Chapter 8.Reference Laser diode performance

A laser diode is a complicated device, both in terms of fabrication as well as in terms of physics involved in its operation. In order to study the tunable devices in this work, it is important to have a well studied reference. The best way to achieve this is to characterize "normal" (i.e. non-tunable) laser diode devices. For this reason a set of reference laser diode structures were fabricated, identical to the tunable ones but with no tuning mechanism. It is these devices that are presented here, to establish the reference for this project.

As discussed earlier, in the process of waveguide optimization, a major change in the structure design was done half-way through this project. For this reason two reference devices were fabricated corresponding to structure A and structure B.

Section:8.1. Structure A

Threshold vs cavity dimension

The dependence of threshold current density to cavity length reveals information about mirror

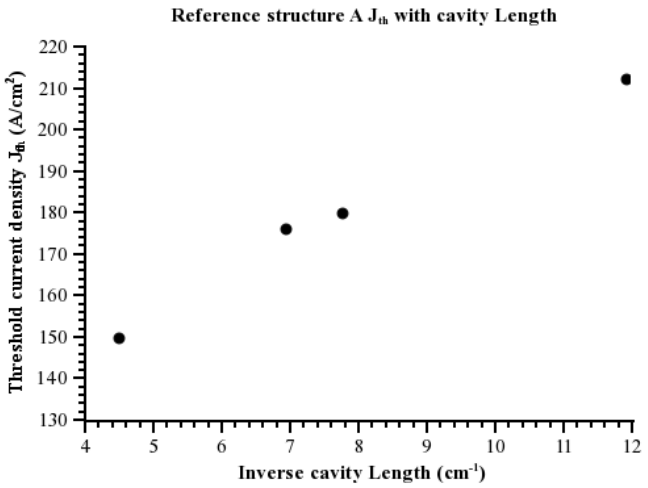

Figure 8.1: Dependence of J_{th} with inverse cavity length. The slope is directly connected to the internal cavity absorption a_i.

losses and the intrinsic absorption inside the cavity as well as the scattering effects due to imperfections on the side walls of the device.

Fig. 8.1 depicts the room temperature lasing threshold for various device lengths. The x axis is 1/L so as to obtain a linear dependence of threshold. As expected, short devices exhibit higher $J_{th.}$ This is easily understood if we take into account that the mirror losses, which enter in the roundtrip gain equation at threshold, scale with 1/L.

Fig 8.2 depicts the lasing threshold current density for various device width. The fact that J_{th} increases for reduced width is attributed to the increased scattering losses on the side walls of the device. The thinner the laser device, the more important the scattering on the sidewalls. As discussed in the previous chapter, a redesigned fabrication process allowed to significantly improve

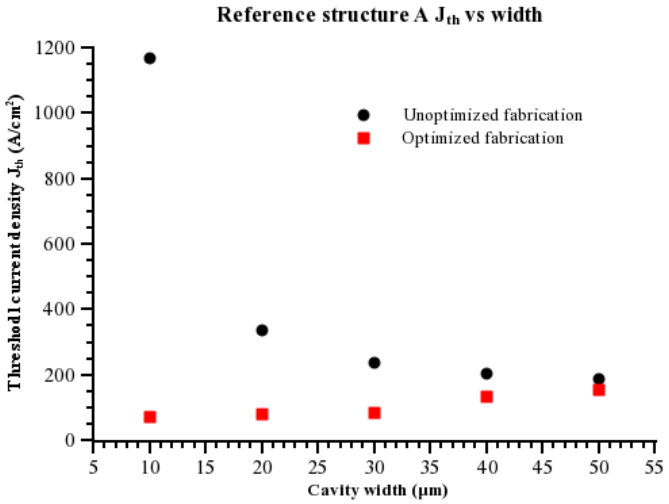

Figure 8.2: Dependence of J_{th} on cavity width. Black dots correspond to initial fabrication process which resulted in poor quality laser diodes. The scattering caused by side wall roughness increases the losses as the cavity width decreases. On the contrary red squares correspond to the optimized fabrication. The threshold decreases as expected due to reduced lateral optical mode competition. The impact of scattering losses is negligible down to a *10μm wide cavity.*

the sidewall roughness, which was expected to reduce the scattering term and the optical losses in the cavity. The difference is pronounced in the narrow cavity regime where threshold was reduced by a factor larger than 10.

Performance vs operating conditions

Plotting the threshold density of a single device with temperature we obtain Fig.8.3.

It has been established that the expected temperature dependence of J_{th} is following the equation $J_{th}^{T} = J_{th}^{o} \cdot e^{\frac{T}{T_o}}$ Thus a figure of merit as to the temperature behavior of a laser diode device is the characteristic temperature T_o. The higher the T_o the less prone the device is to temperature changes. Fitting the previous equation into the data of Fig.8.3 we obtain a value for $T_o = 175 \pm 1$ Kelvin.

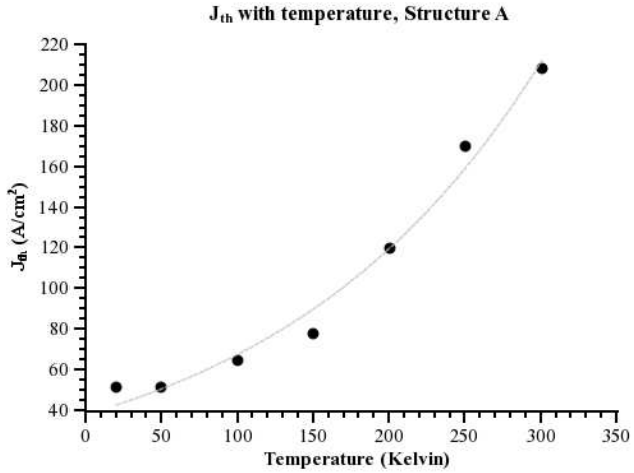

Figure 8.3: Dependence of threshold current density J_{th} on device temperature. The grey line corresponds to the exponential dependence fitted on the experimental data. The characteristic temperature is calculated to be T_o=175Kelvin.

Typical values for T_o for GaAs/AlGaAs laser diodes is between 100 and 200 Kelvin.

Fig.8.4 shows the emission shift of the reference sample A with current.

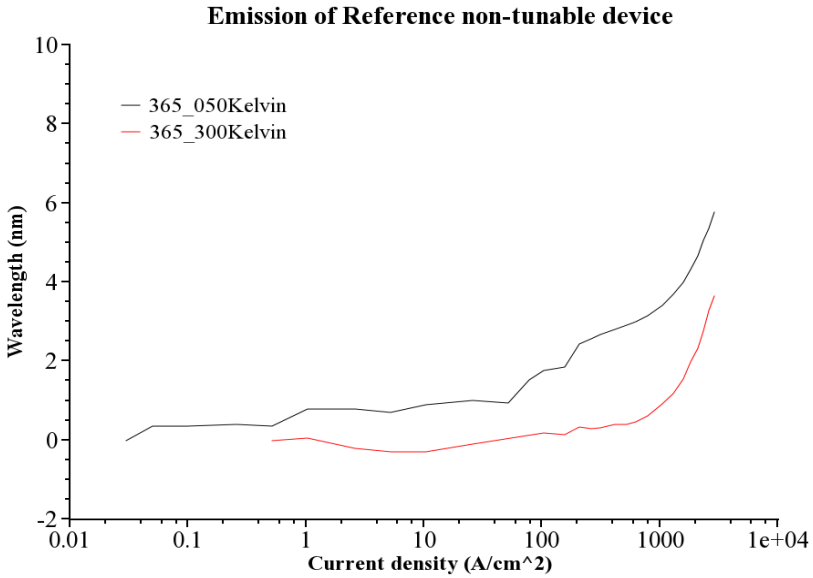

Figure 8.4: Emission shift for reference non tunable structure A. The emission wavelength is almost constant up to large current density. At large pump current the emission shifts linearly with current indicating heating effects. Pump current scale is logarithmic. Similar shift is observed for low (050K) and high (300K) temperature.

Until the KA/cm^2 regime, there is no significant shift observed. However as can be seen in Fig.8.4 for larger current densities there is a systematic shift of the order of a few nm. Specifically, the observed shift appears to be linear with current. This behavior is characteristic of heating effects.

Heating effects

Based on the findings of the previous paragraph, it is evident that for high current density, the laser diodes exhibit some limited but existing heating effects. To further clarify the origin of this effect, a series of pulsed measurements was performed on the reference devices. In these measurements there are two adjustable parameters, namely the pulse width and the repetition rate. Although both influence the average power dissipated in an operating device, there is a significant difference.

Repetition rate has to be low enough so that the device is given enough time, in the OFF state (no current is applied during this time), to return to the ambient temperature. Repetition rate related heating is mainly associated with packaging and macroscopic heat dissipation.

On the contrary, pulse width influences the amount of energy dissipated in the device within a single pulse. Although the device may start operating at ambient temperature at the beginning of the pulse, if the pulse is long enough, the device's temperature is increased within the pulse duration. During this time which is in the order of 100's of nsec in our case, there is limited heat flow towards the package and the heat sink. Ideally the devices should be operated at a repetition rate that is low enough to extract the produced heat and a pulse width that induces insignificant temperature changes during the ON state of the pulse.

Overall, both parameters influence the duty cycle which coincides with the factor of peak to average power dissipated on the device. Usually the duty cycle is kept below 1% and the pulse width is kept below 1μsec in pulsed laser diodes measurements. In our experiments, the pulse width is 500nsec and the repetition rate is 10KHz resulting in a duty cycle of 0.5% corresponding to a peak to average power factor of 200.

Repetition rate

To make sure that the observed phenomenon is not heat-sinking related, the emission wavelength was measured for two different repetition rates. The first, used throughout this project, is 10KHz and the second, a much lower one, is 6KHz. The average power budget was thus reduced to 60% of the original value.

Fig.8.5 depicts the two emission wavelength curves. As is obvious the two curves coincide. This translates to the fact that at the beginning of the pulse, the device temperature is restored to its initial value (i.e. ambient temperature).

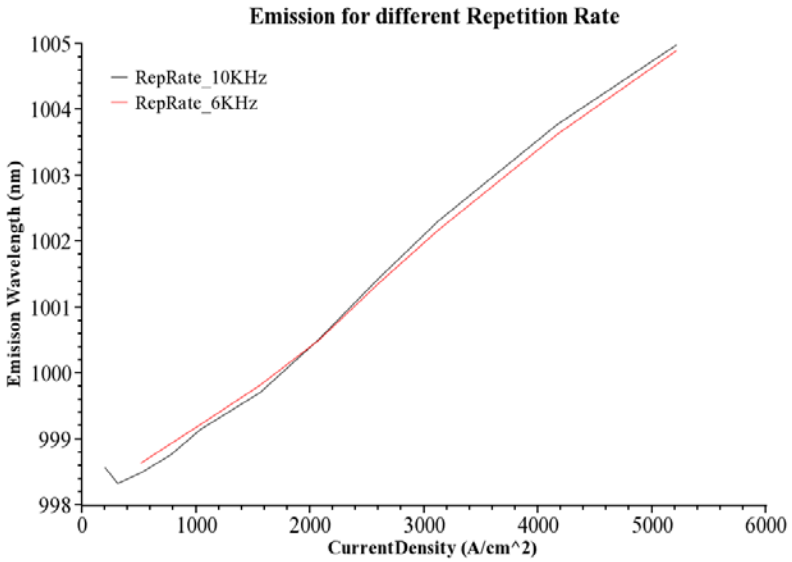

Figure 8.5: Reference non-tunable device emission shift for two different repetition rates (10 and 6KHz) of the pulsed pump current. The emission behavior coincides for the two curves indicating that the average power is adequately dissipated from the package.

Pulse width

Fig.8.6 depicts the emission shift with pump current for varying pulse width. It is immediately evident that the device is changing emission wavelength during pulse operation. The emission near the start of the pulse is on the blue side whereas the emission during the end of the pulse is red-shifted. This is clear evidence that the device's temperature is increasing during a single pulse. In other words, the energy per pulse is high enough to cause a limited amount of heating in the active region of the waveguide.

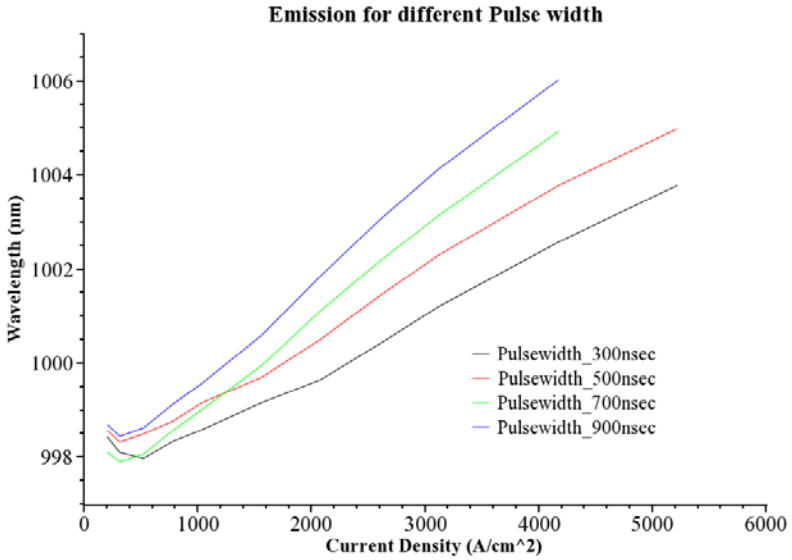

Figure 8.6: Reference non-tunable device emission wavelength at room temperature, for different pulse width values. The higher the pulse duration, the more the redshift of the emission. This indicates heating within the pulse duration.

One possible course of action to reduce or even eliminate this effect, would be to decrease the pulse width so that the energy per pulse is decreased to the point that no heating effect is observed within the used current density range. The technical difficulty that arises is to obtain a pulse with constant, regulated, current and short duration. As discussed in previous chapters, the current pulse that is used to pump the devices has a rise/fall time in the order of 30nsec. This is actually larger due to the capacitance and impedance of the wiring used to connect the laser devices under test, especially in the cryostat assembly. Using a very short pulse (comparable to the rise/fall time of the pump current pulse) would rise questions concerning the current stability of the measurement. For this reason, it was deemed preferable to keep the pulse width at 500nsec which is roughly 10 times larger than the expected current transient effects.

Temperature related emission shift

In order to be able to distinguish between tunability due to stark effect shift of the gain and thermal effects, it is important to devise a concise way to subtract heating effects. As is expected, thermal wavelength shifting is linear with current density flowing through the device. Plotting the emission wavelength of the reference sample – shown in fig. 8.4 – in linear scale, we obtain fig.8.7. The black curves correspond to the measured data. Using a linear fit to predict the thermal shift and subtracting it from the measured data, we obtain the red curves. As may be observed, the remaining shift, caused by other effects, is less than 1.5nm.

In the following paragraphs we will use this technique to remove thermal effects from measured emission shift data.

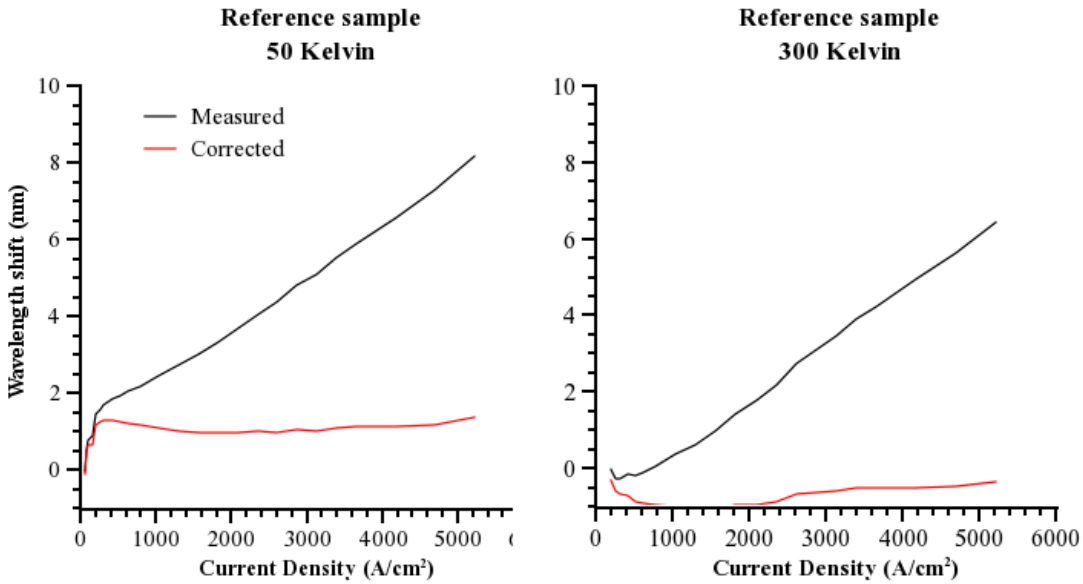

Figure 8.7: Applying a simple linear model to calculate and correct the thermal shift observed in the reference sample, reduces the remaining shift to less than 2nm.The same manipulation is applied to the tunable samples.

Section:8.2.Structure B

Similar measurements were performed for the reference sample fabricated based on the second waveguide design. Besides obtaining a reference for the tunable structures fabricated using the second waveguiding structure, the performance of the two structures may be compared to validate whether there is an improvement of their main characteristics.

8.2.1 Threshold vs dimensions

Fig. 8.8 shows the threshold current density of devices for various laser diode length.

Note that devices appear to be grouped in two areas marked with arrows on the plot. One exhibiting high threshold current density and the other exhibiting low J_{th}. This is attributed to the defect density on the semiconductor material. Devices containing a defect exhibit a large threshold whereas devices exhibiting no defects in the active region exhibit a low threshold.

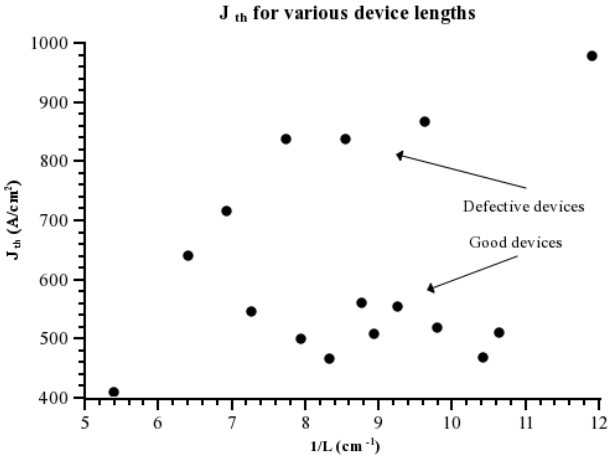

Figure 8.8: Threshold current density at room Temperature with inverse device length. Grouping of data points reveals a set of defective laser diodes (high threshold) and a group of good devices (low threshold) marked with arrows.

Fig. 8.9 shows the threshold current density for varying laser width. As expected the threshold density reduces with decreasing laser width.

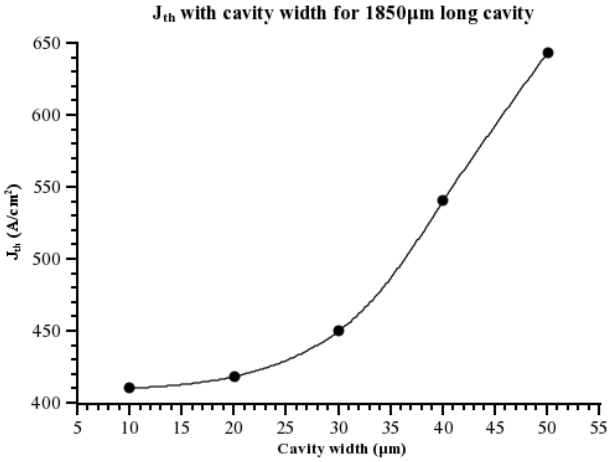

Figure 8.9: Threshold current density dependence on cavity width. As expected, the threshold reduces with cavity width. This is expected as lateral modes sustained by the cavity reduce with the cavity width.

A narrow cavity laser sustains less lateral modes. Less lateral modes in turn result in reduced mode competition. As long as scattering from the side walls is insignificant, the threshold is expected to reduce with laser width.

8.2.2 Performance vs Operating conditions

It is also important to define the laser performance for various operating conditions. The first important parameter is to obtain the temperature dependence of lasing operation. Fig.8.10. Shows the threshold current density for varying temperature.

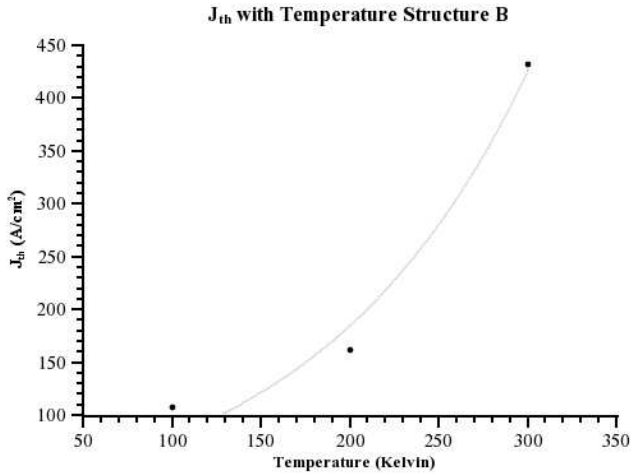

Figure 8.10: threshold current density (J_{th}) with Temperature for Reference structure B. The line corresponds to the exponential fit used to extract the characteristic Temperature (T_o) described in the text.

Fitting this with an exponential growth equation we obtain a characteristic temperature T_o=208±1 Kelvin. Which is high compared to typical AlGaAs based laser devices.

Finally, the emission wavelength for varying current above threshold is depicted in Fig.8.11.

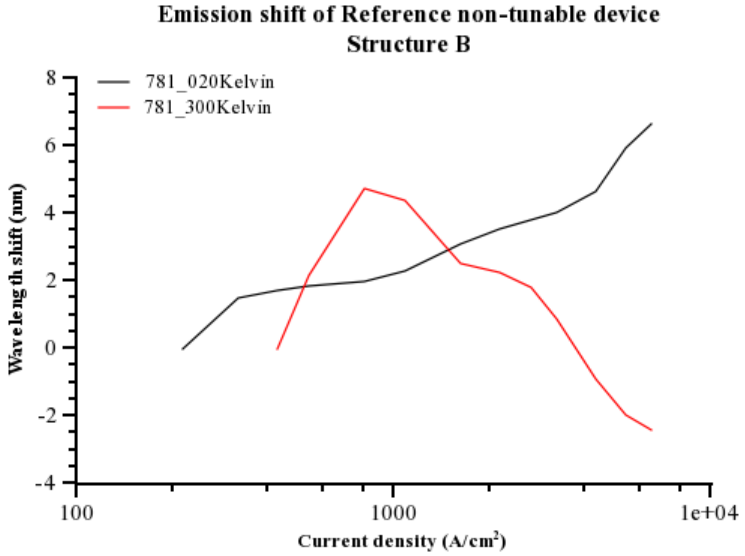

Figure 8.11: Emission shift of reference structure B. Note that the emission shift is positive for low temperature (red-shift) whereas it is negative for high temperature (blue-shift).

It is interesting to note that although for low temperature, the emission shift is positive, at high temperature there is a slight blue shift observed. This may be explained if we take into account that for high temperature, the gain maximum is flat over a large energy range, due to the Fermi probability being less abrupt. The blue shift is also an indication that heating effects no longer play a dominant role in device emission wavelength.

Heating effects

To further study the thermal behavior of devices based on the new structure we have measured the emission wavelength for different pulse width. As already discussed when studying the initial

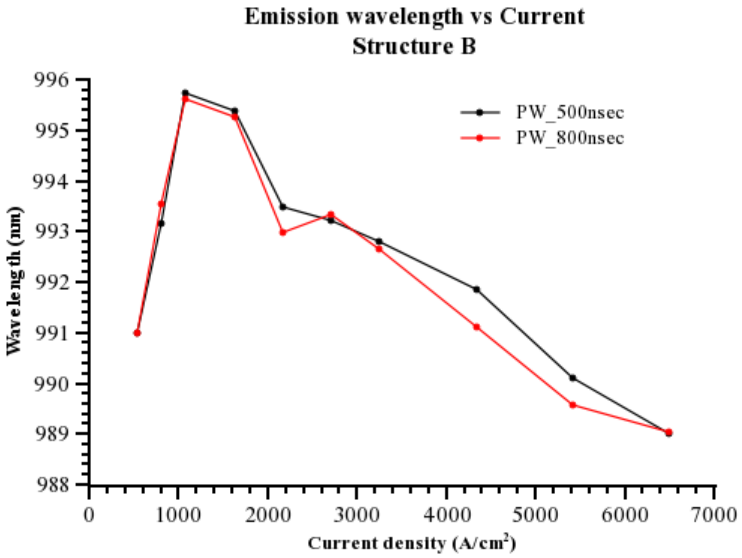

Figure 8.12: Emission wavelength of reference laser diode based on structure B. Increased pulse width results in no change in the emission. This indicates that heating effects are strongly suppressed. The total shift is attributed to other phenomena, as band filling.

structure, it was the pulse width that had a detrimental effect on the emission wavelength indicating heating of the device during pulse on state. Fig.8.12 depicts the emission wavelength during lasing operation for two different pulse width values. The two plots coincide indicating that no emission wavelength change occurs when changing the dissipated power per pulse, this indicates that heating phenomena do not occur in these laser diodes.

Section:8.3. Summary

The following table summarizes the main performance characteristics of the two reference laser diodes.

	Structure A	*Structure B*
Optimum w	Corrected	<10μm
T_o	175	206
J_{th}	208	430
Heating	Yes	No

Table 8.1: Comparison of the main characteristics of the two reference laser diode structures.

As already discussed, optimizing the fabrication process, we successfully managed to reduce the sidewall scattering which was responsible for elevated threshold current in the initial fabricated devices. Using the optimized process, we were able to achieve the lowest J_{th} for narrow laser diodes which at the same time exhibit the best performance in terms of mode emission.

Furthermore, using the second structure the characteristic temperature of the devices was increased to more than 200Kelvin. This results in lower room temperature threshold. As will be discussed later, it is significant to obtain low threshold of operation in order to be able to achieve significant tuning.

It is interesting to note that although structure B appears superior as expected, there is a discrepancy in threshold current density. Specifically the second structure exhibits a J_{th} larger by a factor of 2. In order to explain this unexpected behavior, we have to look in Fig.8.13 which depicts the photoluminescence at 20Kelvin from the two samples. The first sample (365) which corresponds to structure A, has a FWHM emission of 2.43nm whereas the second sample (781) has a FWHM of 6.44. This is attributed to roughness in the quantum well during growth. Although the integrated PL differs by 26% between samples, (integrated PL is a figure of merit to the efficiency of the device's luminescence, which is expected to be close to unity in low temperature), the maximum intensity differ by a factor of 5.

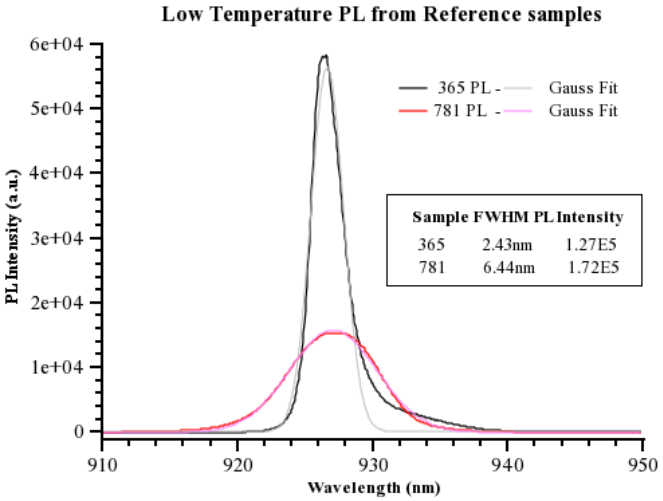

Figure 8.13: Photoluminescence emission from the two reference structures. PL emission maximum is directly associated with gain maximum. The second reference (structure B) has an abnormally high FWHM which is attributed to roughness of the quantum well. The dramatic decrease in PL maximum is obvious. Both spectra are taken with similar parameters for comparison.

Taking into account that the maximum gain is directly proportional to the maximum intensity of the luminescence, it is expected that structure B, requires much larger pumping current to reach the same gain. This translates to much higher threshold. Sample roughness was identified as the issue in this structure using optical inspection of the surface morphology. Furthermore, subsequent samples based on structure B (to be presented later) exhibit room temperature threshold as low as 100A/cm^2 which is one of the lowest values reported in literature for GaAs/AlGaAs based edge emitting laser diodes.

To conclude, optimizing the structure we have managed to improve both the threshold dependence with temperature as well as minimize the heating effects when operating the devices at high pump currents.

The higher Al content cladding used in structure B, was expected to improve carrier leakage effects thus improve the temperature dependence of the threshold. Heating effects on the other hand, where successfully addressed by changing the process of the laser devices. The reduced MESA depth, resulted in more crystalline material surrounding the active region, thus better thermal dissipation and less non-radiative effects. Furthermore, a significantly enhanced heat dissipation is expected from the thick interconnect metal, directly above the laser diode stripe.

Part III: Laser diodes with E fields, characterization and modeling

Chapter 9.The concept of this project

Having a broad overview of the existing tunable laser diodes one easily distinguishes a striking void in performance. The existing broadly tunable laser diodes are either unable to switch fast between wavelengths or are complicated to control involving feedback electronics. This is important for a number of applications.

The aim of this project is to design and manufacture a room temperature broadly tunable laser diode based on the quantum confined stark effect (QCSE-LD). The proposed edge emitting laser diode is expected to be broadly tunable, operate at room temperature and tune its emission wavelength within nsecs. In this chapter we will present the basic idea enabling us to take advantage of QCSE tunability in a laser diode structure. The first section presents the basic laser diode structure that will be used. The following section describes the concept of QCSE and the final section describes the modifications necessary to establish a laser structure that exhibits QCSE laser emission.

Section:9.1. Non tunable structure

The basis of this work is a **single quantum well separate confinement double heterostructure** (SQW-SCDH) shown in Fig.9.1.

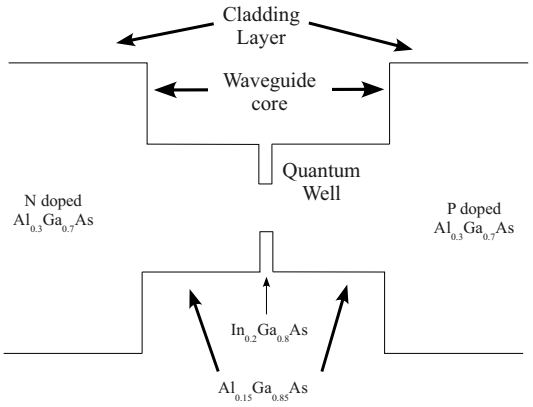

Figure 9.1.:Schematic of the band diagram of a Single Quantum Well Separate Confinement Double Heterostructure (SQW-SCDH)

Table 9.1 depicts the layers of the structure. The $Al_{0.3}Ga_{0.7}As$ layers are the cladding layers. Note that the bottom layer is thicker. That is to decrease mode coupling with the substrate (GaAs) which is transparent in the emission wavelength range and thus may act as a waveguide. Top and bottom highly doped GaAs is used to form electrical contacts. The $Al_{0.15}Ga_{0.85}As$ forms the core of the waveguide. Finally the center of the structure is an $In_{0.1}Ga_{0.9}As$ quantum well that acts as the active material. Carriers are trapped inside the potential well of the quantum well and eventually recombine to produce photons.

Material	*Thickness*	*Doping*
GaAs	250nm	P+ 10^{18} cm^{-3}
$Al_{0.3}Ga_{0.7}As$	1.6μm	P 10^{17} cm^{-3}
$Al_{0.15}Ga_{0.85}As$	124nm	NID[v]
$In_{0.1}Ga_{0.9}As$	10nm	NID
$Al_{0.15}Ga_{0.85}As$	124nm	NID
$Al_{0.3}Ga_{0.7}As$	2.5μm	N $3 \cdot 10^{17}$ cm^{-3}
GaAs	400nm	N+ 10^{18} cm^{-3}

Table 9.1: Basic structure of a non-tunable single quantum well, separate confinement heterostructure laser

The top layers are P-type doped to provide holes into the active area whereas the bottom layers (as well as the substrate) are N-type doped to provide electrons. This is a typical semiconductor laser diode structure. The emission wavelength, which is fixed for this structure, corresponds to the gain maximum exhibited by the $In_{0.1}Ga_{0.9}As$ quantum well.

Section:9.2. Establishing an electric field

The structure presented in Fig.9.1 when under equilibrium, exhibits an electric field. This is the result of the doping on the p and n areas. However, as soon as current is injected through the device, the built in electric field of the diode is screened. In fact, the band structure under operation

v Non Intentionally Doped : Background doping of the MBE growth system is n type 10^{14} cm^{-3}

resembles the flat band situation shown. It is clear that a different way to establish an electric field inside the diode has to be devised.

Carrier transport is governed by drift (due to electric fields) and diffusion (due to concentration gradients). Drift tends to cancel out existing electric fields and diffusion tends to cancel out existing carrier concentration gradients. In fact, carrier concentration gradients and electric fields are connected through the Poisson equation. One way to establish an electric field would be to inhibit carrier movement. This way, free carriers would be unable to drift and diffuse thus allowing for electric fields to be established.

Acting much like a capacitor, where carriers of the opposite charge concentrate on the plates one could devise a way to collect carriers of opposite charge (electrons and holes) in a semiconductor structure. That would result in an electric field. A simple way to create an obstacle to carrier movement is to place a thin layer of higher band gap semiconductor in their path. The heterostructure formed exhibits a discontinuity in the band gap. Thus, carriers traveling in the band, face a barrier that stops them from freely moving further. This will cause an accumulation of carriers (i.e. charges) before the barrier. Putting two such barriers on each side of the active quantum well would result in electrons being accumulated on one side (negative charge) and holes (positive charge) on the other. In order for the laser to work, both type of carriers need to eventually reach the active quantum well.

There are two mechanisms for a carrier to traverse the barrier and inject into the active quantum well. First there is thermal overshoot. Statistically a small portion of the carriers facing the barrier will obtain thermal energy that matches the height of the barrier. Those carriers may go over the barrier and into the rest of the structure. This mechanism is expected to be temperature sensitive. The second way for carriers to escape towards the active quantum well is tunneling through the potential barrier. This becomes increasingly possible if the barrier is sufficiently thin. Tunneling probability depends on the barrier characteristics such as potential height, thickness as well as carrier energy. A theoretical approach to estimate tunneling times will be presented later on.

Section:9.3. Tunable structure

Taking advantage of the barrier concept discussed, we may create the structure shown in Fig.9.2.

Under equilibrium, the difference of this structure compared to the basic structure already presented is the two extra layers on each side of the active QW. A barrier is formed using $Al_xGa_{1-x}As$ which is a high bandgap material and a GaAs quantum well is placed directly before the barrier. The purpose of the GaAs quantum wells will be discussed when presenting the experimental results.

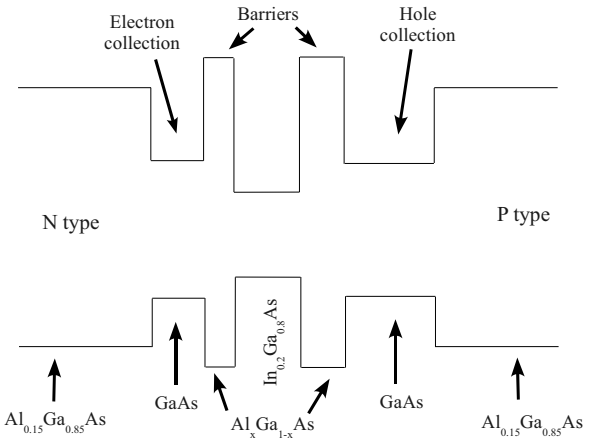

Figure 9.2.:Schematic of the structure proposed to establish an electric field. Structure in equilibrium (The PN built in electric field is also ignored). To avoid cluttering the image, only the core of the structure is shown, the rest remains unchanged.

As soon as current is injected into the structure, the situation changes drastically. Instead of the carriers being injected into the active quantum well, they accumulate into the GaAs quantum wells (**collection quantum wells**) just outside the barriers. Fig. 9.3 shows a schematic of the expected carrier movement. Finally, given time, those carriers will tunnel into the active quantum well and recombine producing photons. Depending on the thickness and height of the barriers, at a given time, a percentage of injected electrons and holes will reside in the collection QW's. This will provide an electric field across the active QW. In turn the electric field will modify the emission of the active QW according to the quantum confined stark effect.

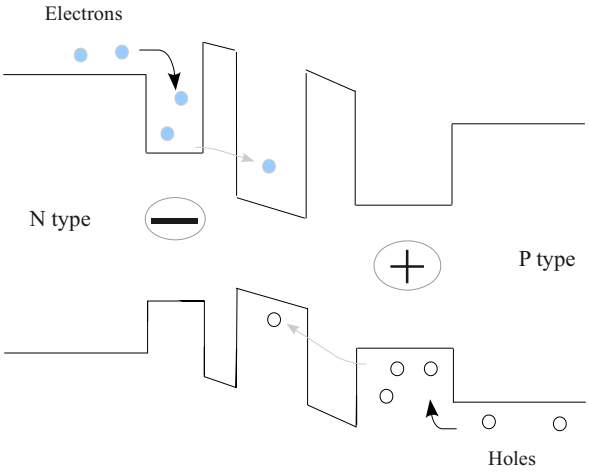

Figure 9.3.:Schematic of the tunable structure under injection. Electrons and holes are accumulated in the GaAs areas directly outside the barriers causing an electric field. As a result the active quantum well is bended, exhibiting a quantum confined stark effect thus tuning the emission spectra.

Depending on the pump current, the accumulated number of the charges in the collection wells will vary. This will translate to a different electric field thus a different magnitude of the stark effect. This device is expected to tune its emission by varying the pump current.

Changing the thickness and height of the barriers, the number of charges accumulated outside the active area for a given current is expected to vary accordingly. This will result in different magnitude of the electric field, thus stark effect for a given current density.

It is evident that a very thick barrier, would result in a small amount of carriers tunneling into the $In_{0.1}Ga_{0.9}As$ quantum well. That, in turn, would provide reduced gain for the laser diode to work and very large electric field build up at small injection current. On the contrary, a very thin barrier would not allow enough carriers to collect in the accumulation quantum wells. That would diminish the electric field created. Table 9.2 shows the layers of the proposed structure. As discussed, barrier mole fraction (i.e. height) as well as thickness are to be finalized during this work.

Material	*Thickness*	*Doping*
GaAs	250nm	P+ 10^{18} cm^{-3}
$Al_{0.3}Ga_{0.7}As$	1.6μm	P 10^{17} cm^{-3}
$Al_{0.15}Ga_{0.85}As$	124nm	NID
GaAs	20nm	NID
$Al_xGa_{1-x}As$	To be examined	NID
$In_{0.1}Ga_{0.9}As$	10nm	NID
$Al_xGa_{1-x}As$	To be examined	NID
GaAs	4.5nm	NID
$Al_{0.15}Ga_{0.85}As$	124nm	NID
$Al_{0.3}Ga_{0.7}As$	2.5μm	N $3\cdot10^{17}$ cm^{-3}
GaAs	400nm	N+ 10^{18} cm^{-3}

Table 9.2: Proposed structure for a tunable single quantum well, separate confinement heterostructure laser

A final note regarding thermal stability of the design. As already discussed, carriers may thermally overshoot the barriers. This process however being strongly thermally sensitive is undesirable, it is thus necessary to tune the barrier height so as to provide room temperature operation of the concept.

Chapter 10.Modeling of used laser diode structures

Understanding the behavior of the laser devices presented in this work, necessitates a careful approach of the theoretical background. This chapter provides the semiconductor theory necessary to follow the mechanisms involved in tunable laser device behavior.

The first section presents semiconductor band structure theory which is necessary to be able to predict carrier distribution and band line up inside a laser structure, then follows light interaction with the structure, waveguiding and gain computation theory. Finally in section 3 tunneling is addressed since it is a main part of the concept of this work.

Section:10.1. Semiconductor Band structure

In order to model and understand any of the semiconductor behavior, there is a need to model the band structure where carriers reside. The ideas presented are based on the k·p method, initially introduced by Bardeen [68] and Seitz [69]. This section will briefly describe some available options and comment the associated approximations.

10.1.1 Semiconductor Bandgap

Maybe the most important characteristic of a semiconductor is the existence of an energy bandgap. Which is an energy range for which there are no solutions to the E(k) relation. An intrinsic (pure), perfectly formed semiconductor would have no free carriers at 0K. In reality, semiconductor behavior becomes interesting because of doping which readily provides carriers as well as our ability to engineer the bandgap as already discussed.

Temperature Dependence

Varshni developed an empirical formula describing the bandgap dependence of a semiconductor with temperature. This is given by the following equation:

$$E_g(T) = E_{go} - \frac{A \cdot T^2}{T + B} \tag{10.1}$$

where A and B are the Varshni coefficients. These parameters along with the bandgap at zero temperature E_{go} are enough to calculate the bandgap of a low doped semiconductor at any given temperature.

Material	*Bandgap at 0 Kelvin*	*A*	*B*
GaAs	1.519	$5.405\ 10^{-4}$	204
AlAs	2.239	$6.0\ 10^{-4}$	408
InAs	0.420	$2.50\ 10^{-4}$	75

Table 10.1: Some basic III-As compounds and the respective Varshni coefficients. Reprinted from [70]

Besides the issue of temperature dependence of the bandgap which has been addressed, there are also several effects that change a semiconductor bandgap. For example when carrier concentration increases, the free carriers screen the atomic potentials leading to bandgap renormalization. Such effects will not be addressed within this text.

Semiconductor alloys

One of the most powerful features of compound semiconductors is the ability to mix atoms from the III and/or the V column of the periodic table to make alloys such as $Al_xGa_{1-x}As$ or $GaAs_xP_{1-x}$. In such cases the alloy will have properties in between the properties of its constituents.

Most properties are given by the weighted average of the respective values that the binary compounds have.

The most striking exception is the bandgap of an alloy which is described by a non-linear relationship. The factor of the nonlinearity is called bowing and is necessary to accurately predict alloy bandgap. Furthermore effective masses which will be described in the following section are interpolated as the inverse of the weighted average of the reciprocal of the effective masses of the constituent compounds.

10.1.2 Effective mass approximation

Besides the bandgap, it is necessary to obtain a picture of how the free carriers behave inside the respective bands. The simpler approach available is the effective mass approximation.

In the framework of the effective mass approximation, it is assumed that each band (electrons, heavy holes, light holes and SO band) has a parabolic dispersion relation, described by the associated effective mass and the band edge (energy at k=0). Therefore the energy dispersion relation is given by the simple equation $$E = \frac{\hbar^2 \cdot k^2}{2 \cdot m^*} \tag{10.2}$$

In essence, it is assumed that each carrier is traveling in free space and the entire semiconductor medium only manifests its presence in a change of the mass which the carrier appears to have (thus the term effective mass).

In the effective mass picture it is easy to obtain analytical relations for the Density of states (DOS) for n-dimensional system where n = 0 - 3.

$$DOS_{3D}=\frac{1}{2\pi^2}\left(\frac{2m^*}{\hbar^2}\right)^{3/2}(E-E_c)^{1/2} \tag{10.3}$$

$$DOS_{2D}=\frac{m^*}{\pi\hbar^2}\sum_n U(E-E_b^n) \tag{10.4}$$

$$DOS_{1D}=\sqrt{\frac{2m^*}{\pi^2\hbar^2}}\sum_n \frac{n_i U\left(E-E_b^n\right)}{E-E_b^n} \tag{10.5}$$

Quantum dots necessitate a different approach. The physics of the Quantum dots (0 dimensional DOS) predicts a delta like function density of states for each eigenenergy. However dots are dispersed in size. This leads to a dispersion of the eigenenergy level for each dot. In order to be able to model a quantum dot system correctly one has to take this into account, thus the DOS function resembles a Gaussian curve around the average size i.e. the dominant energy state. In reality the function is not that simple, and depends on size statistics of a large ensemble of dots.

U(x) is the heavy side step function. Eq.10.3 through 10.5 hold for electrons. With minor sign changes however they may be applied for holes as well. The main advantage of the effective mass approximation is the fact that governing equations are easy to solve. This allows for a fast yet fair description of the semiconductor band structure.

However, as already said, this is only an approximation. The accuracy of this model is compromised as soon as higher energy (i.e. k) components are populated. The bands in that regime are strongly non-parabolic. For systems with low carrier density and low temperature, the effective mass model may be very close to the reality, but for high carrier density and/or elevated temperature systems, this is a poor approximation to work with. The major difference comes from valence band states (hole distribution). Since these bands are close together (heavy hole, light hole and SO band), they interact leading to band mixing. A more precise model needs to be implemented for these bands. This will be addressed in the next section.

From a different perspective, the effective mass model is nothing short of the linearization of the solution of the Bloch equations in the periodic semiconductor potential [71]. The bands in which carriers live are to first approximation parabolic, it is only the requirements of this work, and laser diodes in general for a precise description that clarifies that make it a poor approximation to follow.

10.1.3 Kohn-Luttinger model

The Kohn Luttinger model is based on the same principles as the effective mass theory. However in this case, the coupling between the bands is not neglected leading to a much more accurate description. Taking into consideration the valence bands (heavy hole, light hole and SO band, all doubly degenerate due to spin) the Hamiltonian of the system may be expressed as:

$$\overline{\overline{H}}^{LK}=\begin{bmatrix} P+Q & -S & R & 0 & -S/\sqrt{2} & \sqrt{2}R \\ -S^{+} & P-Q & 0 & R & -\sqrt{2}Q & \sqrt{3/2}S \\ R^{+} & 0 & P-Q & S & \sqrt{3/2}S^{+} & \sqrt{2}Q \\ 0 & R^{+} & S^{+} & P+Q & -\sqrt{2}R^{+} & -S^{+}/\sqrt{2} \\ -S^{+}/\sqrt{2} & -\sqrt{2}Q^{+} & \sqrt{3/2}S & -\sqrt{2}R & P+\Delta & 0 \\ \sqrt{2}R^{+} & \sqrt{3/2}S^{+} & \sqrt{2}Q+ & -S/\sqrt{2} & 0 & P+\Delta \end{bmatrix} \tag{10.6}$$

where $$P=\frac{\hbar^2\gamma_1}{2m_o}\left(k_x^2+k_y^2+k_z^2\right) \tag{10.7}$$

$$Q=\frac{\hbar^2\gamma_2}{2m_o}\left(k_x^2+k_y^2-2k_z^2\right) \tag{10.8}$$

$$R=\frac{\hbar^2}{2m_o}\left[-\sqrt{3}\gamma_2\left(k_x^2+k_y^2\right)+i\,2\sqrt{3}\gamma_3 k_x k_y\right) \tag{10.9}$$

$$S=\frac{\hbar^2\gamma_3}{m_o}\sqrt{3}\left(k_x-ik_y\right)k_z \tag{10.10}$$

Where γ_i are the Luttinger constants, defined experimentally for each material. Note that expanding the KL model to include the conduction bands as well, would lead to an 8x8 Hamiltonian. Including the conduction band is necessary in case a narrow bandgap semiconductor is to be modeled. In our case (E_g >1eV), this is not necessary and the conduction band – valence band coupling can be neglected.

10.1.4 Strain related corrections

Contemporary devices, routinely use strained layers, thus the need to model strain effects in a semiconductor layer is obvious. Strained layers are utilized in both electronic devices such as transistors (HEMT) as well as optoelectronic devices (long-wavelength detectors and laser diodes). In semiconductor devices the most common way to strain a layer is to pseudomorphicaly grow on a substrate with slightly different lattice constant. The periodicity is still maintained but the period is now imposed by the substrate and not the layers' inherent properties. This leads to significant modification of the layer's electronic characteristics behavior. The stress applied in a crystal is a tensor τ_{ij} with diagonal elements corresponding to pressure along an axis (making the crystal deform along that axis but remain rectangular in shape), whereas the off-diagonal components correspond to shear stress and will make the crystal deform side-wise. In biaxial strained layers, we only have diagonal elements of stress. The same facts apply for the deformation of a crystal as a result of stress. The deformation tensor or strain tensor is depicted as ε_{ij} and depicts the fractional increase ($\varepsilon_{ij} > 0$) or decrease ($\varepsilon_{ij} <0$) of the crystal lattice. Diagonal elements of strain define the deformation of the crystal along an axis.

Since torque has to be zero everywhere, off-diagonal elements of both strain and stress follow

the rule that $\tau_{ij} = \tau_{ji}$ thus letting us compact the tensors of stress and strain into a column vector like the one shown in eq.10.11. Stress and strain are connected through the elastic stiffness moduli $C_{ij.}$

Limiting our discussion to cubic crystals, we have

$$\begin{bmatrix} \tau_{xx} \\ \tau_{yy} \\ \tau_{zz} \\ \tau_{xy} \\ \tau_{yz} \\ \tau_{zx} \end{bmatrix} = \begin{bmatrix} C_{11} & C_{12} & C_{12} & 0 & 0 & 0 \\ C_{12} & C_{11} & C_{12} & 0 & 0 & 0 \\ C_{12} & C_{12} & C_{11} & 0 & 0 & 0 \\ 0 & 0 & 0 & C_{44} & 0 & 0 \\ 0 & 0 & 0 & 0 & C_{44} & 0 \\ 0 & 0 & 0 & 0 & 0 & C_{44} \end{bmatrix} \begin{bmatrix} \varepsilon_{xx} \\ \varepsilon_{yy} \\ \varepsilon_{zz} \\ \varepsilon_{xy} \\ \varepsilon_{yz} \\ \varepsilon_{zx} \end{bmatrix} \tag{10.11}$$

In order to model the strain effects in the Kohn Luttinger Hamiltonian, Pikus and Bir [72],[73] came up with the Pikus-Birr Hamiltonian H_{PB}. The pertrubation terms that have to be added to KL theory are shown in the following equations (eq.10.7 - 10.10).

$$P_{\varepsilon} = -\alpha_u \left(\varepsilon_{xx} + \varepsilon_{yy} + \varepsilon_{zz} \right) \tag{10.12}$$

$$Q_{\varepsilon} = \frac{-b}{2} \left(\varepsilon_{xx} + \varepsilon_{yy} - 2\,\varepsilon_{zz} \right) \tag{10.13}$$

$$R_{\varepsilon} = \frac{\sqrt{3}}{2} b \left(\varepsilon_{xx} - \varepsilon_{yy} \right) - i\,d\,\varepsilon_{xy} \tag{10.14}$$

$$S_{\varepsilon} = -d \left(\varepsilon_{xx} - i\,\varepsilon_{yz} \right) \tag{10.15}$$

where ε_{ii} are the strain tensor components.

For example, in the (100) orientation and in case of biaxial strain, we have:

$$\varepsilon_{xx} = \varepsilon_{yy} = \frac{a_o - a}{a} \tag{10.16}$$

$$\varepsilon_{zz} = \frac{-2\,C_{12}}{C_{11}} \varepsilon_{xx} \tag{10.17}$$

where a_o and a are the native lattice constants of the substrate and the strained layer material respectively and C_{ii} are the elastic stiffness constants.

The following table shows the parameters regarding strained layer formalism described here.

Parameter	*GaAs*	*InAs*	*AlAs*[vi]
α_o (Å)	5.6533	6.0584	5.6600
E_g (eV)	1.519	0.418	3.044
γ_1	6.85	20.4	3.45
γ_2	2.1	8.3	0.68
γ_3	2.9	9.1	1.29
C_{11} (dyn/cm^2)	11.879	8.329	12.5
C_{12} (dyn/cm^2)	5.376	4.526	5.34
$\alpha=\alpha_c - \alpha_v$ (eV)	-9.77	-6.0	-7
b (eV)	-1.7	-1.8	-1.7
m^*_e	0.067	0.025	0.15

Table 10.2: Parameters for some Basic III-As compound semiconductors. Collected from literature

Finally, although the formalism presented follows the KL Hamiltonian one may expand the energy relation for each sub-band up to second order terms. This way we may obtain a modified effective mass usable in the effective mass approximation. [74] This facilitates the use of the effective mass theory in case of strained layers as well.

It should be stressed that the 6x6 Kohn Luttinger and Pikus Birr Hamiltonians are still an approximation. They do however take into account higher order effects in the crystal leading to a description that is fairly accurate for the majority of electronic bandstructure analysis. In case of low band gap semiconductors, the conduction – valence band energy distance becomes smaller. In this case coupling of conduction to valence band becomes important. To describe this effect the 8x8 kp Hamiltonian has to be used. [75] [76]

10.1.5 Effects of orientation

The formalism presented in the previous section may be used as is for (001) oriented structures. It is often the case however to look into semiconductor structures grown on different orientations. In fact as we will describe later on, part of this work is based on the unique characteristics that are obtained when structures are grown on high index surfaces such as (111). In order to extend the Kohn Luttinger Hamiltonian model to an arbitrary orientation we need to take into account the associated crystal rotation. Thus we need to apply a unitary rotation transformation of the k space which has the form:

$$U=\begin{pmatrix} cos\varphi\cos\theta & \sin\varphi\cos\theta & -\sin\theta \\ -\sin\varphi & \cos\varphi & 0 \\ \cos\varphi\sin\theta & \sin\varphi\sin\theta & \cos\theta \end{pmatrix} \tag{10.18}$$

where φ and θ are the azimuthal and polar angles of the [hkl] orientation relative to the [100] orientation. A similar transformation was implemented by R.H.Henderson [77] for the 4x4 Hamiltonian.

10.1.6 Polar structures and piezoelectric effects

III-V compound semiconductors are grown in the zinc-blend structure. The zinc blend structure

vi AlAs constants are not for actual AlAs material. Some are tuned to produce correct results when used in ternary compound calculation. i.e. $Al_xGa_{1-x}As$. Keep in mind this alloy is indirect when x> 0.4.

although symmetric along the 100 direction, lacks inversion symmetry along the 111 direction. Thus, any distortion along this axis will result in a net dipole along the very same axis. The magnitude of the polarization obviously depends on the extent of the distortion. In case of biaxial stress, this translates to lattice mismatch between the pseudomorphicaly grown layer and the host material. According to [78], for 111-oriented growth, the magnitude of the polarization is:

$$P_i^S = 2\, e_{14}\, \varepsilon_{jk} \tag{10.19}$$

where e_{14} is the only nonzero piezoelectric constant for zinc-blend crystals and ε_{jk} is the symmetrized strain component see [79] regarding the factor of 2 in eq.10.19. The polarization and the associated electric field are readily connected using $E_z = -\frac{P}{\varepsilon_s \varepsilon_o}$ (10.20)

where ε_s is the relative permittivity and ε_o is the vacuum permittivity. For a detailed description of the strain induced polarization in 111 InGaAs/GaAs QWs see [80] and [81].

As far as the direction of the generated electric field is concerned, it is toward the substrate for a compressively strained layer and (111)B polarity substrate.

Finally, for a given strain, the polarization field is maximum for 111-oriented heterostructures and diminishes for other orientations up to the point where it cancels out for the 100 orientation.

As we will clarify in the following paragraph, electric fields and charge build up inside the structure are directly linked to band bending which in turn leads to band structure modification.

10.1.7 Band bending – Poisson equation

So far the theory that allows us to predict the energy distribution of charges inside the energy bands of a given semiconductor structure was presented. However any charge build up translates to an electric field. In order to compute the structure alignment in the presence of charges, it is necessary to solve the Poisson equation taking into account all charges (ionized dopants and free carriers) as well as any electric field present in the structure i.e. piezoelectricity effects. The Poisson equation in one dimension is given by:

$$\frac{\partial}{\partial x}\left[\varepsilon_s(x)\frac{\partial}{\partial x}V(x)\right] = \frac{-q}{\varepsilon_o}\rho(x) \tag{10.21}$$

where V(x) is the potential profile and ρ(x) is the charge distribution inside the structure.

10.1.8 Schroedinger Equation

Control of the semiconductor structure growth has enabled layer fabrication with thickness small enough to obtain quantum mechanical behavior. In order to describe such layers, the Schroedinger equation has to be implemented. Given the band profile and the Hamiltonian describing the system, solutions of the Schroedinger equation are obtained along the growth axis. It is assumed that the characteristic dimensions of the device parallel to the growth plane are always large enough to treat all layers as bulk.

The general form of the Schroedinger equation is given by:

$$(H+V)\Psi_n = E_n \Psi_n \tag{10.22}$$

where H is the system's Hamiltonian and E_n,Ψ_n is the n^{th} eigenenergy and eigenvector respectively which satisfies eq.10.22. Keep in mind that to apply this equation the wave vector *k* is replaced by the differential operator $-i\nabla$ .Thus, for the effective mass case in a one dimensional problem we have:

$$-\frac{\hbar^2}{2}\frac{\partial}{\partial x}\left(\frac{1}{m^*}\frac{\partial \Psi(x)}{\partial x}\right)+V(x)\Psi(x)=E\,\Psi(x) \tag{10.23}$$

It should be noted that this is an envelope function approach. The actual solution of the problem is split in two parts, the Bloch eigenfunctions u and the envelope eigenfunctions Ψ. Eq.10.23 deals only with the latter.

10.1.9 Heterostructures – Band line up

When growing different semiconductor materials in contact, the difference in the bandgap is accommodated by a discontinuity either in the conduction band or the valence band or both. Early attempts by Anderson[82] and Tersoff [83] who proposed the "Electron affinity rule" and the "Common Anion rule" respectively to predict the band lineup resulted in poor results. The best results are accomplished by experimental measurements for each heterostructure system. A representative publication is [84].

10.1.10 Summary

In this section the basic tools to theoretically describe the electronic structure of a semiconductor heterostructure have been presented. The way to obtain alloy properties and bandgap at any temperature has been presented. Electrons are modeled using the effective mass approximation whereas hole bands are modeled using the 6x6 Kohn-Luttinger Hamiltonian. Furthermore, the strain effects are included using the Pikus-Birr formalism and piezoelectric effects are included when dealing with polar oriented structures.

This enables us to obtain a reasonable approximation of the density of states and the conduction and valence band profile of the structure under investigation given some initial parameters. The next section will provide the link between the electronic and the optical characteristics of the structure under investigation.

It has to be stated that all equations presented are time independent and do not include dynamic phenomena.

Section:10.2.Light matter interaction

Now that a brief introduction to the theory of electronic structure has been achieved, it is necessary to obtain a description of light interaction with the semiconductor structure. In the following paragraphs, waveguiding, light emission and absorption and gain will be presented from a theoretical point of view. This section will enable us to predict the optical behavior of a given structure based on the detailed electronic description of the previous section

10.2.1 Wave-guiding, Maxwell's equations

Light is electromagnetic radiation. As such it obeys to the general Maxwell's equations:

$$\nabla \cdot B = 0 \tag{10.24}$$

$$\nabla \cdot D = \rho \tag{10.25}$$

with $D = \varepsilon_s \varepsilon_o E$ (10.26)

$$\nabla \times E = -\frac{\partial B}{\partial t} \tag{10.27}$$

$$\nabla \times H = J + \frac{\partial D}{\partial t} \tag{10.28}$$

and $B = \mu H$ (10.29)

Finally the continuity equation: $\nabla \cdot J = -\frac{\partial \rho}{\partial t}$ (10.30)

which provides the link between the Current denisty (J) and the charge density (ρ).

For the semiconductor and dielectric materials which may comprise a real device, $\mu \approx \mu_o$ which is the magnetic susceptibility of vacuum.

Assuming a wave-like solution to the Maxwell's equations and making the slowly varying field amplitude approximation (dropping all double derivatives and products of derivatives) we obtain:

$$\nabla^2 E + \omega^2 \mu \varepsilon_o \varepsilon_s E = 0 \tag{10.31}$$

and $\nabla^2 H + \omega^2 \mu \varepsilon_o \varepsilon_s H = 0$ (10.32)

where the quantity ω is the frequency of the propagating light. Eq.10.31 corresponds to the TE modes and eq.10.32 to the TM modes of the system.

Effective refractive index technique

The edge emitting cavity is a three dimensional problem to solve using equations 10.31 and 10.32. However a three dimensional solution of these equations is a complex task. In fact, there is a much simpler approach which though an approximation leads to very good results.

Initially, the axis parallel to the growth axis is the one that has the smaller features. Semiconductor layers are usually less than a μm thick. Rewriting the wave equations in one dimension we get:

TE mode: $\frac{\partial^2}{\partial x^2} E_y + k_o^2 (\varepsilon_s - n_{eff}^2) E_y = 0$ (10.33)

TM mode: $\frac{\partial^2}{\partial x^2} H_y + k_o^2 (\varepsilon_s - n_{eff}^2) H_y = 0$ (10.34)

where in both: $k_o = \omega \sqrt{\varepsilon_o \mu_o}$ (10.35)

Where y is the direction of propagation and x is the growth direction i.e. the waveguide layers are perpendicular to the x axis.

For a detailed view of the mathematics towards eq.10.33 and 10.34 see [85].

This will provide the effective refractive index of the mode. Solving this equation both on ridge as well as off-ridge we may obtain the effective index profile perpendicular to the cavity.

Now reapplying the same set of equations but this time for the axis we just calculated the refractive index profile, we may obtain the lateral modes of the entire cross section. This will in turn provide a new set of effective refractive indices corresponding two the solutions of the two dimensional waveguide system.

The remaining task is to use the information of the refractive index of each mode to obtain the longitudinal modes by solving the round trip phase equation inside the cavity.

This technique although an approximation decouples the 3 dimensional equation into a set of one dimensional problems. beginning only with the topology of the device and the refractive index information for each layer, the complete optical waveguiding problem is solved. In the next paragraphs we will see how light is interacts with these modes.

A final note on waveguide simulation is in order. Dynamic effects may be included in this theory. The dielectric constant of the semiconductor medium may be altered by carrier or thermal effects. In order to do this, the waveguide analysis has to be self consistently solved along with the electronic structure.

10.2.2 Gain

Departing from Maxwell's equations again but this time keeping the polarization term, we obtain the equation describing light – semiconductor interaction. [86]

If we assume a plane wave traveling inside the semiconductor of the form:

$$E(z,t)=\frac{1}{2}\vec{e}_x E(z)e^{i(kz-\omega t-\varphi(z))} \; with \; k=\frac{\omega n}{c} \tag{10.36}$$

then we have:

$$\frac{dE}{dz}=-\frac{\omega n}{2c}\chi''(z)\cdot E(z) \tag{10.37}$$

$$\frac{d\Phi(z)}{dz}=-\frac{\omega n}{2c}\chi'(z) \tag{10.38}$$

where $\chi(z)=\chi'+i\chi''$ is the complex susceptibility of the material. From eq. 10.37 we obtain the change in amplitude change of the field i.e. the gain of the material. In terms of intensity gain we finally have:

$$G=-\frac{\omega n}{c}\chi''(z) \tag{10.39}$$

The susceptibility of the material may be computed from the electronic properties we have calculated in the previous section. In the following paragraphs the method to perform such a calculation will be presented.

Depending on the degree of simplifications done on the interaction Hamiltonian of the system, we may obtain three levels of accuracy.

The full Hamiltonian describing light-semiconductor interaction may be written as:

$$H=\sum_k (E_{go}+E_{ek})\,a_k^\dagger a_k+E_{hk}\,b_{-k}^\dagger b_{-k}$$
$$+\frac{1}{2}\sum_{kk'}\sum_{q\neq 0} V_q(a_{k+q}^\dagger a_{k'-q}^\dagger a_{k'}a_k+b_{k+q}^\dagger b_{k'-q}^\dagger b_{k'}b_k-2a_{k+q}^\dagger b_{k'-q}^\dagger b_{k'}a_k) \quad (10.40)$$
$$-\sum(\mu_k a_k^\dagger b_{-k}^\dagger+\mu_k^* b_{-k}a_k)\,E(z,t)$$

where E_{go} is the bandgap energy, E_{ek} is the conduction band energy corresponding to k, E_{hk} is the valence band energy for the same k, V_q is the Fourier transform of the Coulomb potential, and finally the operators a and b are:

a : Electron annihilation operator

a† : Electron creation operator

b : hole annihilation operator

b† : hole creation operator

Eq.10.40 is sectioned in three lines. The first line corresponds to the photon energy $E_{go}+E_e(k)+E_h(k)$. The second line corresponds to Coulomb interactions, inside the double sum there are three terms, the first two are electron and hole intra-band interactions, respectively. The last term is electron hole interactions. Finally the third line is the light field – carrier interaction.

The only term not described so far is μ_k which is the dipole matrix element defined as:

$$\mu_k=\langle\Psi_e(r)|r|\Psi_v(r) \quad (10.41)$$

where Ψ contains not only the envelope but the entire wavefunction including the Bloch solutions.

Depending on which parts of the Light – Matter Hamiltonian we take into account we can end up with three different levels of accuracy.

Free carrier theory

In this case all interacting terms of eq.10.40 are neglected. Assuming a dephasing time γ we finally obtain:

$$G(\omega)=\Im\left(\frac{i\omega}{\hbar c\,\varepsilon_o n_{opt}}\frac{1}{V}\sum_{n,m}\sum_{\sigma}\int_0^\infty dk\,k\,|\mu_\kappa^{nm,\sigma}|^2(f_{ek}^n+f_{hk}^m-1)\frac{\gamma}{(\omega_k^{nm}-\omega)^2+\gamma^2}\right) \quad (10.42)$$

where n and m are the conduction and hole bands respectively and σ is the summation over each subband (light, heavy holes).

Although this model does provide some level of insight, it suffers from a number of issues. To begin with, this model predicts absorption below the band gap. This is a consequence of the broadening induced by the dephasing. Furthermore, since no coulomb interaction effects were taken into account, there is no gain enhancement, band gap renormalization nor any excitonic effects.

On the other hand, although this model lacks the refinement of a full calculation it imposes a fast way to obtain gain information from the band calculations done in the previous section.

Screened Hartree-Fock approximation

Taking into account carrier screening, the following problem arises: The two particle interaction operators are coupled to the four particle interaction operators and so on. In the screened Hartree-Fock approximation (sHF) only second order terms are treated. Higher order terms are factored out. The procedure is analytically described in [87]. The two extra phenomena described using this approximation is band gap renormalization and coulomb enhancement of gain. The corresponding gain is calculated using:

$$G(\omega)=\Im\left(\frac{i\omega}{\hbar c\,\varepsilon_o n_{opt}\pi L_z}\frac{1}{V}\sum_{n,m}\sum_{\sigma}\int_0^{\infty} dk\,k\,|\mu_{\kappa}^{nm,\sigma}|^2\frac{(f_{ek}^{n}+f_{hk}^{m}-1)}{i(\omega'_k-\omega)+\gamma}Q_k^{nm}(\omega)\right) \tag{10.43}$$

where

$$\hbar\omega_k^{'}=\hbar\omega_k+\Delta E_{CH}+E_{SX,k} \tag{10.44}$$

provides the ω'_k the two terms ΔE_{CH} and $E_{SX,k}$ are the Debye shift and the exchange shift. In Appendix Ap. provides the equations needed to estimate those for a given structure.

Finally the term $Q_k^{nm}(\omega)$ is the Coulomb enhancement factor which describes the gain enhancement due to many body effects.

Full gain model

In this model, not only screening effects but also particle collisions are also taken into account. In this model carrier – carrier scattering and coulomb interaction is fully described. Thus the Fermi distributions are no longer a prerequisite. They naturally emerge through the governing equations. Furthermore, excitonic effects now emerge in the absorption spectra through electron-hole interaction which are correctly described.

The gain spectra is given by:

$$G(\omega)=\Im\left(\frac{i\omega}{\hbar c\,\varepsilon_o n_{opt}\pi L_z}\frac{1}{V}\sum_{n,m}\sum_{\sigma}\int_0^{\infty} dk\,k\,|\mu_{\kappa}^{nm,\sigma}|^2\frac{(f_{ek}^{n}+f_{hk}^{m}-1)}{i(\omega'_k-\omega)+\gamma_{kk}}Q_k^{nm}(\omega)\right) \tag{10.45}$$

where the ω'_k is now calculated using:

$$\hbar\omega_k^{'}=E_{ek}+E_{hk}+E_{go}+\Delta E_{SX,k}+\hbar\Delta_{kk} \tag{10.46}$$

It is important to note that γ_{kk} (the dephasing time) is no longer an input but is computed within the framework of the Born approximation. Furthermore, the bandgap renormalization is provided by a different set of equations.

Numerically solving these equations is resource intensive since many integrals have to be evaluated. However, this model will correctly describe most of the features of the experimental gain spectra.

10.2.3 Spontaneous emission

As already discussed, excess carriers in a direct semiconductor, when not devoured by non-radiative phenomena, will recombine emitting photons. Having already thoroughly described gain in 10.2.2, and switching from ω to photon energy (E=ħ2πω) we only need to express spontaneous

emission rate in terms of G(E). Following the rational described in [88] and references therein, we obtain:

$$r_{spont}(E)=\left(\frac{8\pi n_r^2 E^2}{h^3 c^2}\right)\frac{1}{1-e^{[E-(F_2-F_1)]/k_bT}}G(E) \tag{10.47}$$

which readily provides the spontaneous emission as long as the gain is calculated.

10.2.4 Simulations

The mathematics involved in solving the equations of Chapter 10. are rather complicated. In fact, no closed form solutions are possible unless text book cases are investigated. Real life structures need a different approach.

In order to be able to solve the coupled equations presented so far, a computer program was developed. In the following paragraph, the simulation strategy will be described and the key points of the simulation will be presented.

Simulation strategy

As described, the first step is to model the electronic band structure of the material for a given

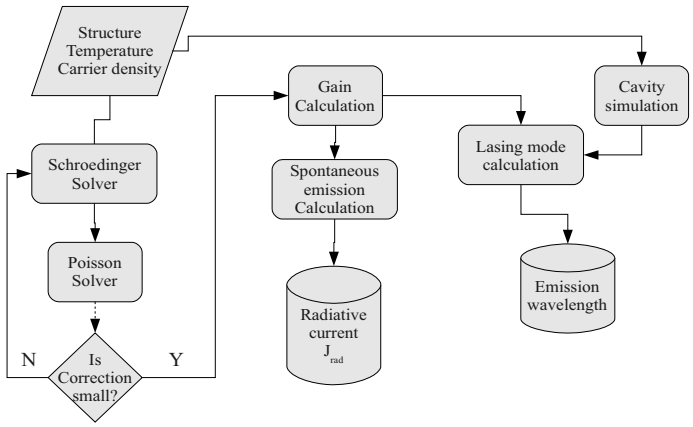

Figure 10.1.: Flowchart of structure simulation.

set of parameters (Temperature and carrier density). This translates into solving the Schroedinger and Poisson equations self consistently. As soon the full band structure is obtained, it is populated by the given carriers (using Fermi statistics) and the gain calculation is performed. Finally from the gain information spontaneous emission may be calculated. Fig. 10.1 shows a schematic representation of the simulation flow chart.

General background

In order to treat real space within a computer program there is a need to create a sampling of the continuous free parameter (space, energy, k e.t.c.) This is called discretized space. Let us work with a spatial example, the dimension x.

The obvious way to perform this is to set a constant step Δx (uniform mesh) thus the continuous dimension will be transformed to a table of values x_i where i can be 1..N and the distance between consecutive x_i is fixed to Δx. N is the number of points, thus the total range of x that may be addressed this way is N·Δx. The problem with this uniform grid is in case there is an increased interest at some area whereas the rest of the range depicts no interesting phenomena. A good example is the axis perpendicular to the growth in a semiconductor structure. The first μm contain all the active layers where the action takes place. The substrate which may be 100μm thick may still be needed (i.e. thermal dissipation, resistance modeling) but has no significant interest. This is why uniform mesh may not be the optimal discretization strategy.

A different approach would be to gradually vary the step Δx with i. This way we choose a dense discretization where interesting phenomena are evolving and a sparse yet existing mesh at the rest of the parameter range. This falls in the category of non-uniform mesh. The price for such a choice is increased complexity as is evident from the following paragraph.

Given the grid discussed, the derivative of a function y over x may be obtained [89] using the following equations:

$$\left.\frac{dy}{dx}\right|_i = \frac{h_+}{h_+ + h_-}\frac{y_+ - y_o}{h_+} + \frac{h_-}{h_+ + h_-}\frac{y_o - y_-}{h_-} \tag{10.48}$$

and the second derivative may be expressed as:

$$\left.\frac{d^2y}{dx^2}\right|_i = \frac{h_- y_+ - (h_+ + h_-)\, y_o + h_+ y_-}{\frac{1}{2} h_+ h_- (h_+ + h_-)} \tag{10.49}$$

where:

$$\begin{aligned} h_- &= x_i - x_{i-1} \\ h_+ &= x_{i+1} - x_i \\ y_- &= y_{i-1} \\ y_o &= y_i \\ y_+ &= y_{i+1} \end{aligned} \tag{10.50}$$

In case the mesh is uniform the above equations simplify into:

$h_-=h_+=\Delta x$ the mesh size.

$$\left.\frac{dy}{dx}\right|_i = \frac{y_+ - y_-}{2\Delta x} \tag{10.51}$$

$$\left.\frac{d^2y}{dx^2}\right|_i = \frac{y_+ - 2y_o + y_-}{\Delta x^2} \tag{10.52}$$

which may be familiar.

As discussed in [89] eq.10.48 weights more the rough side of the mesh. This results in a larger local truncation error but the round-off error which is important in numerical stability is smaller. This is why the choice of using eq.10.48 is done.

10.2.4.1Poisson Solution

So far, sampling and derivative treatment has been presented. Integration follows the notorious trapezoidal algorithm [90] . The remaining part of the computational background lies in transforming differential equations into a form that may be solved by a computer. There are several method to treat a differential equation and each has advantages and disadvantages. For this work the method of choice is **finite differences,** since it is a generic algorithm to treat differential equations. The concept is clarified here for completeness using the Poisson equation (eq.10.21)

Assuming that the exact solution is

$$V_o(x)=V(x)+\delta V(x) \tag{10.53}$$

where V is the current estimate and δV is the error.

This perturbation of V will result in a corresponding change of ρ(χ). Although ρ(x) does not depend linearly on V, we may use a Taylor expansion and keep only terms depending on δV. Thus we have:

$$\rho(x)\big|_{V_o}=\rho(x)\big|_{V}+\frac{\partial\rho(x)}{\partial V}\cdot\delta V \tag{10.54}$$

We use the same technique to obtain changes in other quantities that depend on the main variable.

The target is to estimate $\delta V(x)$ or in discretized notation δV_i. Inserting eq.10.53 and 10.54 into eq.10.21 and rearranging all terms so that the right hand side contains only V terms we have

$$\frac{\partial}{\partial x}\left[\varepsilon_s(x)\frac{\partial}{\partial x}\delta V(x)\right]+\frac{q}{\varepsilon_o}\frac{\partial\rho(x)}{\partial V}\cdot\delta V=-\frac{\partial}{\partial x}\left[\varepsilon_s(x)\frac{\partial}{\partial x}V(x)\right]-\frac{q}{\varepsilon_o}\rho(x) \tag{10.55}$$

We call e(x) the RHS of this and we have:

$$\frac{\partial}{\partial x}\left[\varepsilon_s(x)\frac{\partial}{\partial x}\delta V(x)\right]+\frac{q}{\varepsilon_o}\frac{\partial\rho(x)}{\partial V}\cdot\delta V(x)=e(x) \tag{10.56}$$

Obviously if $V=V_o$ e=0 and this equation has a trivial solution of δV=0. In this case we already have the solution to the differential equation.

If we apply the differentiation operator as depicted in 10.48 twice to obtain the discretized form of the first term, we will end up with terms containing δV_{i-2}, δV_{i-1}, δV_i, δV_{i+1} and δV_{i+2}. Instead we may make the following assumption based on the fact that the dielectric constant ε_s is large in semiconductors and varies little between materials. We may thus ignore the x dependence and move ε_s outside the derivative only in the LHS of equation 10.56. The error is still accurately calculated but eq. 10.56 now simplifies into a second order derivative of δV(x). This may be calculated using only δV_{i-1}, δV_i, δV_{i+1}

$$A_i\delta V_{i-1}+B_i\delta V_i+C_i\delta V_{i+1}=e_i \tag{10.57}$$

Thus equation 10.56 may be written as a set of N linear, coupled equations:

$$\begin{bmatrix} B_1 & C_1 & 0 & 0 & ..... \\ A_2 & B_2 & C_2 & 0 & ... \\ 0 & A_3 & B_3 & C_3 & 0 \\ .... & .... & .... & .... & .... \\ .... & .... & .... & A_N & B_N \end{bmatrix} \cdot \begin{bmatrix} \delta V_1 \\ \delta V_2 \\ \delta V_3 \\ .... \\ \delta V_N \end{bmatrix} = \begin{bmatrix} e_1 \\ e_2 \\ e_3 \\ .... \\ e_N \end{bmatrix} \tag{10.58}$$

this is a set of N equations with N unknowns coupled to each other. A_i, B_i, C_i and e_i are evaluated already thus δV_i may be calculated. The correction is applied to V using eq.10.53.

It should be noted that the coefficient (i.e. A_i, B_i and C_i) matrix in eq.10.58 is tridiagonal. This matrix, may be stored in compact form. Instead of an NxN matrix a 3xN matrix is used. In which the first column contains the sub-diagonal elements, the second the diagonal elements and finally the third contains the upper diagonal.

10.2.4.2Schroedinger Solution

A similar strategy is used to obtain the solution of the Schroedinger equation eq. 10.22. The k_z wave vector is replaced by the differential operator $-i\nabla$. Subsequently all derivatives are replaced using eq. 10.48 and 10.49. Rearranging this we finally obtain:

$$A_i \Psi_{i-1}^n + \left(B_i + V_i - E^n\right)\Psi_i^n + C_i \Psi_{i+1}^n = 0 \tag{10.59}$$

where A_i, B_i, and C_i are the corresponding coefficients. In order for this eq. to have non zero solutions, the determinant of the tridiagonal matrix has to be zero. This is how we obtain the E^n aka the eigenvalues of the system. The method used to find the roots of the determinant is bisection.

Finally, to obtain the corresponding eigenfunctions, inverse iteration is used. For a detailed discussion on those methods, reference [90] is excellent reading.

In case of a multi-band Hamiltonian like the one presented in Section 10.1.3, then eq.10.59 becomes more complicated. If m is the size of the Hamiltonian matrix then the coefficient matrix will be 3m by m·N instead of 3 by N. The increased size corresponds to the band coupling which is accounted for in the latter case. The coefficient matrix is now band diagonal instead of tridiagonal and is stored in compact form in a 3·m by m·N matrix.

A modified bisection algorithm is used to solve for the eigenvalue vectors of size m (each vector has m eigenvalues, one for each band) and inverse iteration is used to get the corresponding eigenfunctions which are still of size N.

In order to obtain the E(k) i.e. the dispersion relation for each band, the eigenvalue problem is solved for each $k_{//}$ of interest. The resulting eigenvalues are stored and used to compute carrier distribution and gain later on.

10.2.4.3Self consistency

The entire procedure is repeated until the error of Poisson equation becomes small. Actually the condition to check for self consistency is the maximum correction δV_{max} calculated by the Poisson solution algorithm. As soon as this is less than 0.1meV it is assumed that the actual band profile is reached. The remaining algorithm is straightforward.

10.2.4.4Gain and spontaneous emission calculation

Once the band structure has been calculated by self-consistently solving Poisson and Schroedinger, the gain requires only a number of integrations to calculate using eq.10.45. Finally spontaneous emission is computed applying eq.10.47 from Section 10.2.3.

10.2.4.5Radiative Current

Assuming that each photon emitted corresponds to an electron – hole pair that is annihilated, it is easy to obtain the total number of carriers that recombine radiatively inside the structure. This is obtained by integrating the spontaneous emission spectra as described in [91] and [92].

10.2.4.6Emission Wavelength

Finally, the gain curve maximum provides the emission wavelength. If one needs to be precise, it is necessary to complete the waveguide simulation for wavelengths in the vicinity of the gain maximum. Subsequently for each supported mode, the modal gain and the threshold condition for this mode is computed. This should provide a set of modes that may reach lasing.

Section:10.3. Dynamic effects

In order to complete a simulation for laser diodes, it is necessary to be able to predict the behavior of the structure under electrical excitation. In this case, the Fermi level for electrons and holes is no longer flat throughout the structure. Furthermore, a different fermi level is used to describe electron population and hole population. These are called pseudo-fermi levels. The pseudofermi levels for each carrier type may be calculated using the drift-diffusion equation which links the current flowing through the structure with the carrier population and the bandstructure.

In case thin semiconductor barriers exist, the drift-diffusion equation needs to take into account tunneling effects. In order to analytically predict carrier traversal through the thin barriers, tunneling probability of carriers needs to be calculated. This section presents the corresponding theory and the solution strategy used to compute these effects.

10.3.1 Tunneling through barriers

Semiclassical tunneling

One of the most powerful techniques in quantum mechanics originates from the Wentzel Kramers Brillouin (WKB) approximation developed as early as 1926. Adopting the method to estimate the tunneling times for an asymmetric double quantum well system is described in [93] and references therein. The following equation describes the tunneling time for electrons:

$$\frac{1}{\tau_T}=\left(\frac{1}{2\mathrm{d}_n}\right)\sqrt{\frac{2E}{m_e^w}}\cdot\frac{16E(V-E)\left(\frac{m_e^b}{m_e^w}\right)}{\left[V+\left(\frac{m_e^b}{m_e^w}-1\right)E\right]^2}\cdot\exp\left(-2\mathrm{d}_b\sqrt{\frac{2\mathrm{m}_e^b}{\hbar^2}(V-E)}\right) \tag{10.60}$$

where d_n is the thickness of the initial QW, d_b denotes the barrier thickness, E is the electron energy, V is the bandgap discontinuity, m^w and m^b are the carrier effective mass in the well and the barrier respectively. This equation may be trivially rewritten for a hole tunneling barrier.

There are several shortcomings to this approximation. Initially it does not take into account the final states, furthermore, it is valid only for thick barriers and large *(V-E)* values. Finally this approximation assumes that all carriers are in k=0 which is not true at high temperature and/or high carrier density.

The WKB based tunneling times has been extended to take into account inplane k momentum and improve the effective tunneling estimates as described in [94]. The difference in tunneling under high excitation/temperature times may reach as much as two order of magnitude.

Bardeen's approach

Using perturbation theory, Bardeen [95] expressed the tunneling probability from an initial state Ψ_i to a final state Ψ_f using the fermi golden rule as:

$$P_{i\to f}=\frac{1}{\tau_T}=\frac{2\pi}{\hbar}\left|\langle\Psi_f\left|M\right|\Psi_i\rangle\right|^2 g(E_f) \tag{10.61}$$

where τ_T is the tunneling time and the interaction is given by:

$$\langle\Psi_f\left|M\right|\Psi_i\rangle=\frac{\hbar^2}{2m}\left[\overline{\Psi_i}\frac{d\Psi_f}{dx}-\psi_f\frac{-d\overline{\Psi_i}}{dx}\right]_{x_o} \tag{10.62}$$

the last equation is evaluated in a point x_o inside the barrier. Under this formulation if we want to look at the time dependent evolution of an initial state Ψ_i which may tunnel out to a final destination described by states Ψ_f^m we obtain:

$$P_{i\to m}(t)=\frac{\left|\langle\Psi_f\left|M\right|\Psi_i\rangle\right|^2}{\hbar^2}\cdot\left[sinC\left(\frac{(E_i-E_m)t}{\hbar}\right)\cdot t\right]^2 \tag{10.63}$$

with $\quad sinC(x)=\sin\frac{(x)}{x}$

based on this idea there are numerous implementations of the transfer matrix formalism. It should be noted that this being a perturbation method, it is only valid in the limit of opaque barriers. Thus the limitation of large tunneling times remains, the difference with the WKB approach is that this is a quantum mechanical approach and as such it inherently takes into account the final states of the problem.

Full time-dependent Schroedinger solution

Only for the sake of completeness we briefly describe this method to calculate tunneling through a barrier. The actual solution to the problem involves solving the time dependent Schroedinger assuming an initial probability of 1 in one state and following the decay of that state with time toward the final states. The eigenvalue problem in this case has complex solutions where

the real part corresponds to the stationary time-independent Schroedinger solution and the imaginary one is directly associated with the state lifetime. Such a picture is well beyond the scope of our work.

Chapter 11.Laser diodes with static electric field

Laser diodes on III-As have traditionally been fabricated on non-polar orientation. For example, the vast majority of GaAs/AlGaAs laser diodes have been studied on (100) GaAs . The main reason for this choice has been the ease of material growth and the resulting material quality. Namely, (100) oriented growth has been extensively investigated and was the orientation of choice during the initial times of laser diode structure growth. There exist however, high index oriented material that exhibit interesting properties. (111) oriented GaAs for example is polar. Pseudomorphic layers grown in this orientation exhibit significant polarization fields. In this chapter, a thorough comparison of laser diodes fabricated on (100) and (111)B orientations is presented. The role of the built-in electric field in the (111)B InGaAs oriented active quantum well is identified and discussed.

Besides the scientific interest of the material presented herein in itself, this chapter can be considered as an introduction to what follows. This is true in the sense that the main part of this work investigates the effect of dynamic electric fields in semiconductor lasers, whereas here the impact of a static electric field is presented.

Section:11.1.Laser performance

In order to compare the effect of crystal orientation on laser diode performance, an identical laser diode structure was grown on GaAs (100) and (111)B oriented substrates. The structure is shown in Table.11.1.

Material	*Thickness*	*Doping*	*Description*
GaAs	250 nm	P+ 10^{18} cm^{-3}	Ohmic contact
$Al_{0.3}Ga_{0.7}As$	1.6 μm	P+ 10^{18} cm^{-3}	Top cladding
$Al_{0.15}Ga_{0.85}As$	125 nm	I	Core
$In_{0.15}Ga_{0.85}As$	10 nm	I	Active
$Al_{0.15}Ga_{0.85}As$	8nm	I	Core
$Al_{0.3}Ga_{0.7}As$	1.6μm	N $3\cdot10^{17}$ cm^{-3}	Bottom cladding
GaAs	-	N+ 10^{18} cm^{-3}	Substrate

Table 11.1: Structure used to study the effect of orientation on laser diode performance.

The samples were used to fabricate edge emitting laser diodes. Processing of the two structures was carried out in parallel, to ensure that no processing related issues affect laser diode performance.

The low temperature spectra emitted from laser diodes in the two configurations, for diodes with identical dimensions, at or below threshold are shown in Fig.11.1. As may be seen, the device grown on (111)B oriented material exhibits a lower threshold compared to (100).

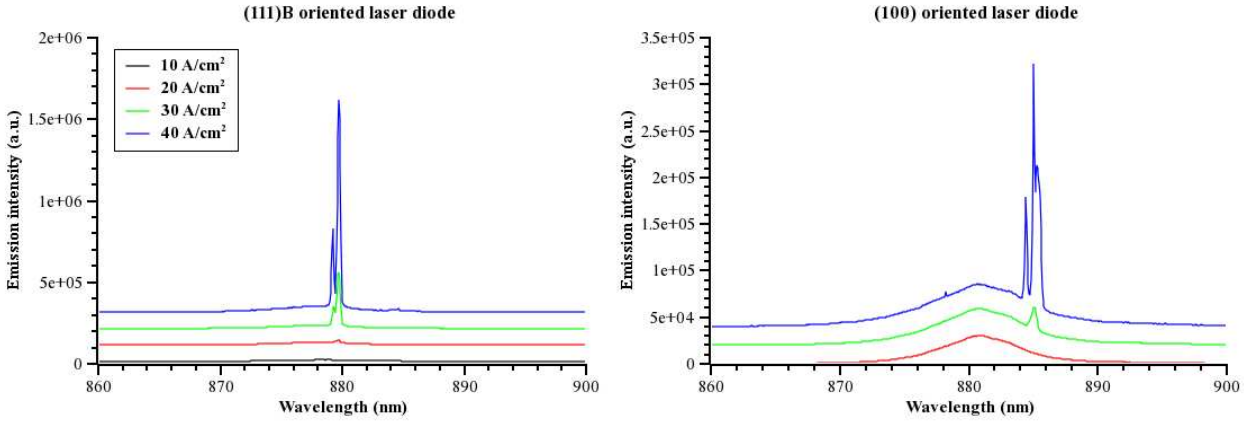

Figure 11.1: Emission spectra at 20Kelvin from a (111)B oriented device (on the left) and a (100) oriented device (on the right). The (111)B oriented device exhibits a lower threshold.

This result is counter-intuitive for the following reasons: initially, one might expect (111)B to have lower crystalline quality compared to (100) grown structures. Furthermore, it is unclear whether there is a residual built-in electric field in the active quantum well during lasing operation, or not. If there is, then the (111)B devices should exhibit a lower electron – hole overlap. To first approximation, this is expected to reduce gain since the latter is proportional to the overlap factor. To elucidate the error in this reasoning, a careful investigation of the two structures is presented.

11.1.1 Threshold with Temperature

An interesting issue, is whether the observed difference persists for a range of temperatures or it is an effect that manifests only at in low temperature. To compare the temperature behavior of the two orientations, the threshold current density of each laser diode was measured as a function of temperature. Fig.11.2 shows the comparison of the temperature dependent $J_{th.}$ for two typical devices of the same dimensions.

As may be seen (111)B oriented devices show a reduced threshold current density throughout the measured temperature range. The characteristic temperatures obtained from the exponential fit to the data shown in fig.11.2 are summarized in table 11.2.

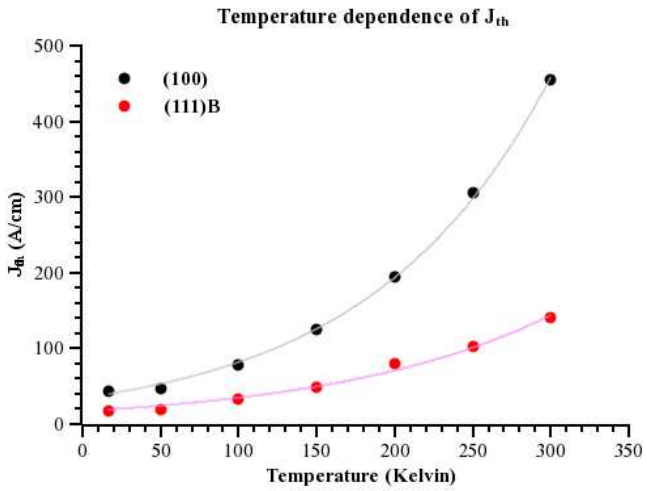

Figure 11.2: Threshold current density in the temperature range from 20 to 300 Kelvin. The (100) oriented device (black circles) exhibits a larger J_{th} for all temperatures compared to the (111)B oriented one (red squares). The lines correspond to exponential dependence of J_{th} to temperature. The characteristic temperature is found to be similar within experimental error. Laser devices are 1.5mm long and 40μm wide.

Orientation	*T_o (Kelvin)*
(100)	117±16
(111)B	124±9

Table 11.2: Characteristic temperature for laser structures grown on (100) and (111)B oriented substrates. There appears to be no difference in T_o between the two structures. This is consistent with the fact that T_o is affected by material quality and bandstructure which are expected to be similar in the two structures.

11.1.2 Threshold with Cavity length

Having established that the difference persists throughout a large temperature range, we may investigate the behavior of the devices with cavity length. Fig.11.3 shows the threshold current density (J_{th}) dependence with inverse length (1/L). It is obvious that there is a systematic difference in threshold current densities obtained for the two different orientations. In fact, the difference is enhanced for long cavities (low mirror losses) as may be seen by the different slope of the linear fit in fig.11.3.

Intrinsic cavity losses (a_i) are an important parameter as far as threshold current density is concerned. The observed difference in J_{th} could be partially explained by a difference in cavity losses between the two devices. In order to rule out the possibility that lower thresholds in the (111)B devices is a result of lower a_i, an estimate of the intrinsic absorption for each orientation was obtained using the analysis described in [96] and [97]. The estimate is achieved by measuring the differential power output of devices with different cavity length. The internal cavity losses (a_i) calculated from experimental data are shown in the following table.

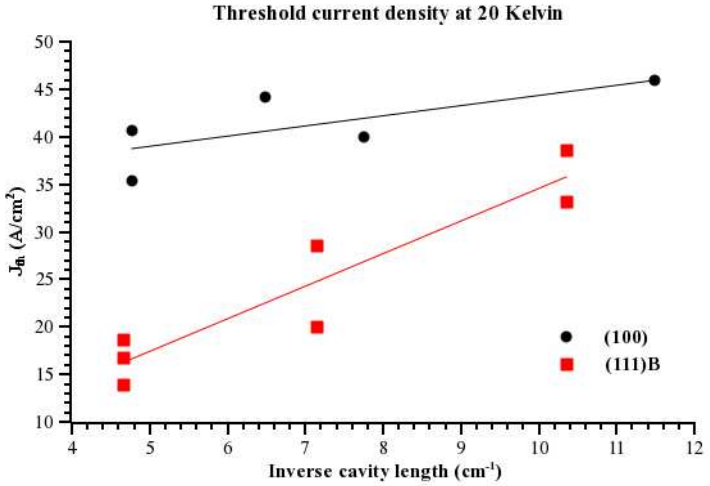

Figure 11.3: Threshold current density with inverse cavity length. The (111)B oriented devices (shown with red squares) exhibit reduced J_{th} for all cavity length measured when compared to (100) oriented devices (shown with black circles).The lines with the corresponding color are a guide to the eye. It is clear that the difference is enhanced for large devices (low 1/L).

Orientation	a_i
(100)	10cm^{-1}
(111)B	14cm^{-1}

Table 11.3: Estimate of the internal losses in the two different orientations. Even though the (111)B oriented devices have higher internal losses they still exhibit lower threshold current density of operation.

It is found that internal losses are higher for the (111)B oriented devices. This may be attributed to different sidewall optical scattering terms since the two crystallographic orientations may behave differently to laser ridge etching. It is thus clarified that not only do the (111)B oriented devices exhibit lower thresholds, but they also have higher internal losses which to the contrary should increase lasing threshold.

11.1.3 Summary

So far it has been established that edge emitting laser diodes grown on (111)B exhibit lower threshold current density at all temperature ranges. It is also clear that the lasing onset difference between (111)B oriented devices and their (100) counterparts is pronounced for large cavity lengths, where mirror losses are not dominating. Finally following the investigation of intrinsic cavity losses, it is clear that the difference in J_{th} can not be attributed to differences in laser diode fabrication.

Given the above, there is clear evidence that (111)B laser devices outperform their (100) counterparts. It is also clear that the observed difference is a result of inherent material properties and not device related issues. In order to further clarify the reasons for the observed differences, the time resolved decay of carriers inside each structure was studied. This will elucidate whether it is material quality that results in the observed threshold difference. The time resolved PL study will clarify whether there is a significant difference in material quality that could explain the observed

difference in lasing thresholds between the two samples.

Section:11.2. Time resolved study

In order to gain information regarding carrier dynamics in the two laser structures under investigation, time-resolved photoluminescence measurements were performed. Initially the PL intensity with pump power was investigated. Then, the carrier lifetime was measured as a function of temperature and these data were used to decouple the radiative and non-radiative lifetimes in each structure.

In the structure we study, there exists a number of layers that absorb at different wavelengths. Namely, starting from the low energy side, there is the InGaAs QW, GaAs from the top contact layer and the substrate, $Al_{0.15}Ga_{0.85}As$ from the core of the waveguide, and finally $Al_{0.3}Ga_{0.7}As$ from the cladding layers. The following table shows the corresponding wavelengths below which absorption takes place at each layer.

Material	*Absorption peak at 10 Kelvin*
$In_{0.15}Ga_{0.85}As$	876 – 880 nm
GaAs	828 – 830 nm
$Al_{0.15}Ga_{0.85}As$	~710 nm
$Al_{0.3}Ga_{0.7}As$	~650 nm

Table 11.4: Wavelength below which each of the materials contained in the structure under investigation absorbs. The required pump wavelength is chosen based on this table to be above the $Al_{0.15}Ga_{0.85}As$ but below the $Al_{0.3}Ga_{0.7}As$ absorbing edge. All values except the $Al_{0.3}Ga_{0.85}As$ are experimentally found from PL experiments on the same samples.

Attempting to pump at a wavelength where $Al_{0.3}Ga_{0.7}As$ absorbs will ensure that no radiation reaches the QW. This is true since the $Al_{0.3}Ga_{0.7}As$ layer is 1.6μm thick and practically all radiation will be absorbed there. Pumping at a wavelength where $Al_{0.15}Ga_{0.85}As$ is absorbing will ensure a large interaction with the pump beam and produce significant number of carriers in that layer that will eventually relax into the QW. In fact, this would be the wavelength of choice for time-integrated photoluminescence. However, since the relaxation time into the QW may be significant, the injected carriers will gradually be introduced into the QW. This situation is unwanted. The best option is to inject carriers abruptly, and then allow the system to relax back to the initial state following the luminescence from the QW. Thus, the best choice is to pump the QW resonantly. To avoid cross talk phenomena from the spectrograph, the pump wavelength should be as far as possible from the expected luminescence wavelength. Furthermore, the GaAs layer on top is heavily doped and produces a significant emission tail. As will be described later, when presenting temperature dependent experiments, it is important to ensure a constant number of injected carriers in the QW system. The easiest way to achieve this is to identify a wavelength region where the luminescence intensity is insensitive to variations of the pump wavelength. In order to ensure the correct pumping wavelength, a photoluminescence excitation experiment was performed for each sample. The wavelength of the pump beam was scanned through a wavelength region around 730nm. The PL intensity was recorded and the integrated emission from the QW was plotted as a function of wavelength.

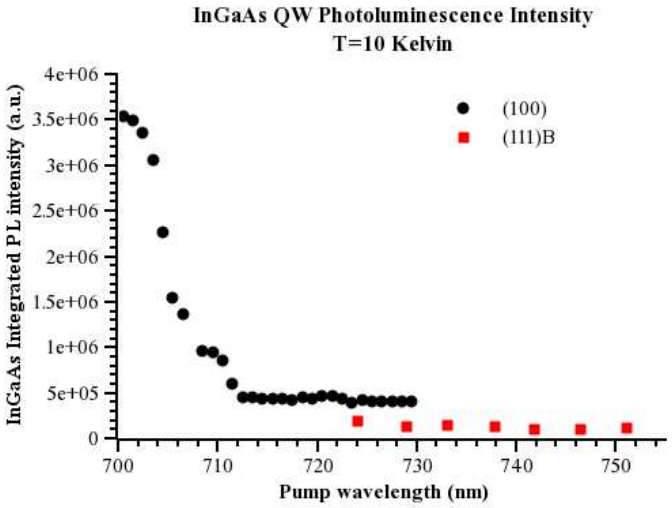

Figure 11.4: Photoluminescence intensity versus pump wavelength. The absorption edge of the $Al_{0.15}Ga_{0.85}As$ core layer is shown as an increase in the PL intensity of the (100) structure below 710nm.

Fig.11.4 depicts the resulting emission intensity. As may be seen there is a flat wavelength range several tens of nm wide where the intensity of the PL is independent of pumping wavelength. The pump wavelength for the following experiments was kept in this range to ensure constant carrier injection.

11.2.1 Carrier lifetime with Power

Initially, we explore the decay time dependence of carriers in the QW of each structure at varying pump power. Fig. 11.5 shows the comparison between the two structures. Comparing the decay times we observe the following differences: the (111)B QW exhibits decay times more than two times larger than the (100) one. If we assume that non-radiative effects are insignificant at low temperature, the difference is mainly attributed to the piezoelectric field effect. This is further indicated by the fact that (111)B decay time is reduced with increasing pump power.

This can only be explained if we assume that increasing the pump power results in partial screening of the piezoelectric field from the injected carriers. This modifies the overlap of the electron and hole eigenstates, thus the radiative lifetime decreases accordingly as already discussed in [98]. On the contrary, the (100) QW should exhibit a slight increase in radiative lifetime as predicted by [53].

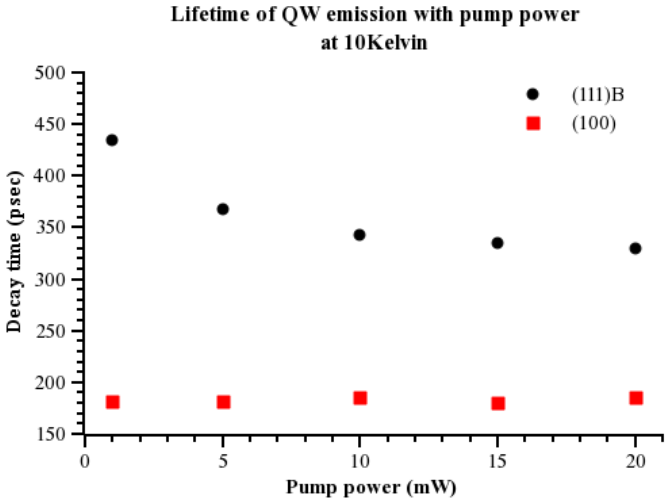

Figure 11.5: Carrier decay time at 10Kelvin as a function of pump power. The decay time in (111)B is significantly larger compared to the (100). Furthermore, the dependence is difference. This is attributed to the piezoelectric field which is partially screened for large pump power, thus allowing for faster radiative recombination. The estimated carrier densities injected in the QW are $3 \cdot 10^{10} - 5 \cdot 10^{11}$ cm^{-2}.

If we compare the time resolved emission images, shown in fig. 11.6 we may directly see that the emission of the (111)B QW red-shifts as the carrier density decays with time whereas the corresponding emission of the (100) oriented QW is fixed.

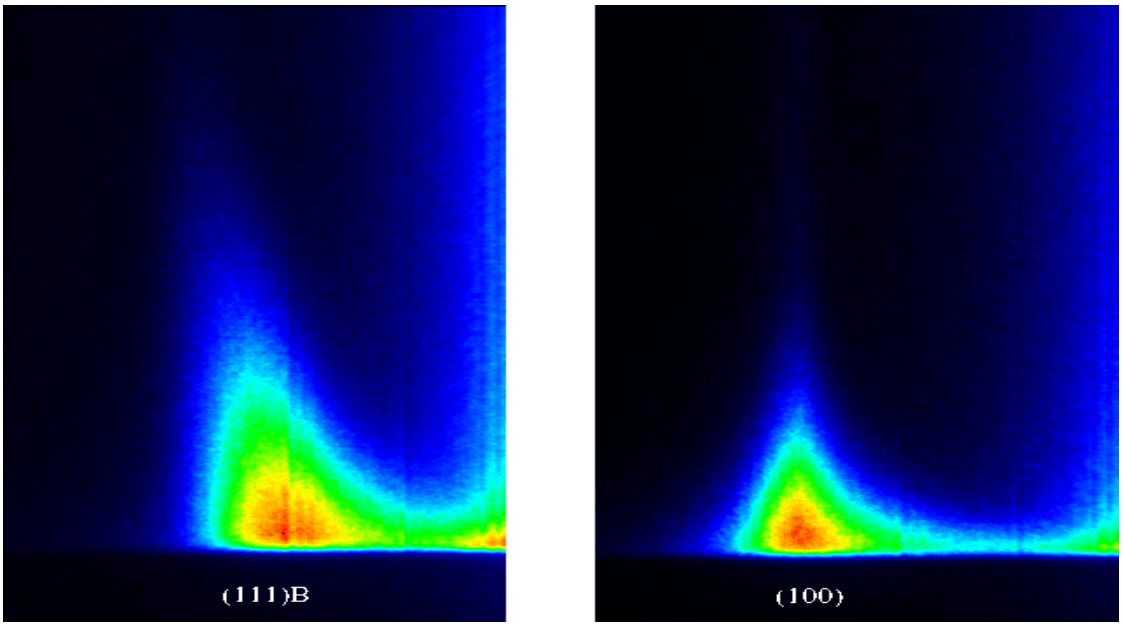

Figure 11.6: Time resolved emission images from (111)B (left) and (100) (right) laser structures. The horizontal axis corresponds to wavelength (increasing to the left) whereas the vertical axis corresponds to time. The (111)B exhibits significant red-shifting as the carrier density decays whereas the (100) has a fixed wavelength. Also the difference in decay times is evident.

So far it is established that decay times are significantly different between the two structures. Furthermore, the effect of piezoelectric field screening has been observed in the quantum confined stark shift of the PL emission of the (111)B quantum well. The next step is to investigate the temperature dependent behavior of the samples.

11.2.2 Carrier lifetime with Temperature

When performing temperature dependent photoluminescence measurements, there is a need to ensure that a constant pump intensity is absorbed in the region under investigation. This ensures that the injected carrier density remains constant across the experiment. Thus one may compare luminescence intensity and reach a conclusion about efficiency with temperature.

If the pump wavelength is kept constant, then the temperature shift of the bandgap will result in different pumping intensities across the temperature range. To remedy this, the pump wavelength was constantly tuned following the bandgap changes. To ensure uniform pumping across temperature, a wavelength range were each sample absorption is relatively constant was selected.

Using the information gained from fig.11.4 we keep the pump wavelength in the wavelength range where the samples exhibit a flat absorption. Then using the Varshni equation we predict the bandgap shift and tune the pump wavelength to follow the flat absorption range. This way we can assume that the injected carriers are constant throughout the experiment. The selected pump power was 10mW which corresponds to approximately $2 \cdot 10^{11} cm^{-2}$ injected carriers per pulse.

As the temperature increases, it is expected that the luminescence intensity will drop. This is because non-radiative effects are strongly temperature dependent. At the same time, the decay time which is a superset of both radiative and non-radiative times, will decline as well. Fig. 11.7 shows the PL intensity and the corresponding decay times from 10 to 220 Kelvin for the (100) oriented sample.

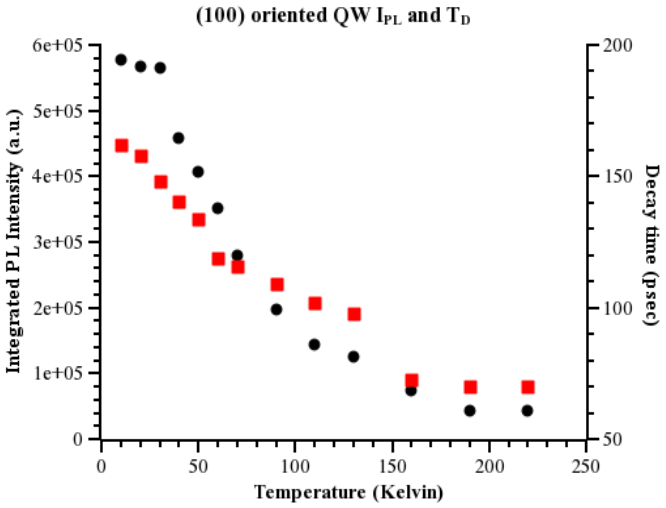

Figure 11.7: Time-integrated photoluminescence intensity (black circles) and corresponding decay times (red squares) versus temperature for (100) oriented structure. A range below 30 Kelvin I_{pl} remains constant. For higher temperatures, the intensity drops exponentially. It is estimated that approximately $2 \cdot 10^{11} cm^{-2}$ carriers are injected per pulse.

As may be seen, there is a small range up to 30 Kelvin, where the intensity does not change significantly. Above that, the PL intensity drops exponentially.

The corresponding plot for the (111)B structure is depicted in fig.11.8.

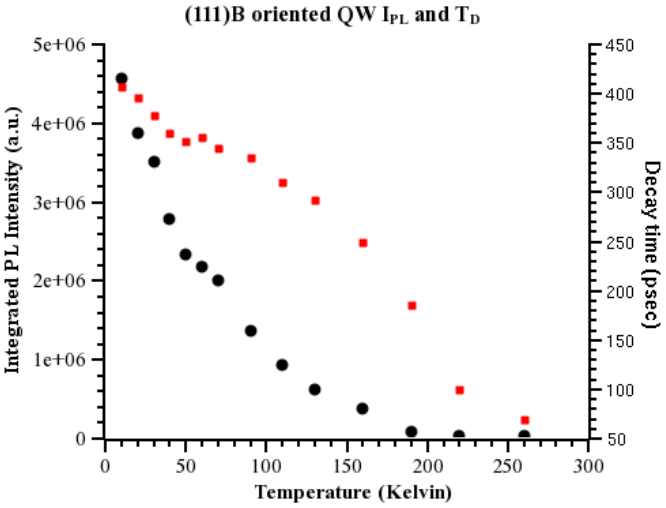

Figure 11.8: Time-integrated photoluminescence intensity versus temperature for (111)B oriented structure. The PL intensity exhibits an exponential decay behavior with temperature. No low temperature regime was identified were the intensity is constant.

Although caution needs to be exercised comparing the intensity between samples, since a number of parameters may indirectly affect the absorbed carriers or the collected emission, it appears that the low temperature PL intensity of the (111)B sample is higher by nearly an order of

magnitude. Furthermore, the decay times are also different, especially in the low temperature regime. Theoretically, the radiative decay time is expected to be different for the two structures. That is explained qualitatively due to the reduce electron-hole state overlap in the (111)B structure due to the piezoelectric field. Using the measured decay times with temperature, we can calculate the radiative and non-radiative decay time for each sample.

11.2.3 Radiative and non-radiative lifetimes

Using the data presented in the previous paragraph we may obtain an estimate of the radiative and non-radiative lifetimes in the two structures. There is however a degree of uncertainty regarding the efficiency of the luminescence at low temperature. Assuming that at 10Kelvin the radiative efficiency is close to unity (0.99), we obtain an estimate of non-radiative lifetime, depicted in fig. 11.9.

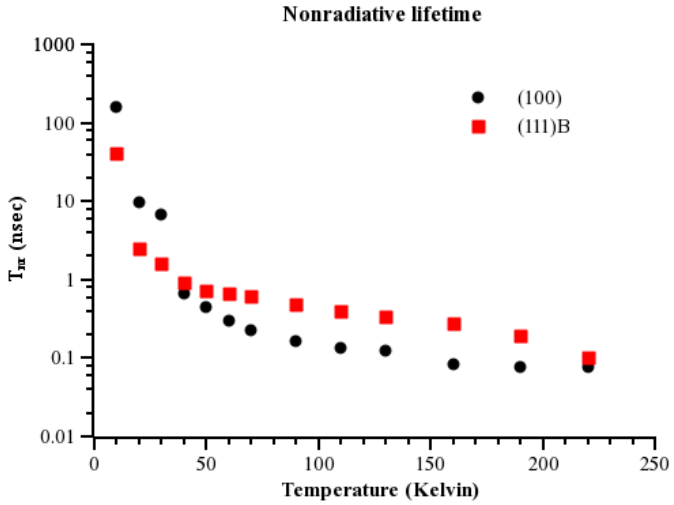

Figure 11.9: Calculated non-radiative lifetime. A low temperature efficiency of 0.99 was assumed for both samples. The non-radiative lifetimes appear similar in the two orientations, with the (111)B structure however exhibiting longer lifetime over a large temperature range.

Although the (111)B oriented structure exhibits higher non-radiative lifetime than its (100) counterpart, this is not true for the entire temperature range. Thus the difference in threshold may not be attributed to the non-radiative lifetime difference. It is interesting however that (111)B grown material performs better in terms of non-radiative lifetime which is a signature of high material quality.

Furthermore, the radiative lifetime is extracted for both samples. Fig. 11.10 depicts the calculated radiative lifetime as a function of temperature for both samples.

It is interesting that with increasing temperature, the radiative lifetime from (111)B appears to increase substantially reaching a value as high as 5nsec. Whereas the (100) radiative lifetime increases slightly. Qualitatively, the different slope can be understood according to the theory of Andreani et al. [99] due to the higher exciton mass of the (111)B exciton and the lower oscillator strength in the (111)B QW due to the presence of the piezoelectric field.

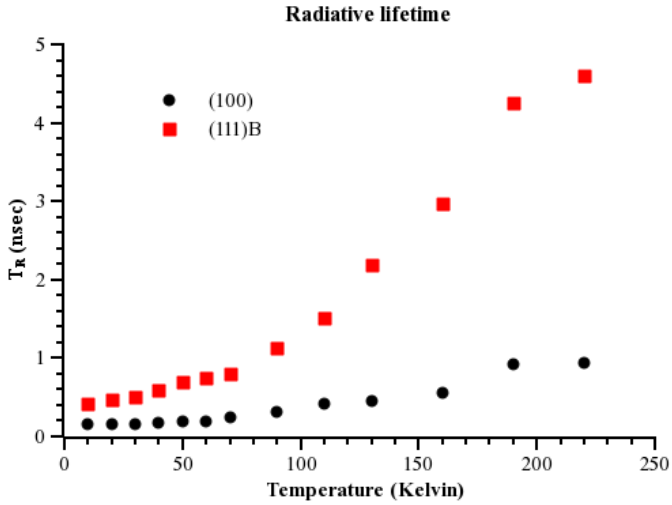

Figure 11.10: Calculated radiative lifetime. Theoretically it is expected that the T_R will gradually increase with temperature since high k states are occupied. It is also noted that the (111)B sample exhibits higher radiative lifetimes over the entire range of temperature studied.

Fig. 11.11 depict the radiative efficiency for the two samples with increasing temperature. It is clear that the (100) efficiency is larger compared to the (111)B one. This along with the rest of the results presented so far, implies that the improved performance of the (111)B structure is not related to material quality but rather to other phenomena.

In summary we have studied both (100) and (111)B oriented laser diode structures using time resolved photoluminescence technique, in order to estimate the radiative and non-radiative lifetimes of each structure. Comparing the radiative efficiency we show that it is smaller for the (111)B. This allows us to conclude that the difference in threshold performance between the two structures is not

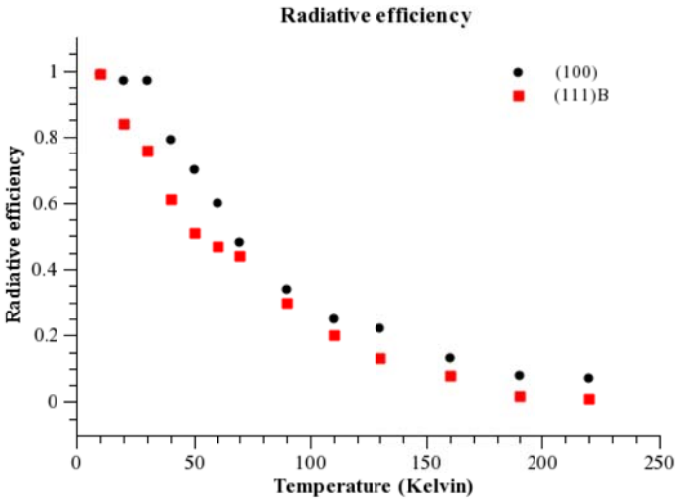

Figure 11.11 *0) black and (111)B red.*

a result of superior optical quality of the (111)B structure but is rather a result of their modified

properties due to different orientation.

Section:11.3. Theoretical investigation of (111)B and (100) LD's

So far a number of experimental techniques have been applied to the (100) and (111)B oriented laser diode structures in an attempt to pinpoint the origin of the performance difference. It is reminded that the ultimate goal is to isolate the effect of the built in electric field to the lasing characteristics of the polar devices. In order to further study this system, ab-initio calculations were performed to obtain the band structure and the current gain characteristics. Based on the theoretical description discussed in earlier chapters a self consistent Poisson Schroedinger solver was implemented. The solver is given the unperturbed bandstructure (no-carriers) and the desired carrier density and calculates the resulting band structure, as well as the optical gain, the spontaneous emission and the required current to maintain the carrier concentration constant. The results are discussed in detail in the following paragraphs.

11.3.1 Bandstructure with carrier density

As the carrier density inside the piezoelectric quantum well is increased, a screening effect is expected. Fig 11.12 shows the expected band structure of the quantum well under different carrier densities. The first question that rises is whether there is a residual electric field for carrier densities high enough to produce gain. The initial finding is that a residual electric field is still present in the active quantum well even for carrier densities large enough ($10^{12}cm^{-2}$) to produce gain and thus lasing.

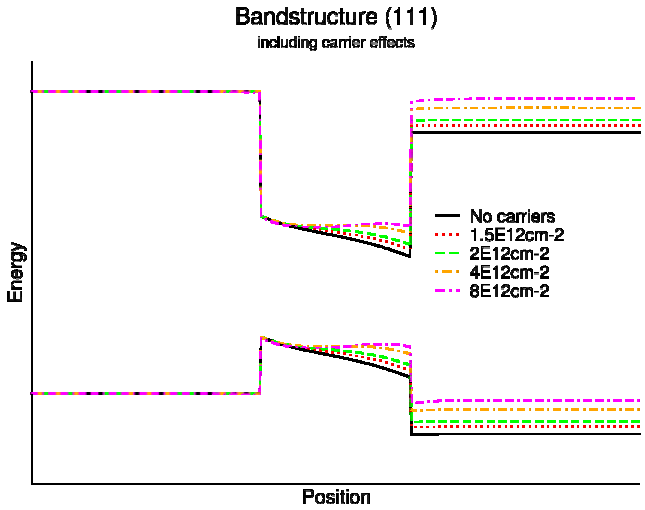

Figure 11.12: Theoretical calculation showing the band structure of a piezoelectric InGaAs quantum well under different carrier densities. Even for density as high as 8E12cm^{-2} there is a remaining electric field present in the quantum well. The calculation was performesd using self consistent Poisson Schroedinger in the effective mass approximation.

It is expected according to our calculations that even at a carrier density as high as 8E12cm-2 there is a significant residual field in the structure. This finding is consistent with the indications

from the experimental results of the lasing characteristics as well as the time resolved photoluminescence measurements. As expected, in the non-polar case, namely the (100) orientation the quantum well is flat regardless of the carrier concentration.

The direct implication of this finding is that even at carrier densities needed for lasing, the electron and hole eigenfunctions will not be centered in the piezoelectric well. Fig.11.13 (left) shows a typical line up of the electron and hole ground state at low excitation.

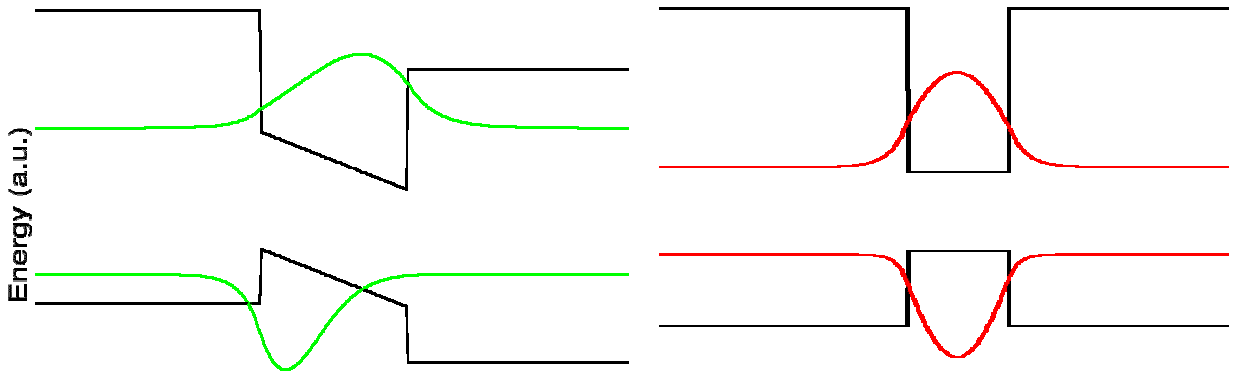

Figure 11.13: Schematic of the eigenfunction asymmetry in a piezoelectric quantum well (left) and for a non piezoelectric quantum well (right).

Comparing the two cases, it is clear that the overlap of the two eigenfunctions is reduced for the piezoelectric case, thus reducing accordingly the interaction between the carriers. This has a direct impact on the gain profile. Higher states are also affected as will be discussed later.

Increasing the carrier density inside the well, will partially screen the built in piezoelectric field and thus the electron hole states are expected to shift towards the center of the well. This is expected to have an effect on optical gain.

11.3.2 Gain calculation

Using the described calculation method, we may estimate the TE optical gain for a given carrier density in the quantum well. For the case of non-polar (100) orientation the calculation of gain is straight forward. Fig. 11.14 shows the gain for different carrier densities in the QW.

A careful examination of the gain curve reveals the electron and hole ground state (e1 – hh1) and the first excited states (e2 – hh2) transitions. As expected from basic quantum mechanics, the crossed (e1 – hh2) and the (e2 – hh1) transitions are forbidden and do not show up.

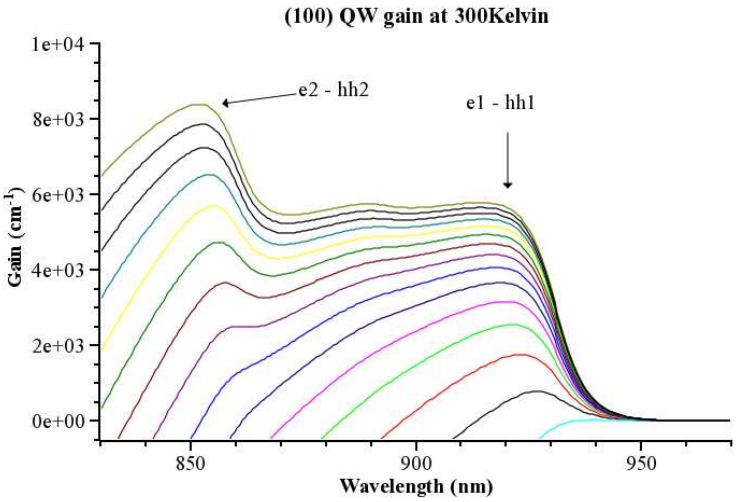

Figure 11.14: Calculated room temperature TE gain for (100) oriented QW, for several carrier densities (from $1 \cdot 10^{12}$ to $8 \cdot 10^{12}$ cm^{-2} with a step of $5 \cdot 10^{11} cm^{-2}$). The two allowed transitions are marked with arrows.

Following the same reasoning for the polar orientation namely (111)B we obtain fig.11.15.

Comparing fig.11.14 and 11.15 we see some profound differences in the gain profiles. To begin with, in the piezoelectric QW, the symmetry of the states is relaxed, this is due to the electric field inside the well. This creates a non-vanishing transition probability between crossed transitions, such as (e1 – hh2), which is manifested in the gain curve as additional peaks. Furthermore, there is a difference in the gain maximum for the same carrier density between the two orientations. The (111)B oriented quantum well produces less gain for the same carrier density. This can be explained

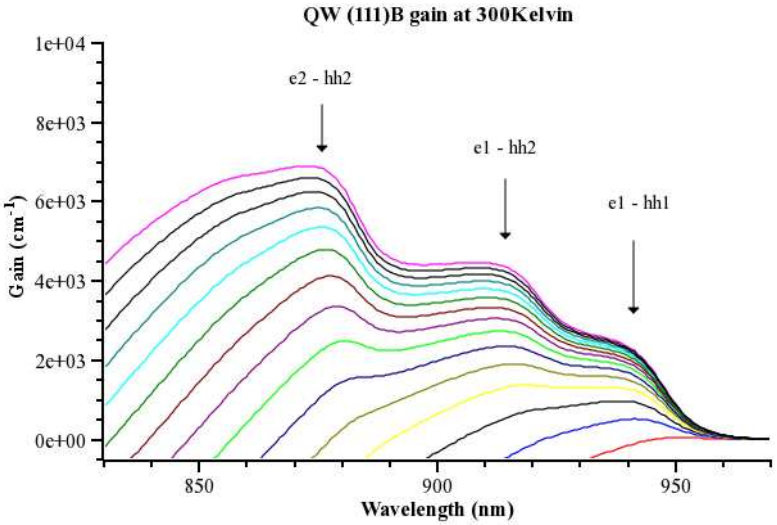

Figure 11.15: Calculated room temperature (111)B grown QW gain, for several carrier densities (from $1 \cdot 10^{12}$ to $8 \cdot 10^{12}$ cm^{-2} with a step of $5 \cdot 10^{11} cm^{-2}$). Since the piezoelectric field breaks the QW symmetry, crossed transitions are now allowed and may be seen in the gain curves.

in terms of a reduced eigenstate overlap between the electron and hole eigenfunctions.

Plotting the residual electric field and the eigenfunction overlap on the same figure for different values of gain maxima we obtain fig.11.16. As is expected, increasing the gain (thus the carrier

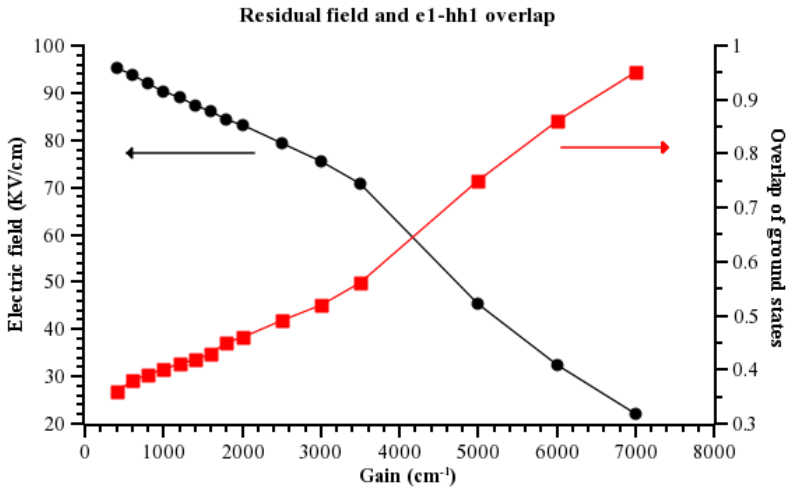

Figure 11.16: Residual piezoelectric field (black circles) and ground state overlap (red circles) with maximum gain.

density) the residual field is reduced and the overlap of the electron and hole ground states is increased. Both effects however persist up to very large gain values.

11.3.3 Spontaneous emission

Using the gain curve, we can calculate the spontaneous emission for each orientation using the known relationship between gain and spontaneous emission (presented earlier).

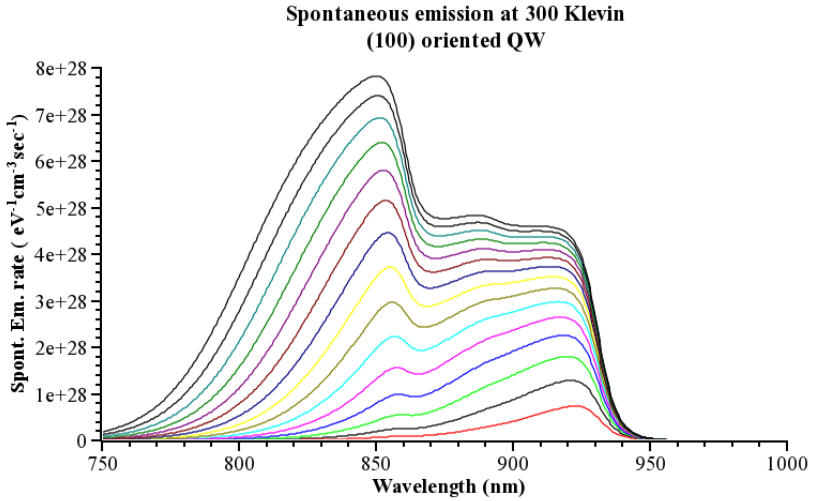

Figure 11.17: Spontaneous emission spectra at 300 Kelvin for a 10nm QW grown on (100) orientation. Spectra correspond to 1E12cm^{-2} to 8E12cm^{-2} carrier density in the QW. Similar features compared to the gain curve discussed previously exist in the spontaneous emission.

Fig.11.17 depicts the spontaneous emission spectra of the QW oriented along the (100) orientation. Features similar to the ones shown in the corresponding gain curves discussed in the previous paragraph exist also in the spontaneous emission spectra.

Along the same lines, fig.11.18 shows the spontaneous emission spectra from the polar oriented QW, namely (111)B obtained from the gain curves of fig.11.15.

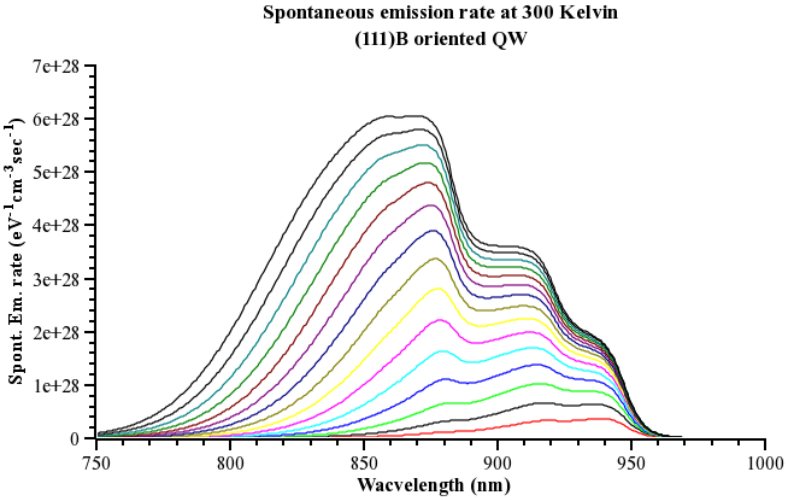

Figure 11.18: Spontaneous emission spectra at 300 Kelvin for a 10nm QW grown on (111)B orientation. Spectra correspond to 1E12cm^{-2} to 8E12cm^{-2} carrier density in the QW. Similar features compared to the gain curve discussed previously exist in the spontaneous emission.

Comparing the spontaneous emission rates for same carrier density, we observe the existence of the crossed transitions in the polar QW which are forbidden in the (100) case. Furthermore, the spontaneous emission rate is reduced in the (111)B case compared to the (100) one. This is consistent with the reduction of the gain intensity discussed in the previous paragraph due to the reduced overlap of the electron hole states.

However, for the case of spontaneous emission, the reduction works in favor of the laser diode performance. In a laser diode, spontaneous emission is considered to be a loss mechanism, in fact, should non-radiative and leakage phenomena be ignored, the spontaneous emission is the sole mechanism for electron hole recombination, before the laser starts operating. Under these conditions, the injected current – in order to achieve a steady state gain – in a cavity has to counter act the annihilated carriers due to spontaneous emission.

11.3.4 Current calculation

Integrating the spontaneous emission rate over all energies we obtain the rate of emitted photons. Thus, an estimate of the carriers that need to be injected in order to keep the carrier density constant is readily found. Using this approximation, we can calculate the current for each one of the calculated gain spectra presented above. Finally the gain maximum – which is where lasing should occur – is also known. This way we may derive theoretical current density vs gain plots.

As discussed, there are two counteracting mechanisms when comparing the piezoelectric and

non-piezoelectric QW's. Initially there is gain reduction which is negative, in the sense that larger carrier density needs to be injected in a QW to obtain the same gain maximum. On the other hand, spontaneous emission rate is also affected by the piezoelectric nature of the QW. Reducing the spontaneous emission rate, the injected current necessary to reach a given carrier density in the well is also reduced. Depending on which of the two mechanisms dominates, a net positive or negative effect on the threshold current density may be obtained.

Performing the current calculation, we plot in fig.11.19 the TE gain spectra for various current densities injected in the two structures. In all cases, the (111)B gain maximum is significantly larger compared to the (100).

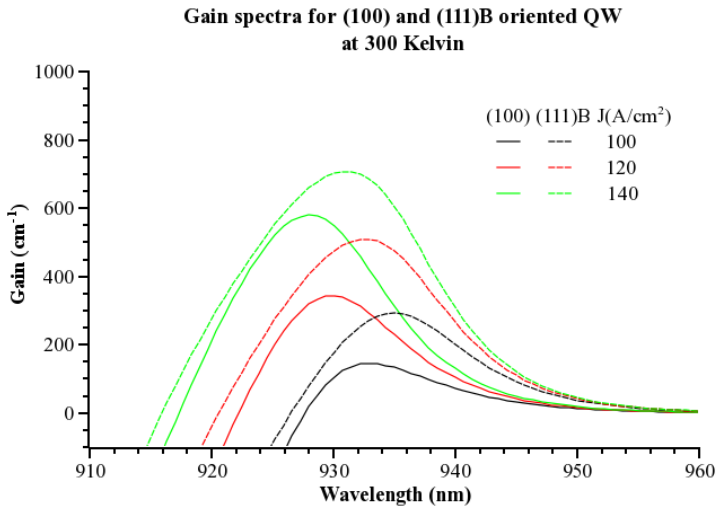

Figure 11.19: Comparison of gain spectra for (100,120 and 140 A/cm^2) injected current into a (100) and a (111)B oriented QW. The gain maximum for the (111)B is significantly larger for the (111)B. Data calculated for 300 Kelvin.

A word of caution is necessary at this point. Besides the piezoelectric field, there is another difference between the (100) and the (111)B QW's that may significantly affect the gain spectra. The hole band in InGaAs is strongly dependent on axial orientation. This affects the in-plane effective mass of the InGaAs active QW. Table 11.5 shows the hole effective masses used to calculate the data presented in this section.

Orientation	*Inplane hh mass*	*Inplane lh mass*
(100)	0.182	0.082
(111)B	0.110	0.097

Table 11.5: Hole effective masses used to obtain the inplane dispersion curve of the $In_{0.1}Ga_{0.9}As$ QW on each orientation. The large difference in hh effective masses is expected to affect device performance, favoring (111)B which exhibits lower inplane hh mass.

The difference in electron and hole effective masses results in a different distribution of the carriers in the in-plane momentum space. Given the fact that photons have insignificant momentum, electrons and holes that recombine must have the same k. Having different k-space distribution results in non-optimum overlap in the population for each k (especially higher k components). This

is a side effect from the very nature of semiconductors and cannot be changed. However, (111)B grown QW's exhibit a lower in-plane hh effective mass. This reduces the difference to the electron effective mass (which is small) thus reducing the difference in k-space distributions. It is thus expected that the improved performance of the (111)B grown structures can be partially attributed to this effect as well as the piezoelectric field. In order to quantify to which extent the piezoelectric field is responsible for the superiority of the (111)B structure, besides the calculated (100) and (111)B structures, a non-existing "gedanken" structure is simulated. In this structure, the effective masses are those of the (111)B but the piezoelectric fields are neglected. Using this structure, allows a direct estimate of the piezoelectric field effect.

In order to match the internal absorption extracted from the experimental data (a_i=10-14cm^{-1}) the quantum well needs to exhibit a gain in the order of 500cm^{-1}. This was calculated taking into account that the QW confinement factor is $\Gamma \approx 2\%$. Using the gain and spontaneous emission spectra calculated earlier, we may obtain an estimate of the corresponding injected current for each structure. Fig. 11.20 shows the theoretical current density for a temperature range of 20 to 300

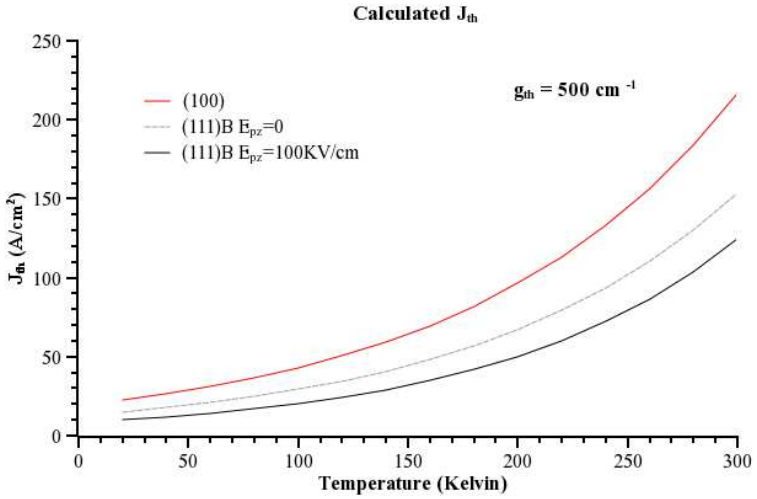

Figure 11.20: Theoretical calculation of J_{th} versus Temperature. The (111)B (black solid line) exhibits lower threshold than the (100) (red solid line) validating the experimental findings. The effect is both due to effective mass difference as well as to the piezoelectric field, as can be seen from the gray line which shows only the effective mass contribution.

Kelvin. According to the theoretical J_{th} depicted in fig.11.20, both the effective mass difference as well as the piezoelectric field reduce the current threshold of the (111)B oriented devices. Comparing this with the experimentally measured threshold current density versus temperature in fig.11.2, we see that the (111)B theoretical data predict very well the experimental curve. The experimental data that correspond to (100) exhibit higher threshold than the theoretically calculated one. This may be attributed to non-radiative recombination which is consistent with the findings from the time resolved experiments described in the previous section.

To take into account the limited length of a real device, we need to plot the theoretical J_{th} for a range of g_{th}. The latter is directly connected to the inverse length of the device through the well

known equation $\Gamma \cdot g_{th} = a_i + \frac{1}{L} \cdot \ln\left(\frac{1}{R \cdot R}\right)$ where R is the mirror reflectivity (assumed to be the same for both mirrors R≈32%).

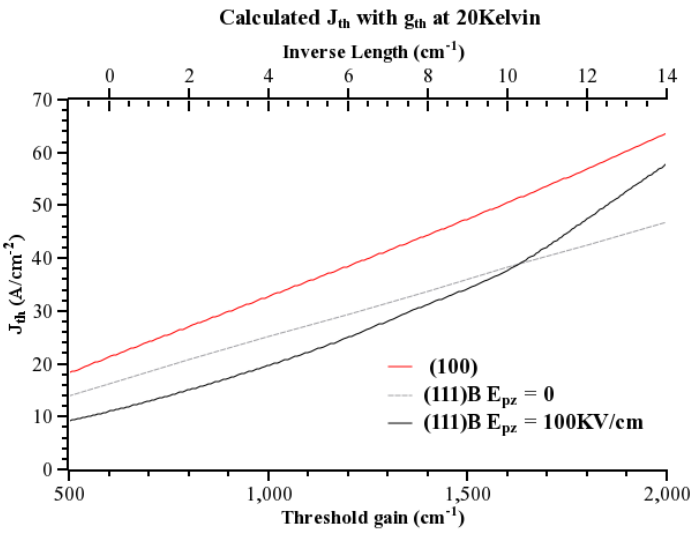

Figure 11.21: Calculated J_{th} versus g_{th}. The top axis corresponds to the 1/L assuming an a_i=14cm^{-1}. The (100) calculated threshold values (red line) are larger over the entire range of g_{th}. Comparing the (111)B (black solid line) with the "gedanken" (111)B without piezoelectric fields (gray dashed line),we may see a range of g_{th} were the piezoelectric field improves the overall behavior whereas for high g_{th} it has a negative effect.

Fig.11.21 depicts the dependence of J_{th} on g_{th} (bottom axis) and provides an indication of the associated inverse length values, if a_i is assumed to be 14cm^{-1}. It is shown that although the (111)B structure is expected to exhibit lower threshold values for a large range of cavity lengths, the role of the piezoelectric field depends on the requested threshold gain. For large cavity lengths, thus small inverse length (small threshold gain) the piezoelectric field works in favor of the overall performance. The spontaneous emission rate reduction is dominating at this regime making it easier to introduce carrier density in the structure. For large threshold gain, which correspond to short cavity length, the requested gain is close to the maximum gain that can be achieved in the QW (complete inversion). In this regime, the limiting factor is gain maximum reduction, thus the piezoelectric field has a negative effect since it reduces the gain due to reduced state overlap.

Section:11.4. Summary

In this chapter the performance of (100) and (111)B laser diode structures was compared. Clear evidence of improved performance of (111)B oriented laser diode structures were presented. In fact (111)B structures were shown to have lower threshold current density at all measured temperature and cavity length [100]. Especially for the case of long cavities, the enhancement is pronounced.

The material emission dynamics were investigated using time resolved photoluminescence techniques and the decay times, radiative and non-radiative lifetimes of carriers were extracted from this analysis. It was shown that (111)B exhibits larger decay times, mainly due to the piezoelectric

nature of the QW which enhances radiative lifetimes, as well as to reduced non-radiative recombination rate [101].

Finally, the structures were studied using theoretical ab-initio calculations, and the main mechanisms behind the performance difference were identified. It was found that inherent material properties such as the different QW in-plane effective masses contribute to the performance enhancement. At the same time however, contrary to the general scientific consensus that piezoelectric fields are deteriorating performance, it was shown that a significant part can of the improvement can be attributed to the piezoelectric field produced in polar (111)B orientation for pseudomophically grown InGaAs [102][103].

The significance of the presented data is enhanced when applied to novel material systems such as the III-N [104] where, until now, the only high quality material available is grown on polar orientations (0001).

Chapter 12.Dynamic Fields in Laser Diodes

The following section presents the initial experiments to evaluate the role of $Al_{0.4}Ga_{0.6}As$ barrier characteristics in the performance of gain tunable laser diodes via the quantum confined Stark effect (QCSE). Section 2 provides a comparison of tunable laser diodes with barriers made from different $Al_xGa_{1-x}As$ composition.

Section:12.1.Tunable Laser devices based on $Al_{0.4}Ga_{0.6}As$

As discussed earlier, the concept to fabricate a gain tunable device, is to establish a dynamic electric field acting on the active quantum well of the laser structure. Placing a thin barrier directly before the active quantum well, will force a portion of the injected carriers to reside before the barrier thus outside the quantum well. This will impose a Stark shift on the quantum states of the quantum well that will in turn result in red-shifting the gain maximum. Preliminary experiments were performed using $Al_{0.4}Ga_{0.6}As$ barriers. The reasoning behind this choice is simple. First of all $Al_xGa_{1-x}As$ is a direct gap material for $0<x<0.4$. Furthermore the discontinuity between GaAs and $Al_{0.4}Ga_{0.6}As$ is significantly large compared to kT.

12.1.1 Barrier balancing

In order for this approach to work, the barriers have to exhibit a “symmetric” behavior. By symmetric we mean that the barrier on the electron side should have an electron tunneling time similar to the tunneling time that the opposite barrier exhibits for holes. Should this not be the case, an unequal density of electrons and holes would reach the active quantum well. The excess carrier density, however, does not contribute to the gain, whereas it does contribute to screening effects which are unwelcome in the active region of a laser diode.

In order to study the optimum relative thickness of electron and hole barriers respectively, a series of laser diode structures were grown varying only the hole barrier thickness.

Sample	*h^+ thickness*	*e^- thickness*
353	12 nm	12 nm
351	10 nm	12 nm
360	8 nm	12 nm

Table 12.1: Structures grown to study the effect of relative barrier thickness. All structures are based on waveguide A.

Fig.12.1 shows the electroluminescence shift observed at low temperature (20Kelvin) for the

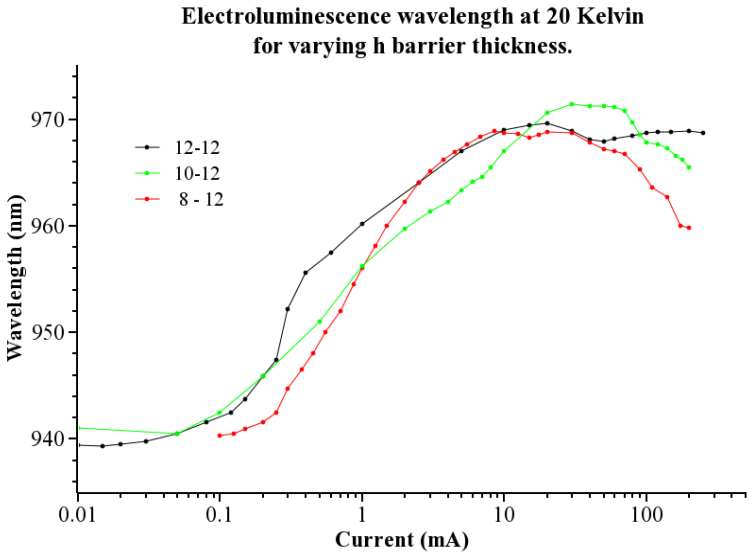

Figure 12.1: Electroluminescence emission peak with current for three different samples with varying h-barrier thickness. Similar shifts are obtained.

three samples described in Table 12.1. All samples exhibit approximately the same shift namely from 940 to 970nm. It is significant to observe that the total shift of 30nm corresponds to an electric field in the order of 150KV/cm^2 which is a large value. The 10nm h-barrier LD shows a somewhat more linear Stark shift, but the differences are very subtle. Another way to investigate the successful balance of the two barriers, would be to see the emission intensity from the areas outside the barriers. Two GaAs quantum wells that were included in the structure directly next to the barriers. The e side has a GaAs "collection quantum well" (CQW) with 4.5 nm thickness whereas the h side collection quantum well is 20nm wide. The term "CQW" comes from the fact that this area is expected to collect carriers that are blocked by the tunneling barriers.

Fig.12.2 shows the emission from the two collection quantum wells (the e-CQW emits at 780nm whereas the h-CQW emits at 810nm) and the active well emission. It is interesting to note that from the three samples under investigation only the one with 10nm h-barrier does not exhibit CQW luminescence. Although it the mechanism leading to luminescence from the CQW's is not understood at the moment, it is clear that CQW luminescence is in essence lost carriers that recombine away from the central – active QW. Ideally, a structure where all recombination takes place in the active QW is desired. In this line of thinking the optimum behavior is observed from the sample with 12 and 10nm barriers for electrons and hole respectively.

12.1.2 Barrier thickness

As shown in the previous paragraph, large Stark shifts from the active QW are possible. A careful inspection of Fig.12.1 reveals that the entire shift comes in a current range of 0.1-10mA whereas the lasing threshold for these devices is 50mA. It is thus necessary to modify the structure and match the current density region for which the shift is exhibited to the proper current range namely that where lasing occurs.

This can be achieved by changing the barrier thicknesses. The thicker the barriers, the more difficult it is for carriers to tunnel into the active quantum well. This in turn, translates to increased carrier densities being stored in the collection QW and therefore increased space charge field. It is important to pinpoint the optimum thickness so that the Stark shift is not developed too early (before the laser reaches threshold) or too late (at very high operating currents where the laser has already exceeded threshold current density by a large factor.

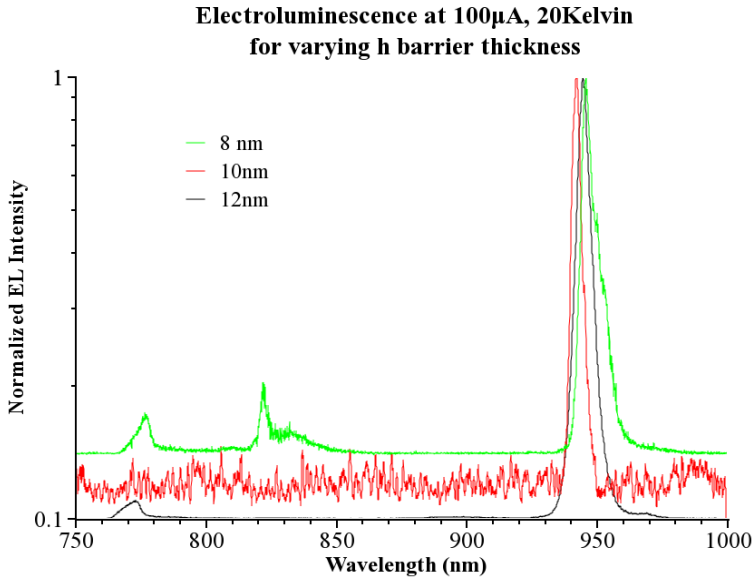

Figure 12.2: Emission from the collection wells for pump current of 100uA. Plots are normalized to the active quantum well emission. Notice that for the case of 8nm h-barrier, both collection wells emit light. On the other end, for the 12nm h-barrier, the 4nm collection well (the electron collection well) emits light. Finally for the 10nm h-barrier case, no visible emission from the collection wells is observed.

A series of laser diode samples were grown, varying both electron and hole barrier thickness. All samples were grown using the same barrier height namely $Al_{0.4}Ga_{0.6}As$. The following table depicts the parameters used. The relative thicknesses of the electron and hole barriers were adjusted based on the findings of the previous paragraph.

Sample	*e^- thickness*	*h^+ thickness*
364	10 nm	8 nm
642	9 nm	7 nm
593	7 nm	5 nm
594	6 nm	4 nm

Table 12.2: Structures grown to study the effect of barrier thickness to the emission shift. All structures are based on waveguide A. Barriers are $Al_{0.4}Ga_{0.6}As$.

Laser diodes were prepared from each of the described samples and the emission wavelength was measured at low temperature (50 Kelvin). The results are depicted in Fig.12.3. The sample containing 8 and 10 nm barrier for electrons and holes respectively, exhibits a shift from a current density as low as 0.01A/cm^2. As the barrier thickness is diminished for the other samples, the Stark shift manifests at larger current density. This is explained by the fact that thinner barriers result in less carrier build up in the collection wells and hence less space charge field thus diminished Stark effect on the active quantum well. Another interesting observation is the fact that emission shift can reach 35nm for the sample containing the thicker barriers. Samples with thinner barriers may be able to achieve the same shift but for current densities that are prohibitively large.

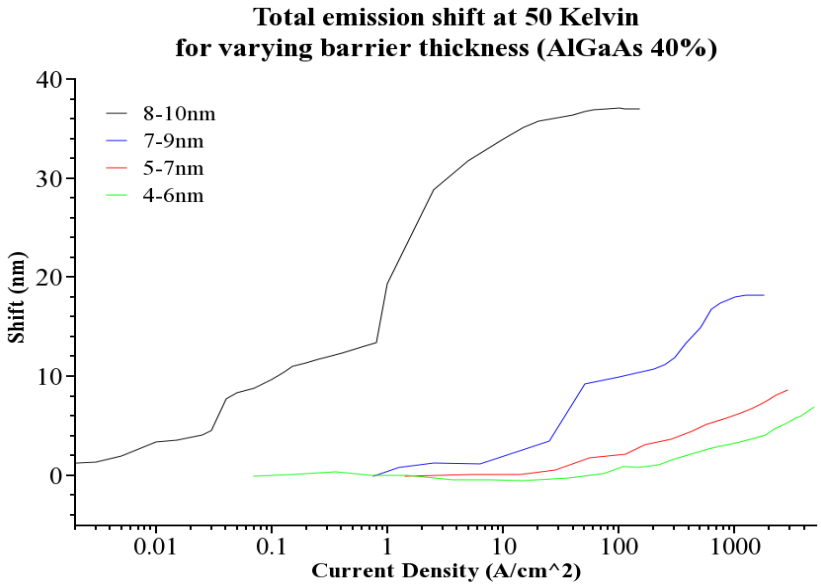

Figure 12.3: Electroluminescence emission shift with pump current density. As expected the emission shift comes at larger current density for samples with thin barriers.

Since the objective is to fabricate a tunable laser diode, it is important to see the emission shift during lasing operation. This is depicted in Fig.12.4.

Similar behavior is observed concerning the current density in the lasing regime. The thicker the barriers, the earlier the shift is observed. Furthermore, thick barriers result in sharper shift for the same change in current density. However, the larger shift is now observed for the sample with 7 and 9 nm thick barriers. This is explained considering the results of Fig. 12.3. The 8-10nm sample,

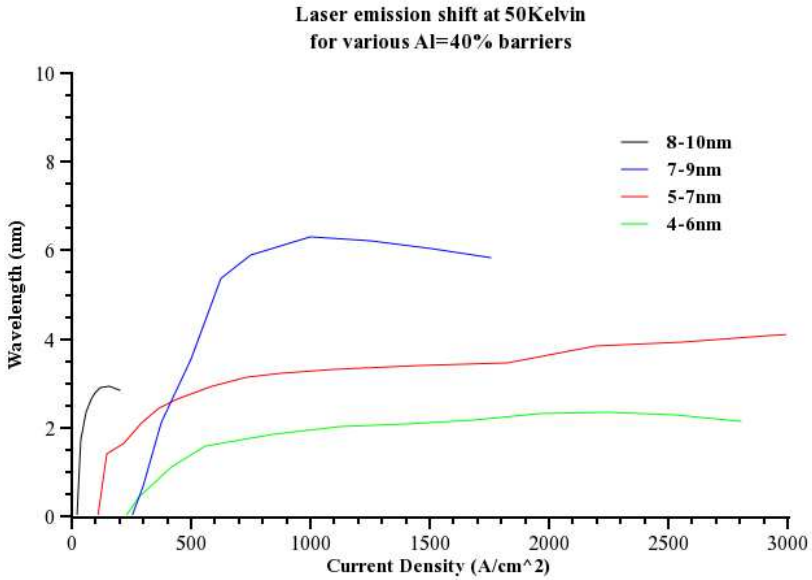

Figure 12.4: Laser emission shift for the samples described in Table 12.2. Analogous behavior to the luminescence shift described before is observed here. All samples are based on waveguide type A and heating effects have been subtracted.

exhibits most of the shift below threshold, thus the remaining shift above threshold is only a small fraction of the total shift caused by the barriers.

Fig.12.5 shows the normalized emission as a function of wavelength (y-axis) and current density (x-axis) for sample 364.

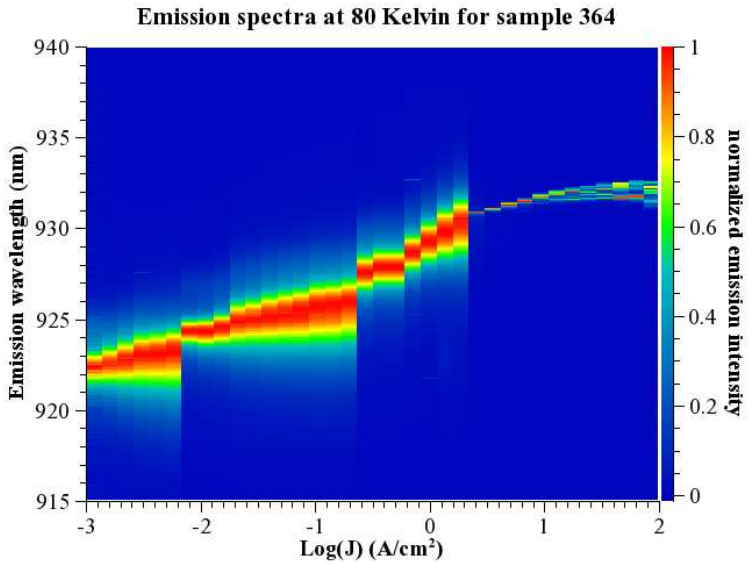

Figure 12.5: Emission spectra for sample 364 (8-10nm barriers) throughout the current range measured. The emission intensity is maximum for each current density is normalized so that it all spectra are visible.

The onset of lasing is obvious from the drastic decrease in emission width. Furthermore, the major part of the emission shift is developed under the lasing threshold.

Another significant observation is the fact that the shift does not increase indefinitely. The first two structures exhibit a turning point, beyond which, further increase of the current density does not result in further redshift of the lasing wavelength. There may be several reasons for this behavior. As the structure is distorted under the space-charge electric field that builds up, a portion of the band bending is applied to the barriers. This effectively reduces their opacity and facilitates the carrier transfer in to the active QW either by tunneling or by thermionic emission. Both mechanisms will be discussed later in this chapter.

In summary, using the comparison from LD's with varying $Al_{0.4}Ga_{0.6}As$ barrier thickness, a number of important issues were illustrated. Most important, a Stark shift is possible in the active quantum well, thus tuning the emission of an edge emitting laser diode. A range of optimum barrier thicknesses based on $Al_{0.4}Ga_{0.6}As$ barriers has been demonstrated. Namely, for electron barriers the optimum lies somewhere between 7 and 9nm thick barrier, whereas for holes the corresponding range is between 5 and 7nm. Furthermore, it has been established that there is some saturation mechanism resulting in a maximum achievable shift for each structure.

12.1.3 Stark effect

Solving the Schroedinger equation for the $In_{0.15}Ga_{0.85}As$ active quantum well under an electric field, we obtain an estimate of the corresponding stark shift. This allows us to estimate the net electric field present in the active QW for a measured emission shift. Fig.12.6 shows the active QW stark shift calculated for the structure under investigation.

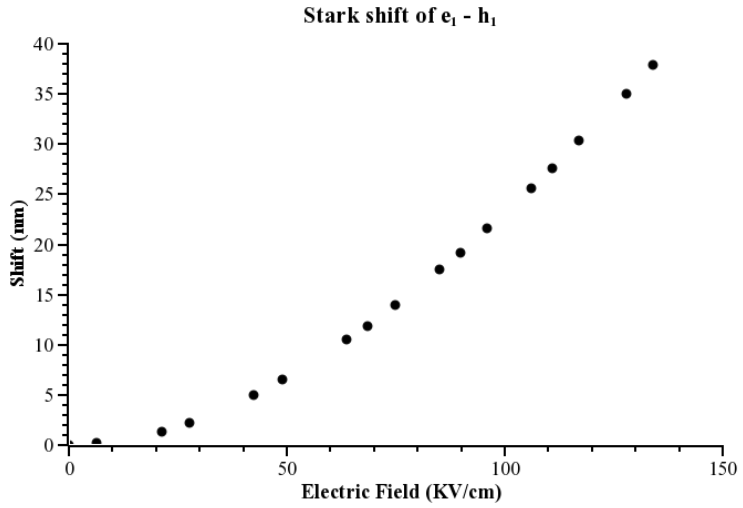

Figure 12.6: Calculated energy difference of e_1-hh_1 vs electric field present in a 12nm wide $In_{0.15}Ga_{0.85}As$ QW.

In order to achieve a shift reaching 30nm, as experimentally observed, a net electric field of about 120KV/cm is necessary. Taking into account the dielectric constant of GaAs this corresponds to a sheet charge of $8.5 \cdot 10^{11}$ carriers/cm^2 in each collection QW. In actuality, since the active QW is providing gain, a carrier density of the order of 10^{12} carriers/cm^2 exists in there as well. These carriers are expected to partially screen the electric field caused by the space charge in the

collection QWs. Given this fact, the actual sheet carrier density accumulated in the collection wells is larger. After presenting the remaining experimental findings, we will return to this calculation to refine our results taking into account the partial screening of the space charge electric field by the carriers in the active QW.

12.1.4 Semi-classical tunneling times

Using a simple semi-classical approach, based on the WKB method described earlier, and assuming that carriers reside at k=0 of the respective collection quantum well, we may obtain a rough estimate for the tunneling time of the electrons through the $Al_{0.4}Ga_{0.6}As$ barrier. This is depicted in fig.12.7 for a range of barrier thickness.

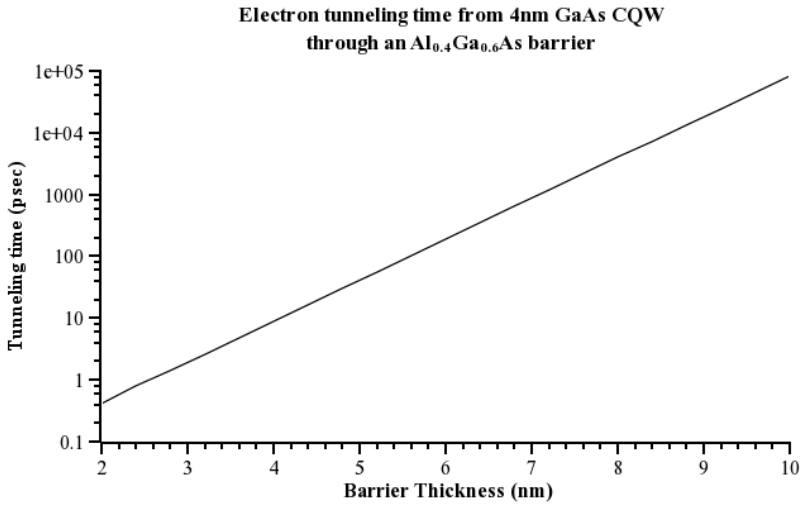

Figure 12.7: Electron tunneling time from an 4nm GaAs QW (CQW) through an $Al_{0.4}Ga_{0.6}As$ barrier. Calculation at k=0 using the semi-classical WKB approximation.

The same calculation can be performed to obtain the heavy and light hole tunneling time through the respective barrier. Note that the collection well for holes is assumed to be 20nm wide. These are depicted in Fig.12.8.

A serious implication arises from the difference in tunneling times between heavy and light holes. The light holes are expected to tunnel through the barrier with a tunneling rate 3-4 orders of magnitude larger than heavy holes. Although this is an *apriori* expected result due to the different effective masses, the implication is that even a small population of light holes is enough to alter the effective tunneling rate. Thus, one has to take into account both tunneling times, weighting them with the relative hole concentrations. This way an effective tunneling time can be calculated for the hole injection through the collection well.

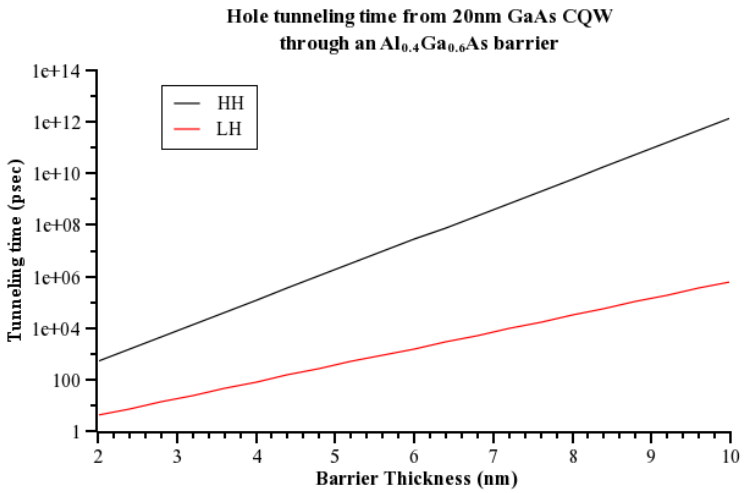

Figure 12.8: Heavy hole (black line) and light hole (red line) tunneling time from a 4nm GaAs QW (CQW) through an $Al_{0.4}Ga_{0.6}As$ barrier. Calculation at k=0 using the semi-classical WKB approximation. Note the large difference in tunneling times due to the different effective masses.

It is expected that at low temperature, the population of the light holes may be negligible as long as the carrier density in the CQW is low enough. The situation changes however when the carrier density is high enough to establish a significant population in the light hole state, or when the temperature is increased to the point where the Fermi tail extends into the light hole state. In reality the situation is even more complicated. A heavy hole state has a clear heavy hole character only for k=0. Due to band mixing effects – which are correctly accounted for by the k·p theory of Kohn and Luttinger – even a heavy hole state has a mixed character for $k \neq 0$. This results in significant changes of the tunneling time as described in [94].

12.1.5 Temperature Behavior

So far, the Stark shift of the emission for edge emitting laser diodes has been investigated at low temperature. Increasing the temperature of operation, a series of phenomena affects the performance of these devices. To begin with, carriers in the active QW are spread over a larger energy range, hence the gain curve is expected to be broader. Accordingly, the gain maximum is suppressed, thus increased carrier densities (i.e. pump current) are necessary to reach lasing. Finally, carriers in the collection wells spread over a larger energy range thus the tunneling time is also expected to change significantly.

Fig. 12.9 depicts the emission shift with current for various temperatures, for the sample with 8 and 10nm hole and electron $Al_{0.4}Ga_{0.6}As$ barriers respectively. The shift is affected at a temperature as low as 130 Kelvin. For 280 Kelvin, there are only 5nm shift remaining.

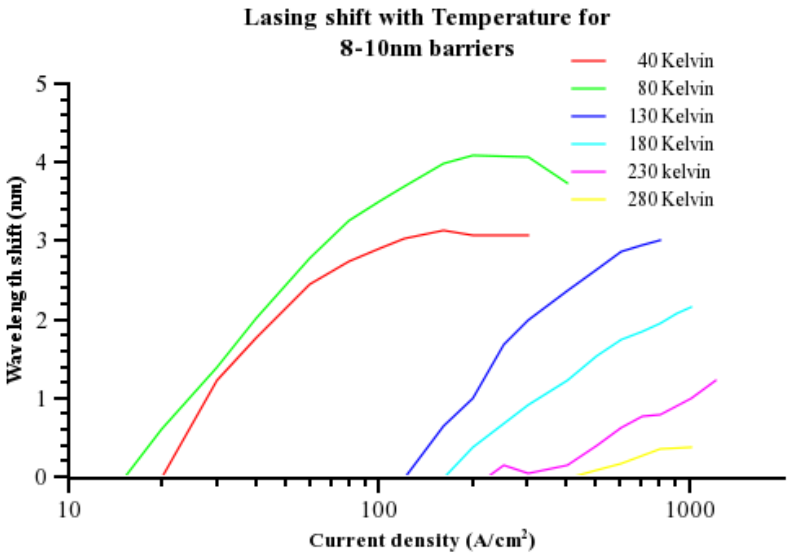

Figure 12.10: Laser operation wavelength shift with pump current density for various Temperature. Besides the dependence from lasing threshold which is expected, the slope of the shift changes for high temperature. This is due to changes in the tunneling time.

More importantly, the lasing shift is shown in fig.12.10. There are two effects that can be seen. First, as the temperature rises, the total stark shift is reducing, especially for T>130Kelvin. This cannot be attributed solely to the increase in threshold current since the effect is also observed below threshold in fig.12.9. Furthermore, the slope of the Stark shift with current decreases with increasing temperature.

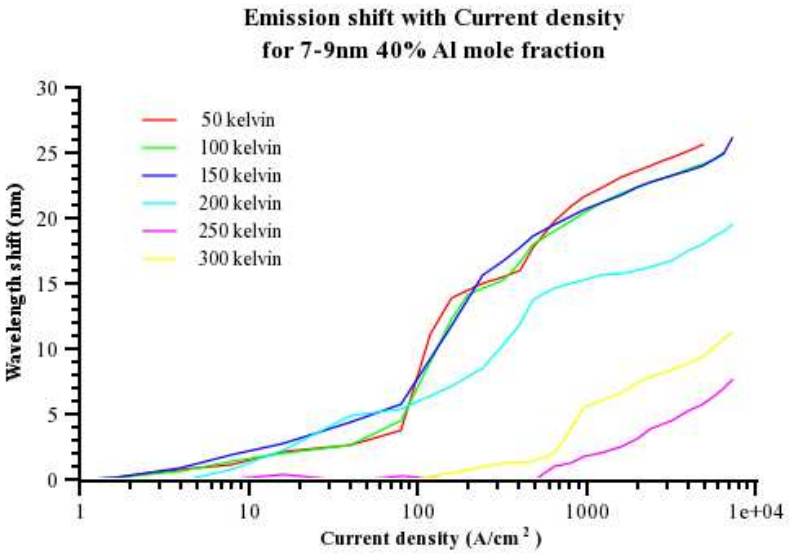

Figure 12.11: EL shift with Temperature for sample 782 with 7 and 9 nm $Al_{0.4}Ga_{0.6}As$ barriers.Sample is based on structure B.

Similar results are obtained for the sample with thinner barriers (namely 7 and 9 nm). The corresponding total emission shift is shown in fig.12.11. Note that this sample was fabricated after

the optimization of the growth, structure design and fabrication described earlier.

As expected, the onset of the Stark shift occurs at higher current density compared to the sample presented in fig.12.9. Up to the highest current used, no saturation effect was observed in the Stark shift. The performance of this device is significantly improved in terms of temperature behavior. Signs of reduction in emission shift are not observed until 200 Kelvin. This may be attributed to the improved barrier material growth sequence described earlier. It should be noted that this device should exhibit a reduced threshold current density as well. However, issues with QW growth resulted in a relatively rough active quantum well as manifested in the FWHM of the low temperature photoluminescence of the active QW. This resulted in increased threshold of the device to a range similar with the unoptimized presented in fig12.10.

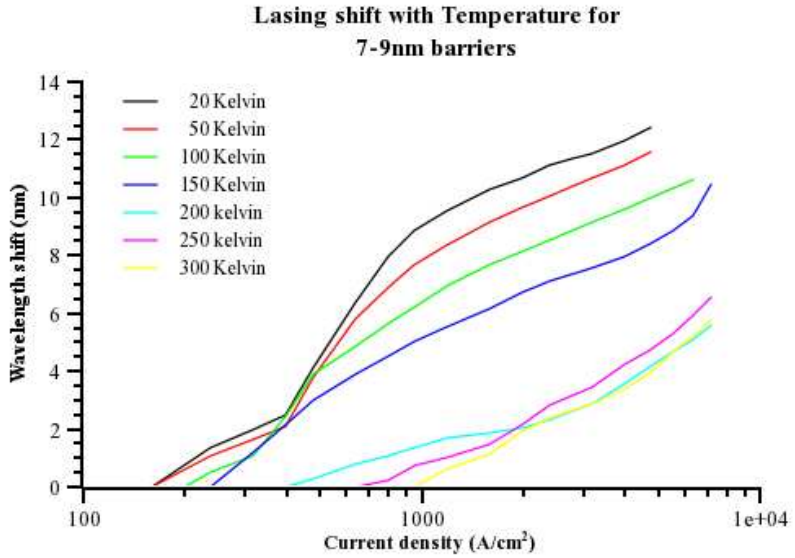

Figure 12.12: Lasing emission shift for sample 782 with current for various temperature. Structure B exhibits no heating effects thus no heating correction is applied.

The corresponding lasing shift is shown in fig. 12.12. We observe a lasing shift in excess of 12nm at low temperature and a room temperature shift of 5nm. Comparing the different barrier thicknesses we observe that the sample incorporating the thinner barriers exhibits reduced total luminescence shift. However, since the current range where the shift is developed is better matched to the lasing regime, the lasing tunability is drastically increased by a factor of 3 (from 4 to 12nm) at low temperature. The situation at high temperature is also improved. A shift as high as 5nm is observed for the second sample. It is important to stress that this is the first observation of significant Stark tuning of the lasing wavelength at room temperature. In order to improve the high temperature behavior of the stark-tunable laser diodes, there is a need to study the temperature effect to the mechanism of the tuning. A possibility that needs to be addressed is whether carriers manage to traverse the barriers by thermionic emission. That would explain the reduction in shift since carriers would not accumulate in the collection quantum wells but rather reach the active QW. To clarify this, we will present the behavior of tunable laser diodes with varying barrier height.

Section:12.2. Barriers with high Al mole fraction

So far the tuning behavior of laser diodes utilizing $Al_{0.4}Ga_{0.6}As$ barriers has been presented. It has already been established, that these barriers perform well at low temperature but gradually lose the Stark shift as soon as the temperature is increased. The logical way to address thermionic emission over the barriers is to increase the barrier height, using higher Al mole fraction material. This would impose a higher energy barrier to the injected carriers and thus provide less temperature sensitivity to the entire injection scheme. To study the effect of Al mole fraction in the barriers, a series of samples was prepared with varying barrier height, as shown in the following table.

Barrier	*e^- thickness*	*h^+ thickness*	*Sample #*
$Al_{0.6}Ga_{0.4}As$	6 nm	4 nm	783
	5.1 nm	4 nm	787
$Al_{0.8}Ga_{0.2}As$	4.5 nm	2.8 nm	784
	4 nm	2.8 nm	785
AlAs	2.8 nm	2.2 nm	786

Table 12.3: Structures grown to study the effect of barrier height to the temperature dependence of the emission shift. All structures are based on waveguide B.

All samples were based on the improved waveguiding structure and were processed in parallel with sample 782 which was presented in the previous section. The results on each sample will be shortly presented and subsequently the results of the comparison with barrier height will be discussed.

12.2.1 Laser tuning from samples with high Al mole fraction

$Al_{0.6}Ga_{0.4}As$ barriers

Using the knowledge gained from the study of $Al_{0.4}Ga_{0.6}As$ barriers, discussed in the previous section, an estimate of the barrier characteristics made using $Al_{0.6}Ga_{0.4}As$ is available.

Following a similar optimization procedure to the one described previously, samples with $Al_{0.6}Ga_{0.4}As$ barriers were prepared. Fig.12.13 shows the emission shift during lasing operation for this sample.

It should be noted that the threshold of these devices is as low as $180A/cm^2$ at room temperature which is close to the optimum. Furthermore, the tuning reaches 20nm for low temperature and reduces to 5nm at room temperature. Compared to fig.12.12 which corresponds to the $Al_{0.4}Ga_{0.6}As$ barriers, there is an increase in maximum shift at low temperature but the high temperature behavior is very similar. It is also worth noting that the matching of the tuning range and the lasing operation regime is better, resulting in a nearly linear dependence of $\Delta\lambda$ vs log(J).

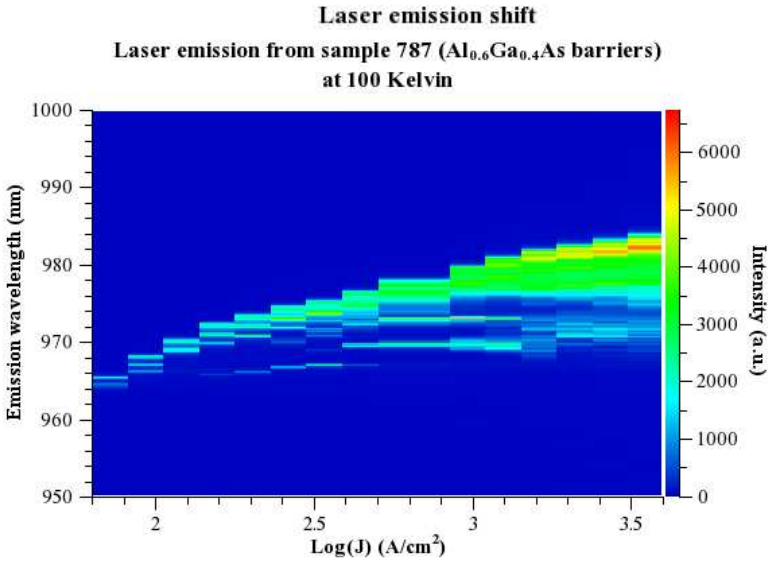

Figure 12.14: Laser emission spectra versus pump current density for sample 787 ($Al_{0.6}Ga_{0.4}As$ barriers).

Fig.12.14 depicts the laser emission spectra for each current density above threshold for a temperature of 100Kelvin.

$Al_{0.8}Ga_{0.2}As$ barriers

Fig.12.15 presents the lasing shift of the sample incorporating $Al_{0.8}Ga_{0.2}As$ barriers. The tuning range may be split in two regions, one below 1KA/cm^2 where the observed tuning is small and a range above 1KA/cm^2 where there is strong tuning. This observation leads us to the conclusion that the barrier thickness in this sample are too thin to effectively accumulate carriers outside the active QW.

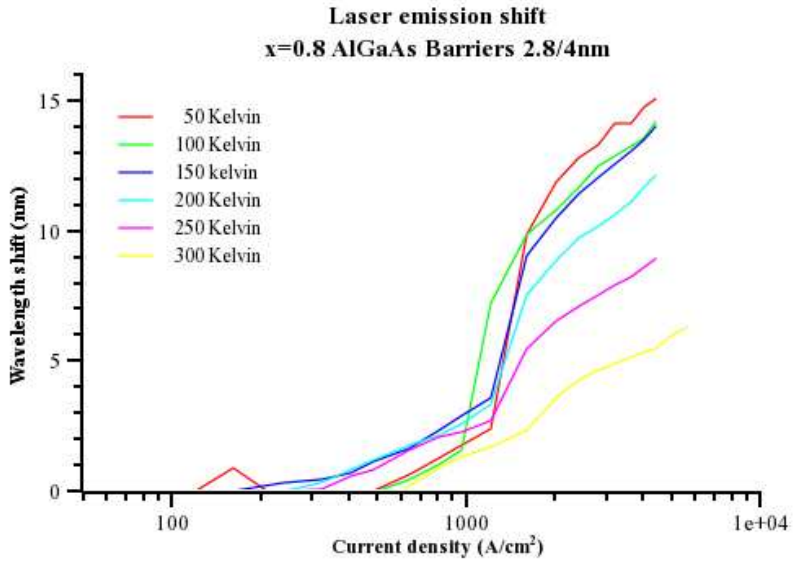

Figure 12.15: Lasing shift for sample 785 versus temperature. Barriers are 2.8 and 4nm $Al_{0.8}Ga_{0.2}As$ for holes and electrons respectively.

As a result, the tuning range occurs at large current density, well above the lasing threshold, even at room temperature. Therefore the maximum recorded range at low temperature is 15nm. At high temperature, the behavior is again similar to the previous samples, reaching a tuning range of 5nm.

AlAs barriers

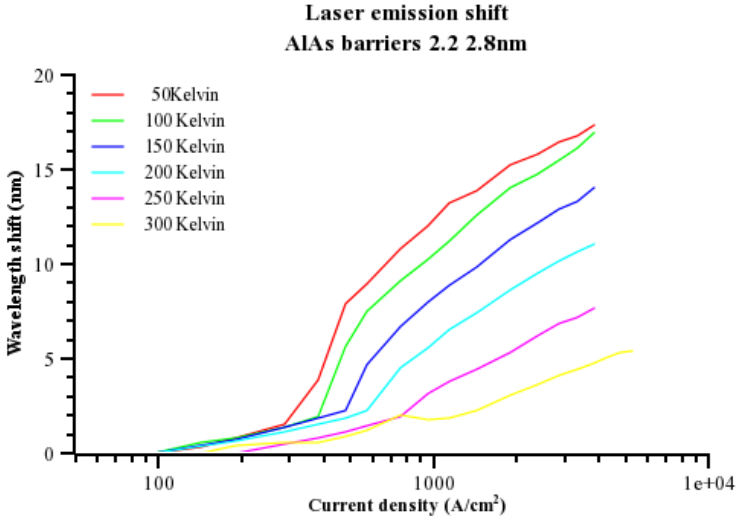

Figure 12.16: Lasing shift for sample 786 for various temperatures. Barriers are 2.2 and 2.8nm $Al_{0.8}Ga_{0.2}As$ for holes and electrons respectively

Finally, the data corresponding to a laser diode with AlAs barriers are presented. Similar behavior compared to the 80% barriers is evident in these devices as well. The optimum tuning range is above threshold. The resulting total lasing shift is approximately 17nm at low teperature

whereas the room temperature behavior is similar to the samples presented before having a shift of 5nm.

Comparison of different Al mole fraction barriers

Using the above results we can compare the tuning behavior differences with barrier height. Fig. 12.17 shows the shift decrease for each of the samples with increasing temperature.

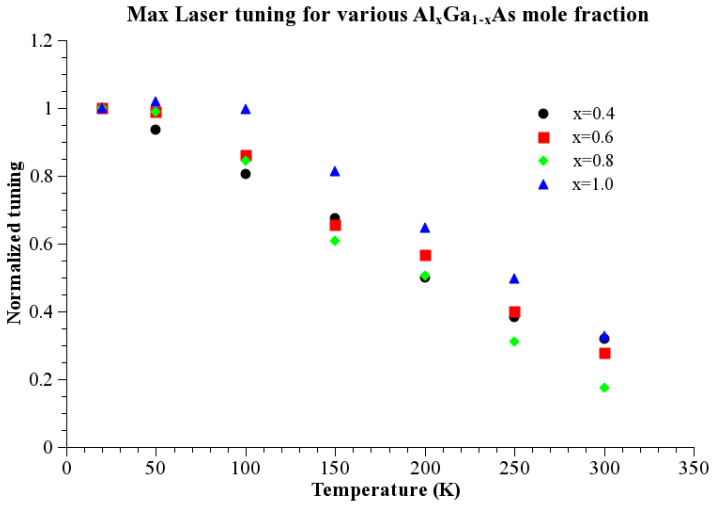

Figure 12.17: Maximum Stark shift during lasing operation with varying temperature for different Al mole fraction in the barrier material. The shift is normalized in order to take into account the different maximum shifts between samples.

By inspection of fig.12.17, there is no significant difference observed in the decrease of tuning with temperature. At 100Kelvin the only sample that exhibits a reduced shift is the one with $Al_{0.4}Ga_{0.6}As$. However at 150Kelvin, the only sample that still shows no significant signs of reduction is the one containing $Al_{0.8}Ga_{0.2}As$. The differences observed here, however, do not reveal a systematic dependence with barrier height which scales with the Al atomic percentage in the fabricated barriers. In fact, the discontinuities that electrons and holes face in front of an AlAs barrier are much larger compared to the thermal energy. Even a defect state in the barrier material, which would reduce the effective barrier height seen by the carriers, would also scale with Al mole fraction. This would also exhibit a Al-mole fraction dependence in fig.12.17 which is not observed.

Having ruled out the possibility that a thermionic emission process is activated, it is necessary to study the tunneling effect itself in further detail. If the tunneling rate changes with temperature, then this is expected to affect the portion of carriers that are accumulated in the collection wells. That would drastically change the electric field created in the device during operation and thus alter the tuning behavior with temperature.

Using the semi-classical tunneling theory described previously, we may estimate the tunneling time for electrons and holes in each structure. These are shown in Table.12.3. It should be noted that we assume that electrons tunnel through the Γ valley of the barrier as suggested already in [105].

Barrier	*e^- T [nsec]*	*hh^+ T [nsec]*	*lh^+ T [nsec]*
$Al_{0.4}Ga_{0.6}As$	15.1	$7.8 \cdot 10^4$	7.14
$Al_{0.6}Ga_{0.4}As$	1.66	891	0.95
$Al_{0.8}Ga_{0.2}As$	3.39	175	0.56
AlAs	1.28	97.9	0.61

Table 12.4: Calculated tunneling times for electrons, heavy holes and light holes at k=0.

As expected, the tunneling time follows the trend existing in the measured data. Namely, the lower the tunneling time, the higher the current needed to obtain a given Stark shift. In fact, the sample which has the lowest light hole tunneling time is the one containing $Al_{0.8}Ga_{0.2}As$ barriers. This is in accordance with the fact that this sample exhibits shifting of the laser emission at the highest current density.

Section:12.3. Theoretical study

12.3.1 Theoretical study of tunneling time

Assuming that carriers relax into the collection QW states and subsequently tunnel through the $Al_xGa_{1-x}As$ barrier, and that carriers have a Fermi distribution inside the collection well, we can calculate the effective tunneling time for each carrier, by taking into account the semi-classical tunneling time for each state and the respective carrier concentration. Especially for holes, the tunneling time is expected to vary significantly as different portion of carriers reside in heavy and light hole states.

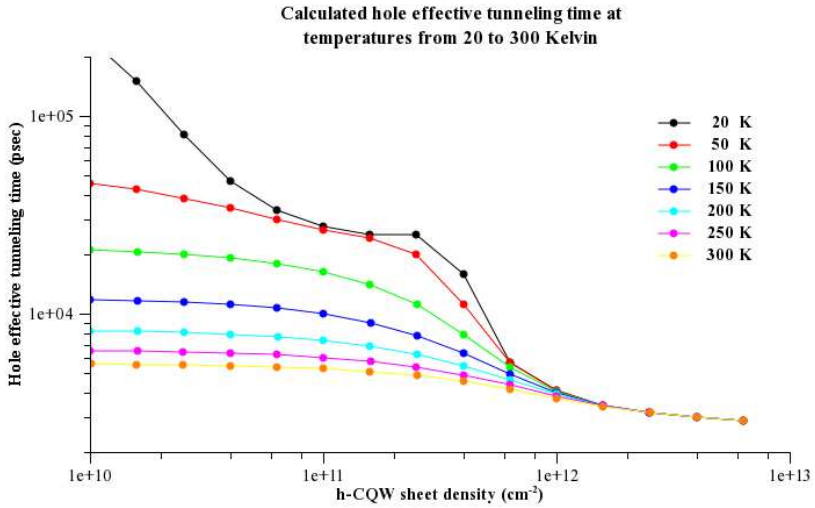

Figure 12.18: Calculated hole tunneling time from an 20nm GaAs through a 7nm thick $Al_{0.4}Ga_{0.6}As$ barrier.

Fig.12.18 shows the calculated weighted hole tunneling time for a 7nm thick $Al_{0.4}Ga_{0.6}As$ barrier. The tunneling time decreases with increasing collection QW carrier density. The heavy hole states reside closer to the band edge QW, as a result, especially at low temperature, they are populated first. As the carrier density increases in the QW, the light hole states become populated as

well. Since the light hole tunneling time is a few orders of magnitude smaller, the impact on the total effective tunneling time is shown as an abrupt decrease in total tunneling time. As soon as the temperature increases, the Fermi probability extends at higher energies, enough for the light hole population to become significant regardless of carrier density. As a result, the effective tunneling time reduces drastically with carrier density and is also strongly temperature dependent.

Performing the same calculation for the AlAs barrier we obtain fig. 12.19.

Comparing fig.12.18 with fig.12.19 we see that this temperature dependent reduction is observed regardless of barrier height. Indeed this is an expected result. The main factor is the relative heavy and light hole population and their respective tunneling times. The relative density only depends on the band states of the collection QW whereas the tunneling times are always 2-3 orders of magnitude different due to the different effective masses.

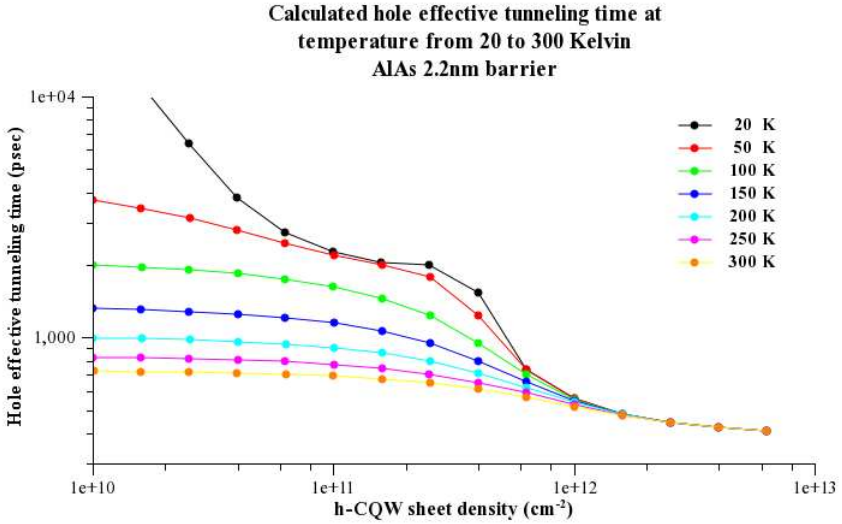

Figure 12.19: Calculated hole tunneling time from a 20nm GaAs through a 2.2nm thick AlAs barrier.

As far as low temperature behavior is concerned, the impact on device performance is that increasing the carrier density will allow carriers to tunnel through the barrier at a faster rate, thus the associated shift will not increase accordingly, leading to the observed saturation. As far as high temperature operation is concerned, it is expected that for the same current, a reduction in emission shift (compared to low temperature) will be observed, due to the reduced accumulation of charges in the collection QW. In fact this mechanism is found to be independent of barrier height, which is in accordance to our experimental findings.

12.3.2 Extracting tunneling times from experimental data

At a given current density, the carriers that actually tunnel through each barrier are directly proportional to the current density flowing through the device. Assuming that all carriers recombine in the active quantum well, and ignoring thermionic processes, we reach the conclusion that the current flowing through the device is equal to the tunneling current flowing through each barrier.

Furthermore, using the measured total emission shift we can obtain an estimate of the electric

field existing in the structure for each current. Knowing the electric field, and assuming that equal density of electrons and holes exist in the corresponding collection QW's (balanced structure), we can calculate the carrier density accumulated in each collection quantum well using the simple parallel plate capacitor equation.

Combining these results, we obtain an estimate of the carrier density exactly before the barrier (in the collection QW) and an estimate of the number of carriers that actually tunnel through the barrier. Calculating the effective tunneling rate from these data is trivial. This way we can obtain a rough experimental estimate of the tunneling rate for each current density at a given temperature. The simplistic picture described by fig.12.6, overestimates the actual electric field applied by the accumulated charges in the collection QW's. This is because no screening effects from the carriers that reside in the active QW is taken into account. However, a rough estimate of the active QW population may be calculated from gain data. As discussed in our laser diodes analysis so far, to reach threshold, a modal gain of approximately $10cm^{-1}$ is needed. This translates to a QW gain in the order of $300cm^{-1}$ assuming a confinement factor of 3.5%. Using a self-consistent Schroedinger – Poisson calculation we can associate the collection QW population with an improved estimate of screened potential existing in the active QW in order to obtain the desired gain.

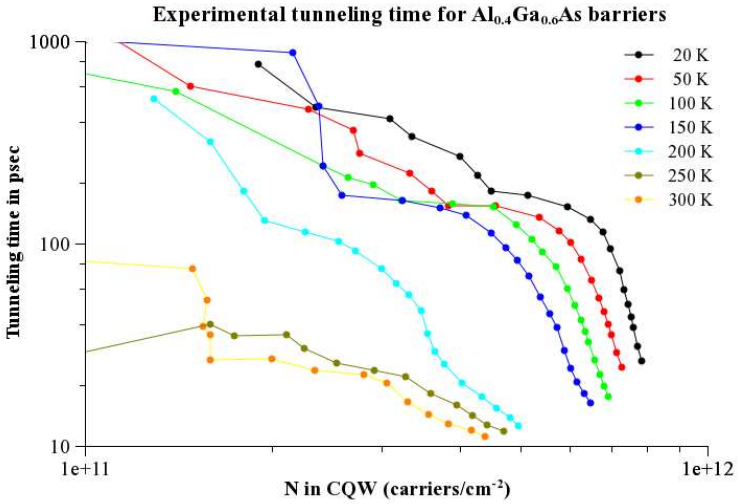

Figure 12.20: Experimentally estimated tunneling time for sample 782 (Al0.4Ga0.6As barriers as a function of collection QW carrier density.

The resulting experimentally estimated tunneling time for sample 782 ($Al_{0.4}Ga_{0.6}As$ barriers) is shown in fig.12.20. comparing the low temperature tunneling times shown with the theoretical calculations depicted in fig.12.18 we observe a similar trend with increasing carrier density. To our knowledge this is the first experimental estimation of carrier tunneling time as a function of carrier density in such a semiconductor system. Furthermore, the temperature change observed in the experimental data shows a decrease in the tunneling time, even for low carrier density in accordance with our theoretical calculations. The discrepancy observed between high density, high temperature experimental data can be explained if we take into account the screening effects from the active QW carriers which have a higher density at high temperature. This is expected to shift the experimental

tunneling curves towards higher collection QW carrier concentrations.

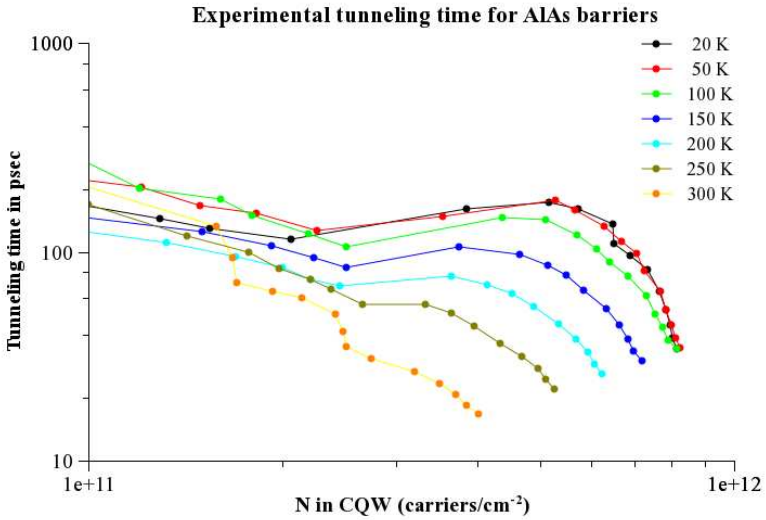

Figure 12.21: Experimentally estimated tunneling time for sample 786 (AlAs barriers) as a function of collection QW carrier density.

Similar results are obtained from the sample with AlAs barriers tunneling time which is shown in fig.12.21. The tunneling time is again reducing with collection QW carrier density as well as temperature, following qualitatively the behavior theoretically predicted in fig.12.19. A significant difference in tunneling time behavior between the two samples is exhibited for high temperature data. As observed, the $Al_{0.4}Ga_{0.6}As$ barriers show evidence of tunneling time reduction at high temperature even for low carrier densities. On the contrary, the sample containing AlAs barriers shows no such behavior. On a final note, the experimentally estimated carrier tunneling times are found to be smaller than the theoretically calculated ones. This may be partially explained taking into account the the simple semi-classical model used overestimates the tunneling time as discussed in [106], and the fact that since a larger collection QW carrier density is necessary to obtain the same Stark shift in a screened structure, the calculated tunneling times are expected to increase accordingly.

Although a simple picture to describe the electric field with collection QW carrier density was used, the main characteristics of tunneling time dependence from carrier density as well as temperature are successfully deduced from the experimental data.

Section:12.4. Conclusions

In summary, we have successfully developed a laser diode structure that is able to sustain a dynamic electric field in the active quantum well. In fact electric field values as high as 200KV/cm where experimentally observed.

Furthermore, we have, for the first time fabricated gain tunable laser diodes using the quantum confined stark effect in the active quantum well. A maximum tunability of 20nm at low temperature was demonstrated. In conclusion, tunable laser diodes were fabricated using this concept that perform even at room temperature, providing however a reduced room temperature tuning range of

5nm. Concerning the intermediate temperature regime, devices that operate without significant loss of tuning ability were demonstrated up to 200Kelvin.

This category of broad wavelength tuning is expected to be fast due to the small characteristic times involved in their operation. This leads to potentially interesting applications where broadly tunable and high tuning speed laser devices are necessary.

The effect of barrier height and barrier width was investigated. Experimental findings suggest that barrier height is not responsible for high temperature reduction of tuning behavior. On the contrary, the effect of hole tunneling is shown to drastically alter the tunneling behavior of the barriers used to achieve the space charge electric field. In fact, the tuning reduction with temperature could be attributed to the drastic reduction of tunneling time with increasing temperature.

Part IV: Appendices

Appendix A. Design and fabrication of the current pulse generator

As described in the text, a need for a high speed rectangular shaped current pulse was evident to correctly perform measurements of the laser diode devices studied in this thesis. Since such an equipment was not available, and the cost to buy a measuring station was prohibitive, it was necessary to create such a current pulse generator in house. This appendix describes in detail the design logic and the modules that comprise the fabricated current pulse generator. All design and circuit fabrication was performed by the author.

A source which is capable to provide current pulses, rectangular in shape (constant current) and short enough so that the device does not heat up was designed. Furthermore, this pulse has to be abrupt (turn on/off time) so that the measured response corresponds to the main part of the pulse only. Subsequently, the current is turned off for a long time to allow the device to dissipate heat. The typical characteristics of such a pulse is depicted in the following table:

Parameter	*Typical value*
Current I_{ON} (mA)	0-2000
Pulse width [PW] (nsec)	200-1000
Rise Time [10-90%] (nsec)	20-50
Fall Time [90-10%] (nsec)	20-50
Duty Cycle (%)	0.1-1%
Current regulation (ΔI_{ON})	<1%
DC current I_{DC}	1μA - 100mA
DC current accuracy ΔI_{DC}	<1%

Table A.1: Specifications for a current source to perform Electrical pumping measurements of Laser Diodes

Conversely, at low current levels, heating is not an issue. Furthermore, optical output is very low. Pulsed pumping would offer nothing in this regime on the contrary given the fact that average optical power is divided by the duty cycle factor, it would be necessary to measure a minute optical signal rendering measurements at very low current impossible. For this reason it is equally important to be able to supply a small but controlled DC current to the device under test as well.

To meet the described specifications, a hybrid (analog+digital) electronic circuit was designed

[66] and fabricated. To design the circuit, the program PSPICE was used to simulate each module separately and finally PROTEL© [67] was used to design the printed circuit boards. All boards were fabricated in the lab using standard 2 sided copper plated photo-resist coated commercially available boards and UV-lithography technique. As depicted in fig.A.1 the basic modules comprising a full-featured pulsed current source are the following:

- DC current source (Voltage controlled DC current output)
- AC current control module (DC current source + modulating network + current amplifier)
- Timing circuit (Voltage controlled rectangular pulse generator)
- Measuring module (measures voltage and current on the device)
- Digital control unit (provides auto-control voltages and mode of operation)
- Interface Unit (LCD, keyboard, RS-232 interface and analog input of control parameters)
- Power supply (provides all voltages necessary for operation)

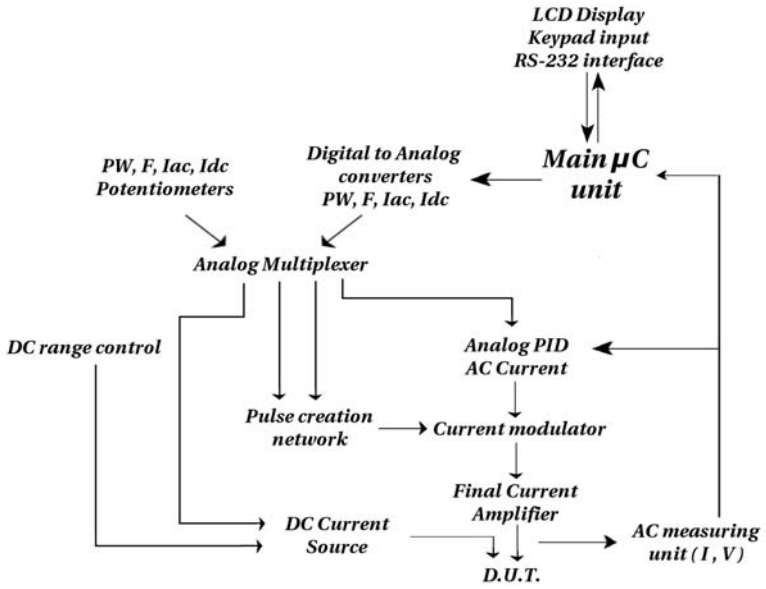

Figure A.1.: The topology of the basic modules comprising the current source design implemented for the needs of laser diode measurements throughout this thesis.

In the following subsections the schematic of each module along with a brief description of the operational logic will be described.

Timing circuit

A NE566 multi vibrator IC is connected in astable operation configuration. The frequency of operation is controlled by varying the charge voltage of the RC network. Trimming R1, R6 and R7 defines the minimum and maximum frequency attainable from the circuit. The output of this IC, edge triggers a fast monostable multi vibrator chip (74HC221). The pulse width of the later is controlled by a second charge voltage network. Resistors R10, R9 and R8 are trimmed to obtain the

desired PW range.

In total, two input voltages are used, (V_f and V_{pw}) ranging from 0 to 5Volts controlling the frequency and pulse width of the timing circuit respectively. Using this circuit we are able to obtain F = 1-10KHz and pulse width PW=200nsec – 2μsec.

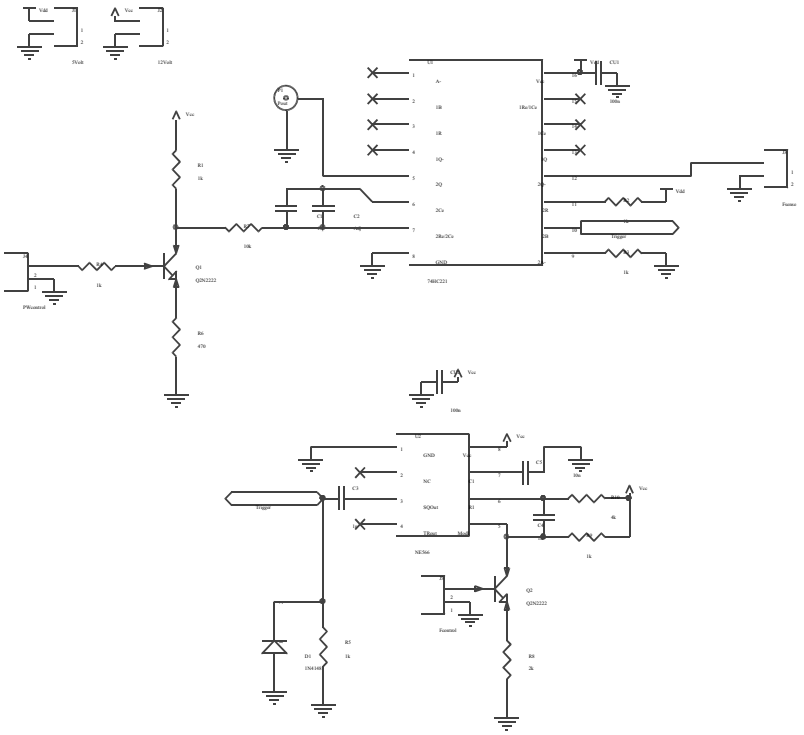

Figure A.2.: Timing network schematic.

AC and DC current source

The circuit design that provides the DC component as well as the AC seed current are very much alike. As shown in fig.A.3 both consist of an analog PID network.

DC current source

The top circuit in fig.A.3 depicts the DC current source. There is a relay that connects/disconnects the resistor R20 in parallel with R21 changing the sensitivity of the feedback circuit. When the R20 is not connected the circuit operates in high sensitivity mode, limiting the range of the output to a few mA, thus increasing the accuracy to 1μA. On the contrary, connecting R20 in parallel with R21 changes the range to 0-100mA sacrificing accuracy. U1 acts as a voltage comparator and provides U2, which is an integrator network, with the error in measurement. The entire circuit acts as an analog PI circuit matching the output to the requested value.

AC current source

The AC current source module provides a continuous current that is subsequently modulated to achieve pulsed operation. The circuit logic (bottom circuit in fig.A.3) is the same as the DC module. U4 and U5 act as the PI components, the feedback however is provided by the measurement module directly from the output of the entire device. This way the transfer characteristics of the circuit including the final amplifier stage are canceled out achieving a linear control of the AC current component. The measurement module will be described in the following sections.

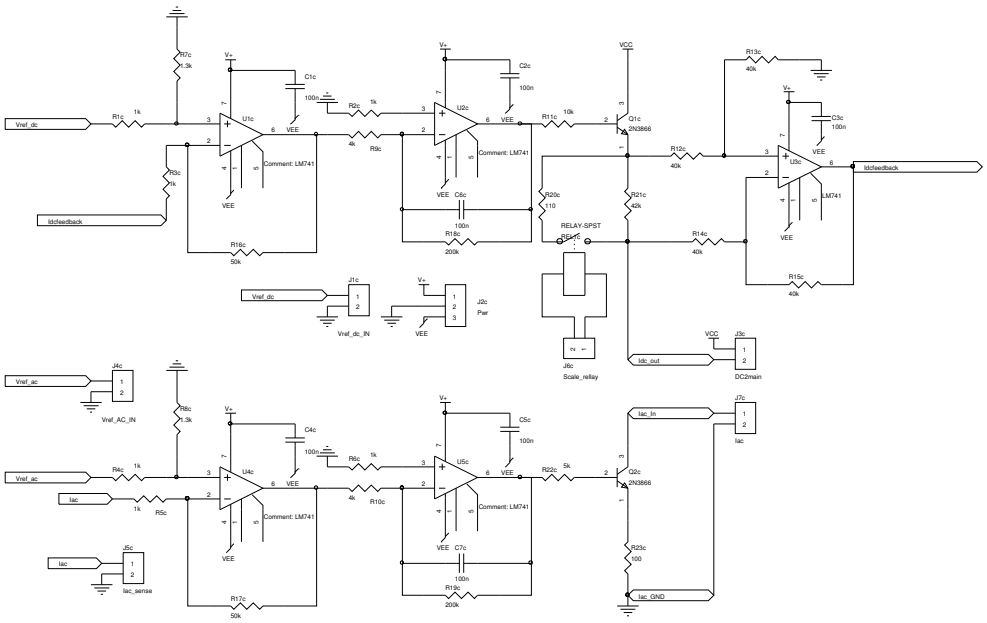

Figure A.3.: Analog PID control circuit schematic.

Final current stage, modulation and amplification

Fig.A.4 depicts the final current stage. The inverting gate U1 drives a fast switching transistor Q6. This acts like a shunt to ground when conducting. When the transistor switches off, the current is directed through the rest of the circuit, reaching the final amplifier.

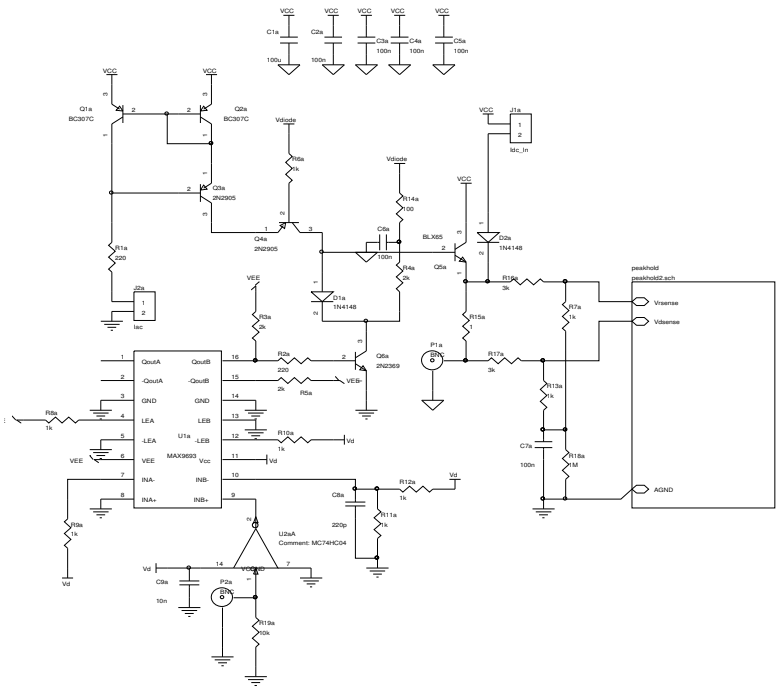

Figure A.4.: Final drive stage. Current modulating network and final amplification stage.

The final amplification stage is Q5 (2N3866). Amplified current flows through R15 (1Ω), which is the current sensing resistor, and then through the device. The rest of the circuit is a 1:1 current mirror. Q1 through Q3 form a current mirror at the input of the control current and are necessary to obtain isolation between the control circuit and the final stage (high voltage swings from the modulating network). Q4 acts as a second isolation step keeping the voltage on the current mirror close to the voltage measured from the device. This suppresses transients on the current mirror and thus the final output. Finally, the DC current connection is protected using a fast switching diode so that current does not flow backwards during the pulse on status.

Measurement unit

As described so far, in order for the above circuit parts to function correctly, the current and the voltage on the device have to be measured when the pulse is applied. The circuit shown in fig.A.5 is used to perform this task.

Input from the p side of the device (V_{IN}) and from the shunt resistor R_{sh}=1Ω (V_{sh}) are directed to a fast high voltage op-amp (MAX 9693) in voltage follower configuration. This is necessary to isolate the final stage of the current source from the rest of the measuring setup. Subsequently, there are two analog, peak sample and hold networks. One to obtain the maximum of the voltage on the device and one to obtain the maximum of voltage on the shunt resistor. Following is another isolation stage (voltage follower) to increase the fan-out of the sample and hold network. The output of this circuit is one voltage (1:1) V_{LD} and one voltage V_I (1mV/mA) for the current flowing during pulse application through the device.

As discussed earlier, both outputs are necessary to drive the rest of the electronics correctly.

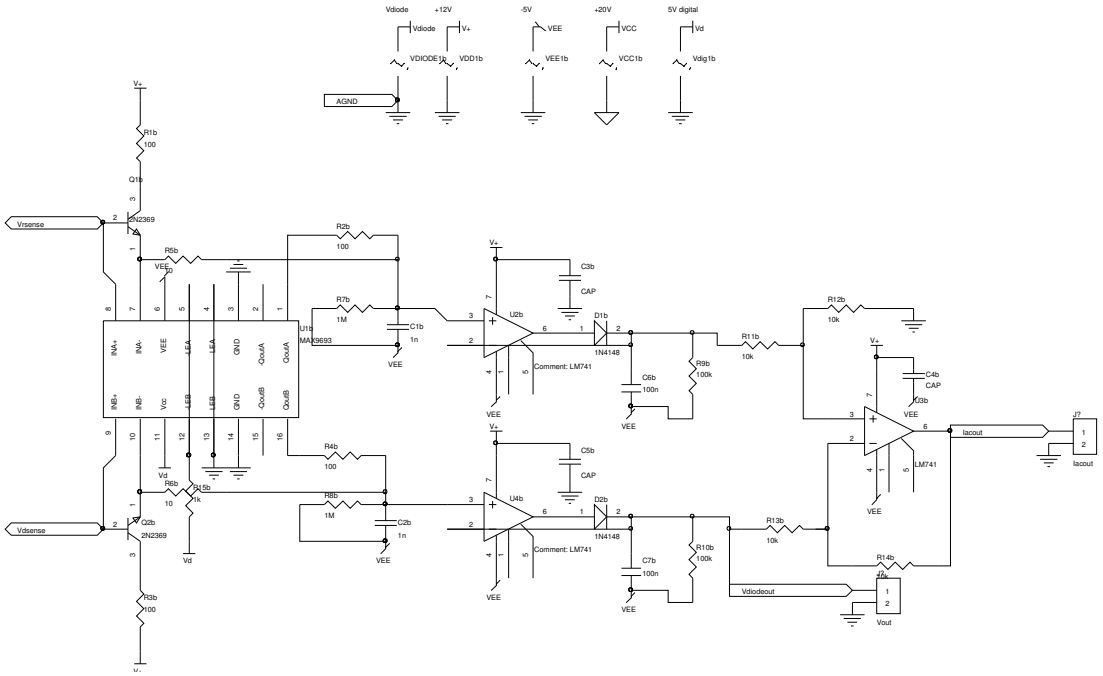

Figure A.5.: 2-channel sample and hold network. Necessary to measure the voltage and current on the device during the fast pulse operation.

Interface

In order to be able to control the current source and read out the performed measurements, an interface was designed. The simplest way to control the instrument would be by using 4 potentiometers which set the corresponding parameters, namely pulse width, repetition rate, DC and AC components of the current source. Of course this is of little interest if there is no way to know the values of each parameter. That is why a more sophisticated interface was designed. The schematic shown in fig.A.6 is the circuit controlling a liquid crystal display (LCD), a keyboard and an RS-232 connection allowing for measurement readout and setting either visually or through a PC.

An ATMEL AVR8515 [107] is used as the core of the interface. At the right handside of Fig.A.6 there is the connector to the LCD and transistors Q6-Q10 that control the LCD backlight intensity through a menu on screen. On the left top there is a MAX232 which translates 0-5Volts signal from the μCPU to ±9Volts for RS-232 compliance. Finally on the bottom, transistors Q1-Q5 which interface the keyboard to the μCPU.

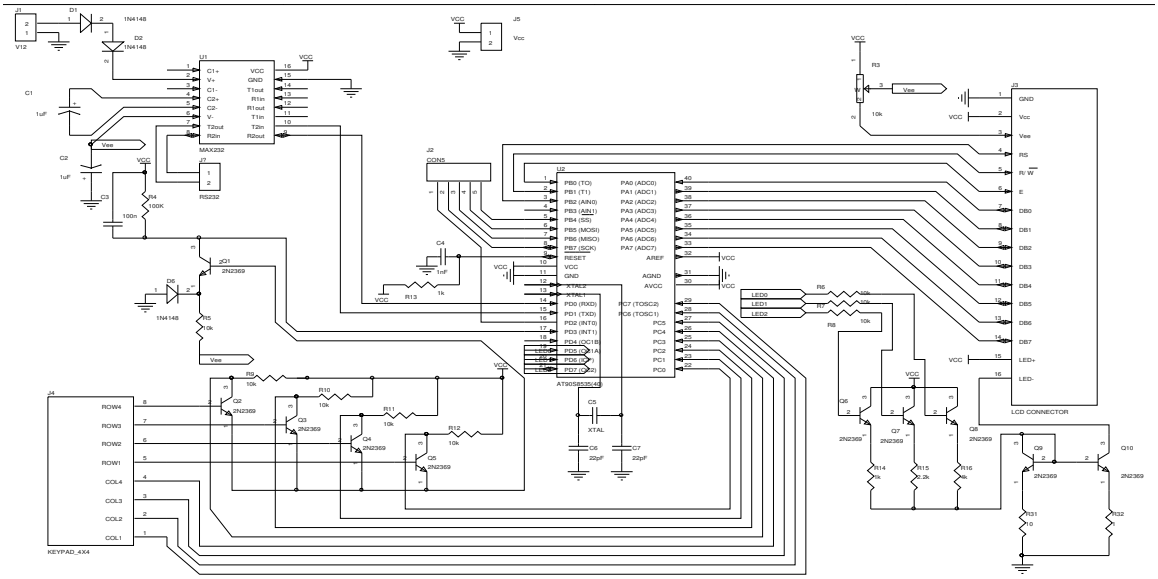

Figure A.6.: LCD, Keyboard and RS-232 interface

To be able to control the current source through the μCPU, 4 analog voltages are required. These are provided through the circuit depicted in fig. A.7. There are four digital to analog (DA) converters (MAX545) followed by four 741 in voltage follower topology to enhance fan-out of each channel.

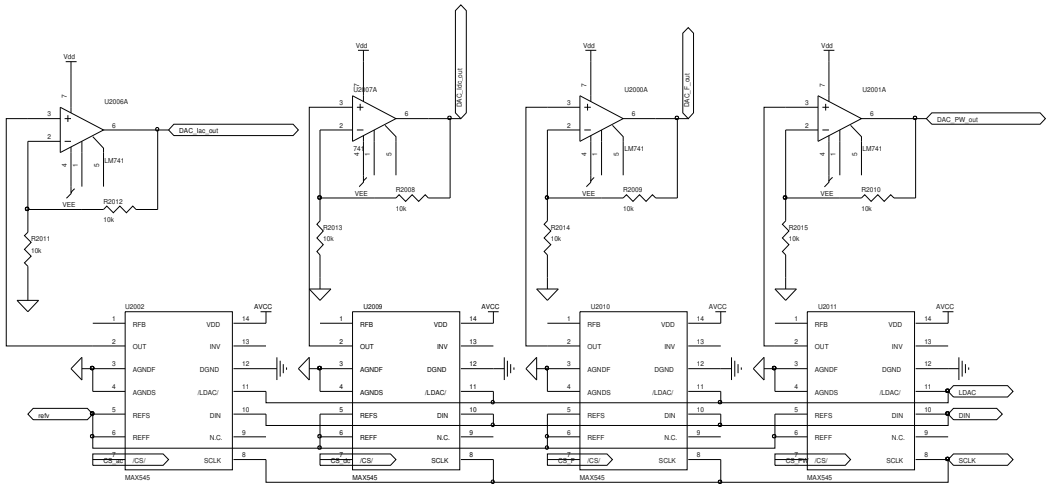

Figure A.7.: 4 channel digital to analog converter. Enables μCPU control of the analog components.

Finally in order to control whether the potentiometers or the DA converters will actually control the current source, there is an analog multiplexing circuit shown in fig. A.8 controlled by the main μCPU. This is realized using four HEF4066 IC's working complementarily in pairs. When the two are in low resistance state the other are in high resistance thus switching between analog or digital inputs.

To conclude the design, the main μCPU control circuit is shown in fig. A.9. This is responsible for the measurement of I_{AC} and V_{LD} as well as control of the analog circuit. All interaction to and

from the interface is performed through the ISP protocol. It should be noted that it was a design

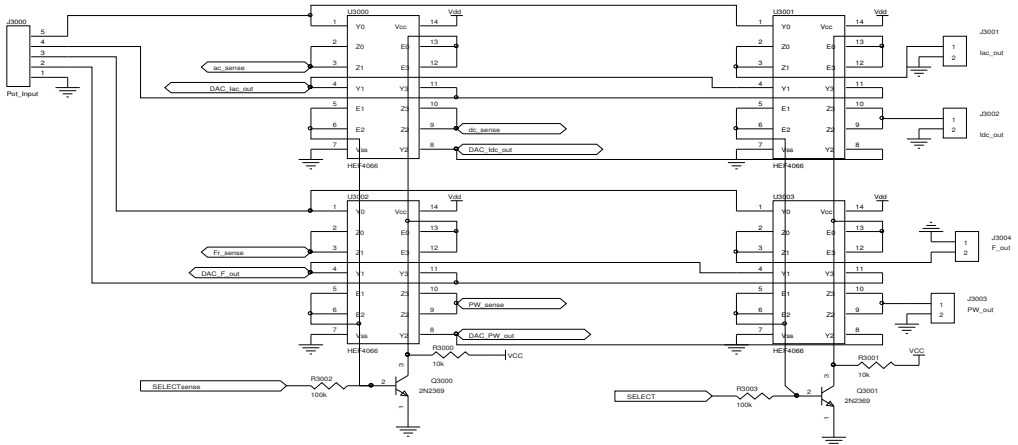

Figure A.8.: 4 channel analog multiplexer.

choice to implement separately the interface from the control unit. The primary consideration in this solution was the fact that the interface board is rather noisy (LCD and MAX232) whereas the main board contains analog parts and is thus sensitive to noise. This also enables for future versions with different power supply for analog and digital components to be added to the design without further work.

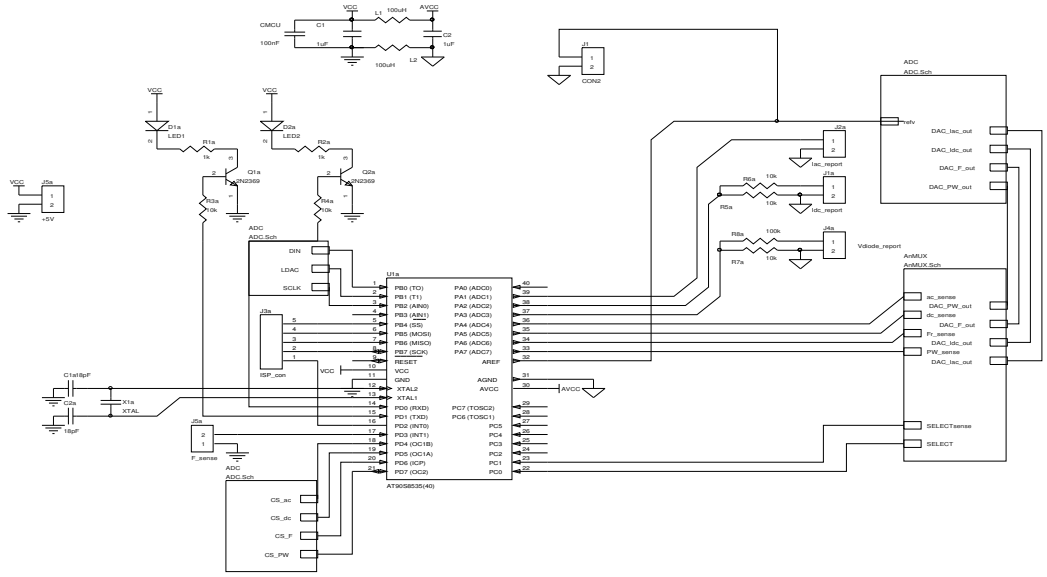

Figure A.9.: Main μCPU control board. This is responsible to control the entire analog part and measure Actual current and voltage on the device.

Power supply

In order for the modules mentioned to operate properly it is necessary to provide the following regulated voltages ±5Volts, 12Volts and 20Volts. These were realized using LM78XX regulators. The schematic of the power supply is depicted in the fig. A.10. All outputs are fused and each voltage has enough connectors to supply all the necessary modules.

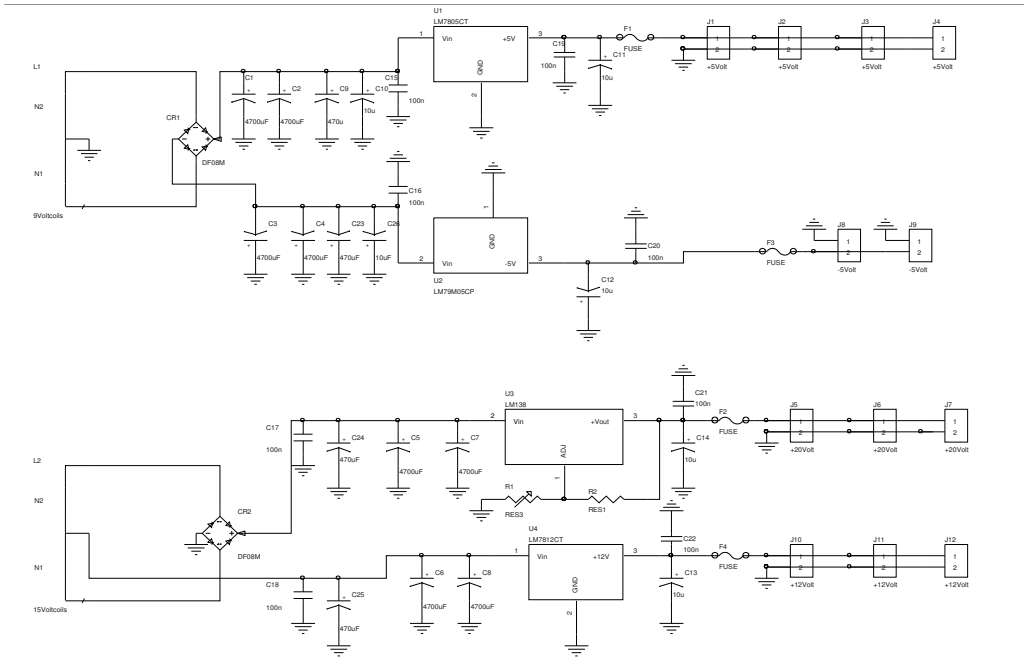

Figure A.10.: Power supply schematic.

Future improvements

Although the current source has been successfully designed, fabricated and used in this project, there are a few minor issues that could drastically improve the overall performance of the apparatus. The main problem encountered was when switching off the main power. The 5Volt power supply network has a large power consumption. That is because most electronics are powered using 5Volts. This led to the following situation: The 5Volt supply would deplete in a small amount of time (msec) whereas the high voltage (20Volts) which has no consumption because pulse is off would still be applied to the circuit. This situation makes the circuit release a high current pulse through the output for a long uncontrolled period of time. The modulating circuit no longer works and allows current through the final amplification transistor. This situation can be addressed in two possible ways: Either by redesigning the power supply so that the 5Volt supply persists until the 20Volt supply is depleted, or by redesigning the triggering circuit of the modulation network so that the modulating transistor is not in high resistance state when the 5Volt supply fails.

Finally, even though the two-board design was implemented to separate noise sources from the analog control board, there were some noise issues coming from the crystal oscillators of the two μCPU's and the LCD (which also has an XTAL oscillator built in). These were reduced drastically by adding decoupling capacitors close to the power input on the respective boards.

Summary

Overall, a pulsed, computer controlled, fully automatic current source was developed and fabricated successfully. The new setup is able to provide current pulses as short as 200nsec with a repetition rate as high as 10KHz. Furthermore, current range from 0-2A is possible as long as the

resistance of the device is such that V_{diode} does not exceed 20Volts when the pulse is on. Finally, DC component of the current may independently be applied in the range of 0-100mA with accuracy better than 1μA at the μA range. The fabricated current source was successfully used to complete all pulsed measurements presented throughout this thesis.

List of references

1: WWW: en.wikipedia.org/wiki/Laser_diode

2: R.N.Hall, G.E.Fenner, J.D.Kingsley and T.J.Soltys, "*Coherent light emission from GaAs junctions",* **Phys.Rev. Lett.**9 pp.366-368 ,1962

3: M.I.Nathan, W.P.Dumke, G.Burns, F.N.Dill and G.J.Lasher, "*Stimulated emission of radiation from GaAs PN junctions",* **Appl. Phys. Lett**1 pp.62-64 ,1962

4: F.H.Dill, "*Continuous stimulated 0.84um emission of GaAs diodes at temperatures of 2K",* pp. , 1963

5: H.Kroemer, "*A proposed class of heterojunction lasers",* **Proc. IEEE**51 pp.1782-1784 ,1963

6: Zh.I.Alferov and R.F.Kazarinov, "*",* pp. ,1963

7: I.Hayashi, M.B.Panish and P.W.Foy, "*A low threshold room temperature injection laser",* **IEEE J.Quantum Electron.**QE-5 pp.211-212 ,1969

8: J.P.van der Ziel, R.Dingle, R.C.Miller, W.Wiegmann and W.A.Nordland, "*Laser oscillation from quantum states of very thin GaAs/AlGaAs multilayers",* **Appl.Phys.Lett.**26 pp.463-465 , 1975

9: H.Soda, K.Iga, C.Kithara and Y.Suematsu, "*GaInAsP/InP surfasce emitting injection lasers",* **Jpn. J.Appl.Phys**18 pp.2329-2330 ,1979

10: S.Nakamura, M.Senoh, S.Nagahama, N.Iwasa, T.Yamada, T.Matsushita, H.Kiyoku, "*InGaN-based Multi-Quantum Well structure laser diodes",* **Jpn.J.Appl.Phys.**35 pp.L74-L76 ,1996

11: P.I.Kuindersma, W.Sheepers,J.M.H.Cnoops, Tunable 3-section strained MQW PA-DFB's with large single mode tuning range, 1990

12: F.Delorme,G.Terol,H. de Bailliencourt, "*",* **IEEE J.Sel.Top.Quantum Electron.**5 pp.480 ,1999

13: C.K.Cardiner,R.G.S.Plumb,P.J.Williams and T.J.Reid, "*",* **IEEE J.Proc.Optoelectronics**143 pp.24-30 ,1996

14: S.A.Wood,R.G.S.Plumb,D.J.Robbins,N.D.Whitbread and P.J.Williams, "*",* **IEEE Proc.Optoelectron.**147 pp.43-48 ,2000

15: D.C.Reid,D.J.Robbins,A.J.Ward, "*",* **Proc. OFC**ThV5 pp. ,2002

16: F.Yang, P.Blood and J.S.Roberts, "*Edge-emitting quantum well laser with Bragg reflectors",* **Appl.Phys.Lett.**66 pp.2949-2951 ,1995

17: M.J. Coupland, K.G. Mamdleton and C.Hilsum, "*",* **Phys.Lett**7 pp.231 ,1963

18: "*Single Frequency Semiconductor Lasers*" by:J.Buus published by: SPIE 1991

19: "*Tunable laser diodes and related optical sources*" by:J.Buus, M.C. Amann, D.J. Blumenthal

published by: Wiley Inter-science 2005

20: R.A.Soref, J.P.Lorenzo, "*All-Si active and passive guided-wave components for λ=1.3 and 1.6μm",* **IEEE Journal of Quantmu Electronics**22 pp.873-879 ,1986

21: B.Bennet, R.Soref and J.DelAlamo, "*Carrier-induced change in refractive index of InP,GaAs and InGaAsP",* **IEEE Journal of Quantum Electronics**26 pp.113-122 ,1990

22: J.P.Weber, "*Optimization of the carrier-induced eff. index change in InGaAsP waveguides",* **IEEE Journal of Quantum Electronics**30 pp.1801-1816 ,1994

23: M.Okuda and K.Onaka, "*Tunability of DBR laser by modulating refr. index in corrugated waveguide",* **Japanese Journal of Applied Physics**16 pp.1501-1502 ,1977

24: N.Susa and T.Nakahara, "*Enhancement of change in the refractive index in an asymetric quantum well",* **Appl.Phys.Lett.**60 pp.2457-2459 ,1992

25: N.Susa, *Electric-field-induced refr. index changes in InGaAs-InAlAs asymetric CQW*, 1995

26: M.Oberg, S.Nilson, T.Klinga and P.Ojala, "*A 3-electrode DBR laser with 22nm wavelength tuning range",* **IEEE Photonics Technology Letters**PTL-3 pp.299-301 ,1991

27: T.L.Koch,U.Koren, R.P.Gnal, C.A.Burrus and B.I.Miller, "*Continuously tunable 1.5μm MQW GaInAs/GaInAsP DBR lasers",* **Electronics Letters**24 pp.1431-1433 ,1988

28: F.Delorme,S.Grosmaire,A.GLoukhian and A.Ougazzaden, "*High power operation of widely tunable 1.55μm DBR laser",* **Electronics Letters**33 pp.210-211 ,1997

29: N.K.Dutta, A.B.Piccirilli, T.Cella and R.L.Brown, "*Electronically tunable distributed feedback lasers",* **Appl.Phys.Let.**48 pp.1501-1503 ,1986

30: P.I.Kuindersma,W.Scheepers,J.M.H.Cnoops, P.J.A.Thijs et al, Tunable 3-section strained MQW PA-DFB's with large single mode tuning range, 1990

31: M.C.Amann,S.Illek,C.Schanen and W.Thulke, "*Tunable twin-guide laser: A novel LD with improved tuning performance",* **Appl.Phys.Lett.**54 pp.2532-2533 ,1989

32: M.C.Amann and W.Thulke, "*Continuously tunable LD: Longitudinal vs transverse tuning scheme",* **IEEE J.of Select. Areas in Comm.**8 pp.1169-1177 ,

33: S.Sakano,T.Tsuchiya,M.Suzuki, S.Kitajima and N.Chinone, "*Tunable DFB laser with a striped thin-film heater",* **IEEE Phot.Technol.Lett.**4 pp.321-323 ,1992

34: T.Kameda, H.Mori, S.Onuki, T.Kikugawa,Y.Takahashi,F.Tsuchiya and H.Nagai, "*A DBR laser employing passive-section heaters with 10.8nm tuning range",* **IEEE Phto.Technol.Lett.**5 pp.608-610 ,1993

35: F.Sugihwo, M.C.Larson and J.S.Harris Jr., "*Micromachined widely tunable vertical cavity laser diodes",* **J. of Microelectromechanical systems**7 pp.48-55 ,1998

36: BA Joyce,N Ohtani,SM Mokler,T Shitara,J Zhang, JH Neave and PN Fawcett, "*Applications of*

RHEED to the study of growth dynamics and surf.chem. of MBE", **Surf. Science**298 pp.399-407 ,1993

37: Foxon CT, "*Molecular-Beam epitaxy - Surface and kinetic effects",* **CRC critical Rev. in Sol.State and Mat. Sciences**10 pp.235-242 ,1981

38: "*thermodynamics of solids*" by:R.A.Swalin published by: John Wiley and Sons 1972

39: "*Molecular Beam Epitaxy: Applications to Key Materials*" by:R.F.C. Farrow published by: Noyes Publications 1995

40: "*Molecular Beam Epitaxy: Fundamentals and current status*" by:MA Herman, H. Sitter published by: Springer- Verlag 1996

41: "*Introduction to solid state physics*" by:C.Kittel published by: John wiley and Sons 2005

42: "*Solid State Physics*" by:N.W.Ashcroft, N.D. Memrin published by: HRW Int.Eds. 1987

43: "*X-Ray diffraction*" by:B.E.Warren published by: Dover 1990

44: , BEDE D1 Installation and operation Manual,

45: P.F.Fewster N.L.Andrew, "*Absolute Lattice Parameter MEasurements",* **J.Appl.Cryst.**28 pp.451-458 ,1995

46: "*Scanning Electron Microscopy*" by:L. Reimer published by: Springer 1998

47: M. Gersley, "*Thermal-field-emission electron optics for nanolithography",* **J. Appl. Phys**65 pp.914 ,1989

48: "*Optical processes in Semiconductors*" by:J.I.Pankove published by: Dover Publications Inc. 1971

49: "*Semiconductor Optoelectronic Devices 2nd Ed*" by:Pallab Bhattacharya published by: Prentice Hall 1997

50: "*Encuclopedia of Analytical Chemsitry*" by:T.H. Gfroerer published by: John Wiley and Sons 2000

51: "*Optoelectronic devices, advanced simulation and analysis*" by:J.Piprek published by: Spinger 2004

52: M.Gurioli A.Vinatieri M.Colocci C.Deparis J.Massies G.Neu A.Bosacchi and S., "*Temperature dpendence of τr and τnr recombination time in GaAs AlGaAs QW",* **Phys.Rev.B**44 pp.3115-3124 ,1991

53: R.Eccleston B.F.Feuerbacher J.Kuhl W.W. Ruhle and K.Ploog, "*Density-dependent radiative lifetimes in GaAs Quantum Wells",* **Phys.Rev.B**45 pp.11403-11406 ,1992

54: J.Feldmann G. Peter E.O. Gobel P.Dawson K. Moore C.Foxon and R.J. Eliot, "*Linewidth Dependence of Radiative Exciton Lifetimes in Quantum Wells",* **Phys.Rev.Letters**59 pp.2337-2340 ,1987

55: M.C.Wang K.Kash C.E.Zah R.Baht and S.L.Chuang, "*Measurement of τnr Auger and τr rates in strained-layer QW systems",* **Appl. Phys. Lett.**62 pp. ,1993

56: A.P.Ongstad D.J. Gallant G.C. Dente, "*Carrier lifetime saturation in InGaAs single Quantum Wells",* **Appl.Phys.Lett**66 pp. ,1995

57: B.Deveaud L.Kappei J.Berney F.Morier-Genoud M.T.Portells-Oberli J.Szczytko, "*Excitonic effects in the luminescence of Quantum wells",* **J.Chem.Phys**318 pp.104-117 ,2005

58: "*Modern GaAs processing methods*" by:Ralph Williams published by: Artech House 1990

59: G.A.Baraff and M.Schluter, "*Binding and formation energies of native defect pairs in GaAs",* **Phys.Rev.B**33 pp.7346-7348 ,1986

60: W.S.Hobson, U.Mohideen, S.J.Pearton, R.E.Slusher and F.Ren, "*SiN/sulphide passivate GaAs/ AlGaAs microdisk lasers",* **IEEE Elect. Lett.**29 pp.2199-2200 ,1993

61: G.Christophe, "*Optimization of plasma-deposited SiIN films for optical channel waveguides",* **Optics and Lasers in Eng.**33 pp.15-20 ,2000

62: K.Jagannadham, "*Compound semiconductor bonded to AlN heat spreader substrate using graded i",* **J.Vac.Sci.Techno.A**25 pp. ,2007

63: W.A. Lanford and M.J. Rand, "*The hydrogen content of plasma-deposited silicon nitride",* **J.Appl.Phys.**49 pp.2473-2477 ,1978

64: M. Hatzakis, B.J.Canavello and J.N.Shaw, "*Single-Step Optical Lift-off Process",* **IBM J. of Research and Development**24 pp.452-460 ,1980

65: E.Aperathitis D.Cengher M.Kayambaki M.Androulidaki G.Deligeorgis ..., "*Evaluation of RIE etching process for integrated GaAs/AlGaAs optoelectronic",* **Mat. Sc. Eng. B**80 pp.77-80 , 2001

66: "*The art of electronics*" by:P.Horowitz and W.Hill published by: Cambirdge Un. Press 1989

67: WWW: www.protel.com

68: J. Bardeen, "*An improved calculation of the energies of metallic Li and Na",* **J.Chem. Phys**6 pp.467-371 ,1938

69: "*The modern theory of Solids*" by:F.Seitz published by: McGrawHill 1940

70: "*Physics of semiconductor and their heterostructures*" by:J. Singh published by: McGraw Hill 1993

71: J.M. Luttinger W.Kohn, "*Motion of electrons and holes in perturbed periodic fields",* **Phys. Rev**97 pp.869-883 ,1955

72: G.E. Pikus and G.L. Bir, "*Effects of deformation on the hole energy spectrum of Germanium and Silicon",* **Sov. Phys.-Solid State**1 pp.1502-1517 ,1960

73: "*Symmetry and Strain-Induced Effects in Semiconductors*" by:G.L.Birr and G.E.Pikus

published by: Wiley 1974

74: C.Y.P.Chao and S.L.Chuang, "*Spin-orbit coupling effects on the valence band structure of strained semic",* **Phys.Rev. B**46 pp.4110-4122 ,1992

75: F.Szmulowicz and G.J.Brown, "*Calculation and photoresponse measurement of the bound-to-continuum IR a in",* **Phys.Rev.B**51 pp.13203 ,1995

76: T.E.Ostromek, "*Evaluation of matrix elements of the 8x8 kp H with k SO contrib, for GaAs",* **Phys.Rev.B**54 pp.14467 ,1996

77: R.H.Henderson and E. Towe, "*Effective mass theory of III-V semiconductors on arbitrary (hkl) surfaces",* **J. Appl. Phys**79 pp. ,1996

78: "*Piezoelectricity*" by:W.G.Cady published by: 1964

79: J.C.Hensel and G.Feher, "*",* **Phys.Rev.B**129 pp.1041 ,1963

80: D.L.Smith, "*Strain-generated electric fields in 111 growth axis strained layer SL's",* **Solid State Communications**57 pp.919 ,1986

81: D.L.smith C.Mailhiot, "*Piezoelectric effects in strained layer superlattices",* **J.Appl.Phys**63 pp.2717 ,1988

82: R.L.Anderson, "*Experiments on Ge-GaAs heterojunctions",* **Solid-state Electronics**5 pp.341 , 1962

83: J.Tersoff, "*Theory of semiconductor heterojunctions: The role of quantum dipoles",* **Phys.Rev.B**30 pp.4874 ,1984

84: N.Debbar D.Biswas and P.Battacharya, "*Conduction-band offsets in pseudomorphic InGaAs/AlGaAs QW",* **Phys.Rev.B**40 pp.1058 ,1989

85: "*Introduction to optical waveguide analysis*" by:K.Kawano and T.Kitoh published by: John Wile & Sons 2001

86: "*Semiconductor Laser Fundamentals, Physics of the gain materials*" by:W.W.Chow and S.W.Koch published by: Springer 1998

87: M.S-C.Luo S.L.Chuang S.Schmitt-Rink and A.Pinczuk, "*Many-Body effects on intersubband spin-density and charge-density excitatio",* **Phys.Rev.B**48 pp.11086-11094 ,1993

88: "*Physics of Optoelectronic devices*" by:S.L.Chuang published by: Wiley InterScience 1995

89: A.E.P. Veldman and K.Rinzema, "*Playing with nonuniform grids",* **J. of Eng.Mathematics**26 pp.119 ,1992

90: "*Numerical respipes in C*" by:W.HPress S.A.Teukolsky W.T.Vetterling and B.P.Flannery published by: Cambridge University Press 2002

91: C.H.Gao, H.Y.Ong, W.J. Fan and S.F.Yoon, "*Analysis of optical gain and Jth of 980nm InGaAs/GaAs QW lasers",* **Computational Material Science**30 pp.296 ,2004

92: W.J.Fan, M.F. Li, T.C. Chong, and J.B.Xia, *Valence hole subbands and optical gain spectra of GaN/AlGaN strained QW's*, 1996

93: M.Nido, M.G.W. Alexander, W.W.Ruhle, T.Schweizer and K.Kohler, "*Nonresonant e and h tunneling times in GaAs/AlGaAs DQW's",* **Appl.Phys.Lett**56 pp.355-357 ,1990

94: E.T.Yu, M.K.Jackson and T.C. McGill, "*Hole tunneling in GaAs/AlGaAs double-barrier structures",* **Appl.Phys.Lett.**55 pp.744-746 ,1989

95: J.Bardeen, "*Tunneling from a many-particle point of view",* **Phys.Rev.Lett.**6 pp.57-59 ,1961

96: F.Yang, P.Blood and J.S.Roberts, "*",* **Appl.Phys.Lett**66 pp.2949 ,1995

97: J. Piprek, P.Abraham and J.E. Bowers, "*",* **IEEE J. of Sel. Topics in Quant. El.**5 pp.643 ,1999

98: T.SMoisE, L.J.Guido, R.C.Barker, J.O.White and R.Kost, "*Screening effects in (111)B AlGaAs/ InGaAs SQW heterostructures",* **Appl.Phys.Lett**60 pp.2637-2639 ,1992

99: L.C.Anreani, "*",* **Solid state Comm.**77 pp.641 ,1991

100: G.Deligeorgis, G.E. dialynas, Z. Hatzopoulos and N.T.Pelekanos, Threshold current reduction due to piezoelectric effects in InGaAs LD's, 2005

101: G.Deligeorgis, M.Guriolli, A. vinatieri, Z.Hatzopoulos and N.T. Pelekanos, Carrier dynamics of LD structures grown on (100) and (111)B orientation, 2008

102: G.Deligeorgis, G.dialynas, Z.Hatzopoulos and N.T.Pelekanos, Polarization field effects on optical gain and lasing characteristics, 2005

103: G.Deligeorgis, G.E.Dialynas, N. Le Thomas, Z.Hatzopoulos and N.T.Pelekanos, Piezoelectric effect on the lasing characteristics of (111)B InGaAs LD, 2005

104: G. Dialynas, G.Deligeorgis, M.Zervos and N.T. Pelekanos, "*Influence of polarization field on the lasing properties of III-Nitride QW",* **Physica E: Low dimensional Systems and Nanostructu**32 pp.558-561 ,2006

105: T.Tada, A.Yamaguchi, T.Ninomiya, H.Uchiki, T.Kobayashi and T.Yao, "*Tunneling proces in AlAs/GaAs DQW studied by PL",* **J.Appl.Phys.**63 pp.5491-5494 ,1988

106: R.Clerc, A.Spineli, G.Ghibaudo and G.Pananakis, "*theory of tunneling in MOS structures",* **J. of Appl.Phys.**91 pp.1400-1409 ,2002

107: WWW: www.atmel.com